

RESEARCH ARTICLE

Phase-field-crystal models for condensed matter dynamics on atomic length and diffusive time scales: an overview

Heike Emmerich<sup>a\*</sup>, Hartmut Löwen<sup>b\*</sup>, Raphael Wittkowski<sup>b</sup>, Thomas Gruhn<sup>a</sup>, Gyula I. Tóth<sup>c</sup>, György Tegze<sup>c</sup>, and László Gránásy<sup>c,d\*</sup>

<sup>a</sup>*Lehrstuhl für Material- und Prozesssimulation, Universität Bayreuth, D-95440 Bayreuth, Germany,*

<sup>b</sup>*Institut für Theoretische Physik II, Weiche Materie, Heinrich-Heine-Universität Düsseldorf, D-40225 Düsseldorf, Germany,*

<sup>c</sup>*Institute for Solid State Physics and Optics, Wigner Research Centre for Physics, P.O. Box 49, H-1525 Budapest, Hungary,*

<sup>d</sup>*BCAST, Brunel University, Uxbridge, Middlesex, UB8 3PH, U.K.*

*(Received 00 Month 200x; final version received 00 Month 200x)*

Here, we review the basic concepts and applications of the *phase-field-crystal* (PFC) method, which is one of the latest simulation methodologies in materials science for problems, where atomic- and microscales are tightly coupled. The PFC method operates on atomic length and diffusive time scales, and thus constitutes a computationally efficient alternative to molecular simulation methods. Its intense development in materials science started fairly recently following the work by Elder et al. [Phys. Rev. Lett. 88 (2002), p. 245701]. Since these initial studies, dynamical density functional theory and thermodynamic concepts have been linked to the PFC approach to serve as further theoretical fundamentals for the latter. In this review, we summarize these methodological development steps as well as the most important applications of the PFC method with a special focus on the interaction of development steps taken in hard and soft matter physics, respectively. Doing so, we hope to present today’s state of the art in PFC modelling as well as the potential, which might still arise from this method in physics and materials science in the nearby future.

**Keywords:** phase-field-crystal (PFC) models, static and dynamical density functional theory (DFT and DDFt), condensed matter dynamics of liquid crystals and polymers, nucleation and pattern formation, simulations in materials science, colloidal crystal growth and growth anisotropy

\*Corresponding authors. Emails: heike.emmerich@uni-bayreuth.de, hlowen@thphy.uni-duesseldorf.de, and grana@szfki.hu

arXiv:1207.0257v1 [cond-mat.soft] 2 Jul 2012

### Table of contents

1. Introduction	4. Phase-field-crystal models applied to nucleation and pattern formation in metals
2. From density functional theory to phase-field-crystal models	4.1. Properties of nuclei from extremum principles
2.1. Density functional theory	4.1.1. Homogeneous nucleation
2.2. Dynamical density functional theory	4.1.2. Heterogeneous nucleation
2.2.1. Basic equations	4.2. Pattern formation
2.2.2. Brownian dynamics: Langevin and Smoluchowski picture	4.2.1. PFC modelling of surface patterns
2.2.3. Derivation of DDFT	4.2.2. Pattern formation in binary solidification
2.2.4. Application of DDFT to colloidal crystal growth	4.3. Phenomena in the solid state
2.3. Derivation of the PFC model for isotropic particles from DFT	4.3.1. Dislocation dynamics and grain boundary melting
2.3.1. Free-energy functional	4.3.2. Crack formation and propagation
2.3.2. Dynamical equations	4.3.3. Strain-induced morphologies
2.3.3. Colloidal crystal growth: DDFT versus PFC modelling	4.3.4. Kirkendall effect
3. Phase-field-crystal modelling in condensed matter physics	4.3.5. Density/solute trapping
3.1. The original PFC model and its generalisations	4.3.6. Vacancy/atom transport in the VPFC model
3.1.1. Single-component PFC models	5. Phase-field-crystal modelling in soft matter physics
3.1.2. Binary PFC models	5.1. Application to colloids
3.1.3. PFC models for liquid crystals	5.1.1. Nucleation in colloidal crystal aggregation
3.1.4. Numerical methods	5.1.2. Pattern formation in colloidal crystal aggregation
3.1.5. Coarse-graining the PFC models	5.1.3. Colloid patterning
3.2. Phase diagrams the PFC models realize	5.2. Application to polymers
3.2.1. Phase diagram of single-component and binary systems	5.2.1. Self-consistent field theory for polymer systems
3.2.2. Phase diagram of two-dimensional liquid crystals	5.2.2. Phase-field methods for polymer systems
3.3. Anisotropies in the PFC models	5.2.3. Comparison of the methods
3.3.1. Free energy of the liquid-solid interface	5.3. Application to liquid crystals
3.3.2. Growth anisotropy	6. Summary and outlook
3.4. Glass formation	Appendix
3.5. Phase-field-crystal modelling of foams	Acknowledgements
3.6. Coupling to hydrodynamics	References
	List of abbreviations

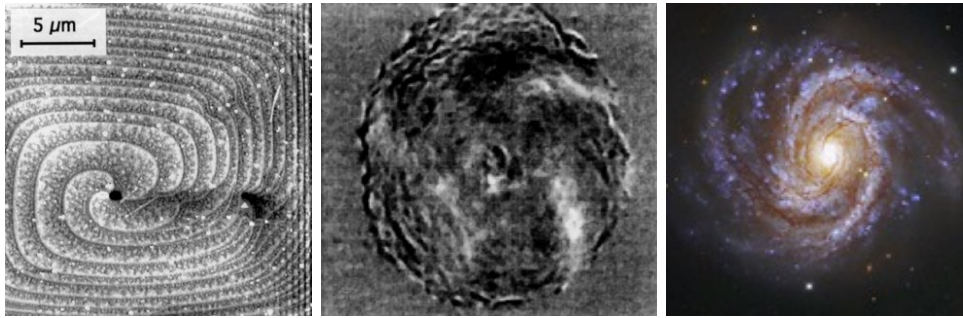


Figure 1. Pattern formation on microscopic to cosmic length scales. From left to right: multiple spiralling nanoscale terraces starting from a central heterogeneity. (Reproduced with permission from C. Klemenz, *Hollow cores and step-bunching effects on (001) YBCO surfaces grown by liquid-phase epitaxy*, *J. Cryst. Growth* 187 (1998), 221-227, no. 2, DOI: 10.1016/S0022-0248(97)00866-X © 1998 by Elsevier.) Cellular slime mould self-organized into a five-arm spiral structure. (Reproduced with permission from B. Vasiev, F. Siegert, and C. Weijer, *Multiarmed spirals in excitable media*, *Phys. Rev. Lett.* 78 (1997), 2489-2492, no. 12, DOI: 10.1103/PhysRevLett.78.2489 © 1997 by the American Physical Society.) Messier 100, a multi-arm spiral galaxy in the Virgo Supercluster, 60 million light-years from earth. (Credit: ESO/IDA/Danish 1.5m/R. Gendler, J.-E. Ovaldsen, C. C. Thöne, and C. Féron.)

## 1. Introduction

Pattern formation has been observed in complex systems from microscopic to cosmic scales (for examples, see figure 1), a phenomenon that has been exciting the fantasy of humanity for a long time. Nonequilibrium systems in physics, chemistry, biology, mathematics, cosmology, and other fields produce an amazingly rich and visually fascinating variety of spatiotemporal behaviour. Experiments and simulations show that many of such systems – reacting chemicals, bacteria colonies, granular matter, plasmas – often display analogous dynamical behaviour. The wish to find the origin of the common behaviour has been driving the efforts for finding unifying schemes that allow the assigning of many of these processes into a few universality classes. Pattern formation and the associated nonlinear dynamics have received a continuous attention of the statistical physics community over the past decades. Reviews of the advances made in different directions are available in the literature and range from early works on critical dynamics [1] via phase-separation [2] and pattern formation in nonequilibrium systems [3, 4] to recent detailed treatments of the field in books (e. g., references [5–7]).

In particular, Seul and Andelman [4] described pattern formation on the mesoscale as manifestation of modulated structures. Within this approach, the modulated phases are stabilized by competing attractive and repulsive interactions, which favour inhomogeneities characterized by a certain modulation length scale. The modulations are described by a single scalar order parameter. As outlined in reference [4], the idea of Seul and Andelman can be applied to a large variety of systems ranging from Langmuir films over semiconductor surfaces and magnet garnets to polyelectrolyte solutions. Furthermore, the pioneering theories of spontaneous domain formation in magnetic materials and in the intermediate state of type I superconductors has been reinterpreted within this framework.

In the past decade, special attention has been paid to a similar model, whose mathematical formulation has been laid down decades earlier to address hydrodynamic instabilities [10] and to describe the transition to the antiferromagnetic state in liquid  $^3\text{He}$  or to a non-uniform state in cholesteric liquid crystals [11], whereas recently it has been employed for the modelling of crystallization in undercooled liquids on the atomic scale [12]. This approach is known to the materials science community as the phase-field-crystal (PFC) model [12], and has proven to be an amazingly efficient tool for addressing crystalline self-organization/pattern formation on the *atomistic* scale.

The PFC approach attracts attention owing to a unique situation: the crystallization of liquids is traditionally addressed on this scale by the density functional theory (DFT) [13–15], whose best developed non-perturbative version, known as the fundamental-measure theory (FMT) [16], leads to unprecedented accuracy for such properties as the liquid-solid interfacial free energy [17, 18] or the nucleation barrier [17]. However, handling of large systems is hampered by the complexity of such models. In turn, the PFC model, being a simplistic DFT itself, incorporates most of the essential physics required to handle freezing: it is atomistic, anisotropies and elasticity are automatically there, the system may choose from a variety of periodic states [such as body-centred cubic (bcc), face-centred cubic (fcc), and hexagonal close packed (hcp)] besides the homogeneous fluid, etc. The free-energy functional is fairly simple having the well-known Swift-Hohenberg (SH) form

$$\tilde{\mathcal{F}} = \int d\tilde{\mathbf{r}} \left( \frac{\tilde{\psi}}{2} \left( -\beta + (k_0^2 + \nabla_{\tilde{\mathbf{r}}}^2)^2 \right) \tilde{\psi} + \frac{\tilde{\psi}^4}{4} \right), \quad (1)$$

where  $\tilde{\psi}$  is the reduced particle density and  $\beta$  a reduced temperature, while  $k_0$  is the absolute value of the wave number vector the system prefers. (In equation (1) all quantities are dimensionless.) This together with the assumption of overdamped conservative (diffusive) dynamics (a major deviation from the non-conservative dynamics of the SH model) leads to a relatively simple equation of motion (EOM) that, in turn, allows the handling of a few times  $10^7$  atoms on the diffusive time scale. Such abilities can be further amplified by the amplitude equation versions [19] obtained by renormalisation group theory, which combined with advanced numerics [20] allows for the handling of relatively big chunks of material, while retaining all the atomic scale physics. Such a coarse-grained PFC model, relying on equations of motion for the amplitudes and phases, can be viewed as a physically motivated continuum model akin to the highly successful and popular phase-field (PF) models [21–25], which however usually contain *ad hoc* assumptions. Accordingly, the combination of the PFC model with coarse graining establishes a link between DFT and conventional PF models, offering a way for deriving the latter on physical grounds.

In its simplest formulation, defined above, the PFC model consists of only a single model parameter  $\beta$  (provided that length is measured in  $k_0^{-1}$  units). Still it has a fairly complex phase diagram in three spatial dimensions (3D), which has stability domains for the bcc, fcc, and hcp structures, as opposed to the single triangular crystal structure appearing in 2D. Introducing additional model parameters, recent extensions of the PFC model either aim at further controlling of the predicted crystal structure or attempt to refine the description of real materials. Other extensions address binary systems, yet others modify the dynamics via considering further modes of density relaxation besides the diffusive one, while adopting a free energy that ensures particle conservation and allows assigning inertia to the particles. In a few cases, PFC models tailored to specific applications have reached the level of being quantitative. Via the PFC models, a broad range of exciting phenomena became accessible for atomistic simulations (see Tab. 1), a situation that motivates our review of the present status of PFC modelling.

While Tab. 1 contains a fairly impressive list, it is expected to be only the beginning of the model's employment in materials science and engineering. For example, true knowledge-based tailoring of materials via predictive PFC calculations is yet an open vision, for which a number of difficulties need to be overcome. We are going to review a few of the most fundamental ones of these open issues. For example,

the PFC models still have to establish themselves as widely accepted simulation tools in materials engineering/design, which requires methodological advances in various directions such as (a) ensuring the quantitateness of PFC predictions for practically relevant (multi-phase multi-component) materials and (b) a consistent extension of PFC modelling to some essential circumstances such as non-isothermal problems, coupling to hydrodynamics, or handling of non-spherical molecules.

So far, only limited reviews of PFC modelling are available [25, 62]. Therefore, we give a comprehensive overview of PFC modelling in the present review. Especially, we present the main achievements of PFC modelling and demonstrate the potential these models offer for addressing problems in physics and materials science. We pay special attention to the similarities and differences of development steps taken in hard and soft matter physics, respectively. The rest of our review article is structured as follows: in section 2, we present a detailed theoretical derivation of the PFC model on the basis of dynamical density functional theory (DDFT). Section 3 is devoted to some essential features of the PFC model and its generalisations including the realization of different crystal lattices, the predicted phase diagrams, anisotropy, and some specific issues such as glass formation, application to foams, and the possibility for coupling to hydrodynamics. Section 4 addresses nucleation and pattern formation in metallic alloys, whereas section 5 deals with the application of the PFC models to prominent soft matter systems. Finally, in section 6, we offer a few concluding remarks and an outlook to probable developments in the near future.

## 2. From density functional theory to phase-field-crystal models

Freezing and crystallization phenomena are described best on the most fundamental level of individual particles, which involves the microscopic size and interaction

Table 1. A non-exclusive collection of phenomena addressed using PFC techniques.

Phenomena	References
Liquid-solid transition:	
– dendrites	[26–30]
– eutectics	[26, 28, 29, 31]
– homogeneous nucleation	[28, 30–33]
– heterogeneous nucleation	[30, 31, 34, 35]
– grain-boundary melting	[36, 37]
– fractal growth	[38, 39]
– crystal anisotropy	[33, 38, 40–44]
– density/solute trapping	[38, 39, 45]
– glass formation	[35, 46, 47]
– surface alloying	[48, 49]
Colloid patterning	[33]
Grain-boundary dynamics	[50]
Crack propagation	[50]
Elasticity, plasticity, dislocation dynamics	[12, 50–54]
Kirkendall effect	[55]
Vacancy transport	[56]
Liquid phase separation with colloid accumulation at phase boundaries	[57]
Liquid crystals	[58–60]
Formation of foams	[61]

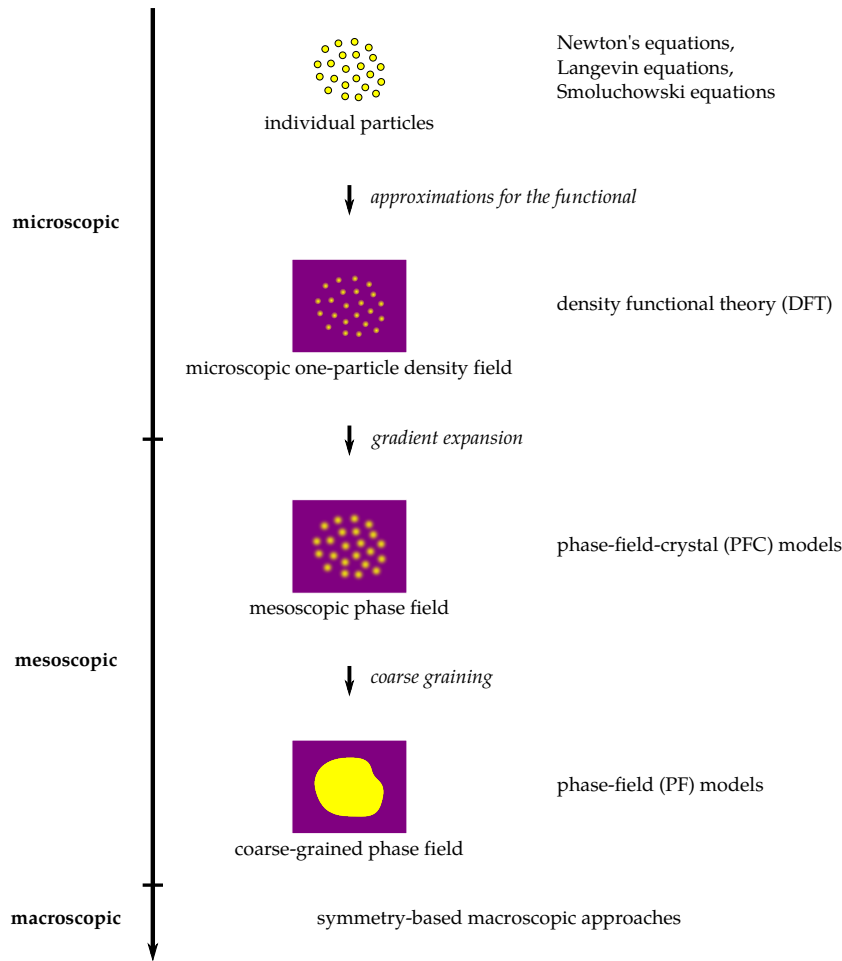


Figure 2. Levels of description with the corresponding methods and theories (schematic).

length scale of the particles (see figure 2). The individual dynamics of the particles happens correspondingly on a microscopic time scale. In the following, two different classes of materials, namely *molecular* and *colloidal* materials, need clear distinction. The former comprise metals as well as molecular insulators and semiconductors. We consider these molecular systems as classical particles, where the quantum-mechanical nature of the electrons merely enters via effective molecular force fields. The corresponding molecular dynamics is governed by Newton's second law. Hence the length scale is atomic (about a few Angstroms) and the typical time scale is roughly a picosecond.

The latter material class of colloidal systems involves typically mesoscopic particles immersed in a molecular viscous fluid as a solvent that are interacting via effective forces [63]. These colloidal suspensions have a dimension typically in the range between a nanometre and a micrometre and are therefore classical particles. Thus, the corresponding “microscopic” length scale describing their extension and interaction range is much bigger than for the molecular materials. The individual particle dynamics is *Brownian motion* [64, 65], i. e., it is completely overdamped<sup>1</sup> superimposed with stochastic kicks of the solvent. The corresponding coarse-grained Brownian time scale upon which individual particle motion occurs is much longer (about a microsecond) [68].

<sup>1</sup>It is interesting to note that there are also mesoscopic particle systems with Newtonian dynamics, which are virtually undamped. These are realized in so-called complex plasmas [66, 67], where dust particles are dispersed and levitated in a plasma.

In terms of static equilibrium properties (such as structural correlations and phase transitions), both metals and colloids can just be regarded as classical interacting many-body systems. For this purpose, density functional theory (DFT) was developed [14, 15, 69]: DFT is a microscopic theory, i. e., it starts with the (effective) interparticle interactions and predicts the free energy and the static many-body correlations. In principle, DFT is exact, but for practical applications one has to rely on approximations.

In the past years, it has become clear that DFT is an ideal theoretical framework to justify and to derive the free-energy functional of coarse-grained models as the PFC approach [26, 70]. PFC models keep the microscopic length scale, but describe the microscopically structured density field in a very rough way, for example, by keeping only its first Fourier modes for a crystal. Although some microscopic details are lost, the basic picture of the crystal is kept and much larger system sizes can be explored numerically. The PFC models are superior to simple PF models, which work with a single order parameter on a more coarse-grained regime. Finally, there are also phenomenological hydrodynamic approaches that are operating on the macroscopic length and time scale.

This pretty transparent hierarchy of length scales for static equilibrium properties gets more complex for the dynamics. In order to discuss this in more detail, it is advantageous to start with the colloidal systems first. Here, the individual dynamics is already dissipative and overdamped: the “microscopic” equations governing the colloidal Brownian dynamics are either the *Langevin equation* for the individual particle trajectories or the *Smoluchowski equation* for the time evolution of the many-body probability density [71, 72]. Both approaches are stochastically equivalent [73]. In the end of the past century, it has been shown that there is a dynamic generalisation of DFT, the DDFT, which describes the time evolution of the many-body system within the time-dependent one-body density as a generalized deterministic diffusion equation. This provides a significant simplification of the many-body problem. Unfortunately, DDFT is not on the same level as the Smoluchowski or Langevin picture since an additional adiabaticity approximation is needed to derive it. This approximation implies, that the one-body density is a slowly relaxing variable and all higher density correlations relax much faster to thermodynamic equilibrium [74]. Fortunately, the adiabaticity approximation is reasonable for many practical applications except for situations, where fluctuations play a significant role. Now, DDFT can be used as an (approximate) starting point to derive the dynamics of a PFC model systematically [70]. This also points to alternative dynamical equations, which can be implemented within a numerically similar effort as compared to ordinary PFC equations, but are a bit closer to DDFT.

For Newtonian dynamics, on the other hand, intense research is going on to derive a similar kind of DDFT [75–78]. Still the diffusive (or model B) dynamics for a conserved order-parameter field can be used as an effective dynamics on mesoscopic time scales with an effective friction. Then, the long-time self-diffusion coefficient sets the time scale of this process. One should, however, point out that the PFC dynamics for molecular systems is dynamically more coarse-grained than for their colloidal counterparts.

## 2.1. Density functional theory

Density functional theory (DFT) is a microscopic theory for inhomogeneous complex fluids in equilibrium [14, 15, 69, 79] that needs only the particle interactions and the underlying thermodynamic conditions as an input. The central idea is to

express the free energy of the many-body system as a functional of the inhomogeneous one-body density. As it stands originally, DFT is a theory for static quantities. Most of the actual applications of DFT are for spherically symmetric pairwise interactions between classical particles (mostly hard spheres) [14, 69, 80], but they can also be generalized to anisotropic interactions (as relevant for non-spherical hard bodies or molecules) [81–84]. One of the key applications of DFT concerns the equilibrium freezing and melting [14, 15, 85, 86] including the fluid-solid interface [87–90]. Further information about DFT and a detailed historic overview can be found in several articles and books like references [87, 91–94].

More recently, static DFT was generalized towards time-dependent processes in nonequilibrium. The extended approach is called dynamical density functional theory (DDFT). DDFT was first derived in 1999 for isotropic Brownian particles by Marconi and Tarazona [95, 96] starting from the Langevin picture of individual particle trajectories. An alternate derivation based on the Smoluchowski picture was presented in 2004 by Archer and Evans [97]. In both schemes an additional *adiabaticity approximation* is needed: correlations of high order in nonequilibrium are approximated by those in equilibrium for the same one-body density. These derivations were complemented by a further approach on the basis of a projection operator technique [74]. The latter approach sheds some light on the adiabaticity approximation: it can be viewed by the assumption that the one-body density relaxes much slower than any other density correlations of higher order. DDFT can be flexibly generalized towards more complex situations including mixtures [98], active particles [99], hydrodynamic interactions [100, 101], shear flow [102] and non-spherical particles [103, 104]. However, as already stated above, it is much more difficult to derive a DDFT for Newtonian dynamics, where inertia and flow effects invoke a treatment of the momentum density field of the particles [75–78].

In detail, DFT gives access to the free energy for a system of  $N$  classical particles, whose centre-of-mass positions are defined through the vectors  $\mathbf{r}_i$  with  $i \in \{1, \dots, N\}$ , by the *one-particle density*  $\rho(\mathbf{r})$ , which provides the probability to find a particle at position  $\mathbf{r}$ . Its microscopic definition is

$$\rho(\mathbf{r}) = \left\langle \sum_{i=1}^N \delta(\mathbf{r} - \mathbf{r}_i) \right\rangle \quad (2)$$

with the normalised classical canonical (or grand canonical) ensemble-average  $\langle \cdot \rangle$ . At given temperature  $T$  and chemical potential  $\mu$ , the particles are interacting via a pairwise (two-body) potential  $U_2(\mathbf{r}_1 - \mathbf{r}_2)$ . Furthermore, the system is exposed to an external (one-body) potential  $U_1(\mathbf{r})$  (describing, for example, gravity or system boundaries), which gives rise in general to an inhomogeneous one-particle density  $\rho(\mathbf{r})$ . DFT is based on the following variational theorem:

*There exists a unique grand canonical free-energy functional  $\Omega(T, \mu, [\rho(\mathbf{r})])$  of the one-particle density  $\rho(\mathbf{r})$ , which becomes minimal for the equilibrium one-particle density  $\rho(\mathbf{r})$ :*

$$\frac{\delta\Omega(T, \mu, [\rho(\mathbf{r})])}{\delta\rho(\mathbf{r})} = 0. \quad (3)$$

*If the grand canonical functional  $\Omega(T, \mu, [\rho(\mathbf{r})])$  is evaluated at the equilibrium one-particle density  $\rho(\mathbf{r})$ , it is the real equilibrium grand canonical free energy of the inhomogeneous system.*

Hence, DFT establishes a basis for the determination of the equilibrium one-particle density field  $\rho(\mathbf{r})$  of an arbitrary classical many-body system. However, in practice,



the exact form of the grand canonical free-energy density functional  $\Omega(T, \mu, [\rho(\mathbf{r})])$  is not known and one has to rely on approximations. Via a Legendre transform, the grand canonical functional can be expressed by an equivalent Helmholtz free-energy functional  $\mathcal{F}(T, [\rho(\mathbf{r})])$ ,

$$\Omega(T, \mu, [\rho(\mathbf{r})]) = \mathcal{F}(T, [\rho(\mathbf{r})]) - \mu \int d\mathbf{r} \rho(\mathbf{r}), \quad (4)$$

with  $V$  denoting the system volume. The latter is conveniently split into three contributions:

$$\mathcal{F}(T, [\rho(\mathbf{r})]) = \mathcal{F}_{\text{id}}(T, [\rho(\mathbf{r})]) + \mathcal{F}_{\text{exc}}(T, [\rho(\mathbf{r})]) + \mathcal{F}_{\text{ext}}(T, [\rho(\mathbf{r})]). \quad (5)$$

Here,  $\mathcal{F}_{\text{id}}(T, [\rho(\mathbf{r})])$  is the (exact) *ideal gas free-energy functional* [69]

$$\mathcal{F}_{\text{id}}(T, [\rho(\mathbf{r})]) = k_{\text{B}}T \int d\mathbf{r} \rho(\mathbf{r}) (\ln(\Lambda^3 \rho(\mathbf{r})) - 1), \quad (6)$$

where  $k_{\text{B}}$  is the Boltzmann constant and  $\Lambda$  the thermal de Broglie wavelength. The second term on the right-hand-side of equation (5) is the *excess free-energy functional*  $\mathcal{F}_{\text{exc}}(T, [\rho(\mathbf{r})])$  describing the excess free energy over the exactly known ideal-gas functional. It incorporates all correlations due to the pair interactions between the particles. In general, it is not known explicitly and therefore needs to be approximated appropriately [14, 69]. The last contribution is the *external free-energy functional* [69]

$$\mathcal{F}_{\text{ext}}(T, [\rho(\mathbf{r})]) = \int d\mathbf{r} \rho(\mathbf{r}) U_1(\mathbf{r}). \quad (7)$$

A formally exact expression for  $\mathcal{F}_{\text{exc}}(T, [\rho(\mathbf{r})])$  is gained by a functional Taylor expansion in the density variations  $\Delta\rho(\mathbf{r}) = \rho(\mathbf{r}) - \rho_{\text{ref}}$  around a homogeneous reference density  $\rho_{\text{ref}}$  [69, 85]:

$$\mathcal{F}_{\text{exc}}(T, [\rho(\mathbf{r})]) = \mathcal{F}_{\text{exc}}^{(0)}(\rho_{\text{ref}}) + k_{\text{B}}T \sum_{n=1}^{\infty} \frac{1}{n!} \mathcal{F}_{\text{exc}}^{(n)}(T, [\rho(\mathbf{r})]) \quad (8)$$

with

$$\mathcal{F}_{\text{exc}}^{(n)}(T, [\rho(\mathbf{r})]) = - \int d\mathbf{r}_1 \cdots \int d\mathbf{r}_n c^{(n)}(\mathbf{r}_1, \dots, \mathbf{r}_n) \prod_{i=1}^n \Delta\rho(\mathbf{r}_i). \quad (9)$$

Here,  $c^{(n)}(\mathbf{r}_1, \dots, \mathbf{r}_n)$  denotes the  $n$ th-order direct correlation function [92] in the homogeneous reference state given by

$$c^{(n)}(\mathbf{r}_1, \dots, \mathbf{r}_n) = - \frac{1}{k_{\text{B}}T} \left. \frac{\delta^n \mathcal{F}_{\text{exc}}(T, [\rho(\mathbf{r})])}{\delta\rho(\mathbf{r}_1) \cdots \delta\rho(\mathbf{r}_n)} \right|_{\rho_{\text{ref}}} \quad (10)$$

depending parametrically on  $T$  and  $\rho_{\text{ref}}$ .

In the functional Taylor expansion (8), the constant zeroth-order contribution

is irrelevant and the first-order contribution corresponding to  $n = 1$  is zero.<sup>1</sup> The higher-order terms are nonlocal and do not vanish in general.

In the simplest nontrivial approach, the functional Taylor expansion is truncated at second order. The resulting approximation is known as the *Ramakrishnan-Yussouff theory* [85]

$$\mathcal{F}_{\text{exc}}(T, [\rho(\mathbf{r})]) = -\frac{1}{2}k_{\text{B}}T \int d\mathbf{r}_1 \int d\mathbf{r}_2 c^{(2)}(\mathbf{r}_1 - \mathbf{r}_2) \Delta\rho(\mathbf{r}_1) \Delta\rho(\mathbf{r}_2) \quad (11)$$

and predicts the freezing transition of hard spheres both in three [85] and two spatial dimensions (2D) [105].<sup>1</sup> The Ramakrishnan-Yussouff approximation needs the fluid direct pair-correlation function  $c^{(2)}(\mathbf{r}_1 - \mathbf{r}_2)$  as an input. For example,  $c^{(2)}(\mathbf{r}_1 - \mathbf{r}_2)$  can be gained from liquid integral equation theory, which links  $c^{(2)}(\mathbf{r}_1 - \mathbf{r}_2)$  to the pair-interaction potential  $U_2(\mathbf{r}_1 - \mathbf{r}_2)$ . Well-known analytic approximations for the direct pair-correlation function include the second-order *virial expression* [109]

$$c^{(2)}(\mathbf{r}_1 - \mathbf{r}_2) = \exp\left(-\frac{U_2(\mathbf{r}_1 - \mathbf{r}_2)}{k_{\text{B}}T}\right) - 1. \quad (12)$$

The resulting *Onsager functional* for the excess free energy becomes asymptotically exact in the low density limit [92]. An alternative is the *random-phase* or *mean-field approximation*

$$c^{(2)}(\mathbf{r}_1 - \mathbf{r}_2) = -\frac{U_2(\mathbf{r}_1 - \mathbf{r}_2)}{k_{\text{B}}T}. \quad (13)$$

For bounded potentials, this mean-field approximation becomes asymptotically exact at high densities [103, 110–112]. Non-perturbative expressions for the excess free-energy functional for colloidal particles are given by *weighted-density approximations* [81, 84, 87, 113, 114] or follow from FMT [82, 115]. FMT was originally introduced in 1989 by Rosenfeld for isotropic particles [16, 86, 91, 116] and then refined later [80, 117] – for a review, see reference [79]. For hard spheres, FMT provides an excellent approximation for the excess free-energy functional with an unprecedented accuracy. It was also generalized to arbitrarily shaped particles [82, 115, 118].

## 2.2. Dynamical density functional theory

### 2.2.1. Basic equations

Dynamical density functional theory (DDFT) is the time-dependent analogue of static DFT and can be classified as *linear-response theory*. In its basic form, it describes the slow dissipative nonequilibrium relaxation dynamics of a system of  $N$  Brownian particles close to thermodynamic equilibrium or the behaviour in a time-dependent external potential  $U_1(\mathbf{r}, t)$ . Now a time-dependent one-particle

<sup>1</sup>This follows from the representation (9) under consideration of the translational and rotational symmetries of the isotropic bulk fluid that also apply to the direct correlation function  $c^{(1)}(\mathbf{r}_1) = \text{const.}$

<sup>1</sup>More refined approaches include also the third-order term [106] with an approximate triplet direct correlation function [107, 108].

density field is defined via

$$\rho(\mathbf{r}, t) = \left\langle \sum_{i=1}^N \delta(\mathbf{r} - \mathbf{r}_i(t)) \right\rangle, \quad (14)$$

where  $\langle \cdot \rangle$  denotes the normalised classical canonical noise-average over the particle trajectories and  $t$  is the time variable.

This one-particle density is conserved and its dynamics is assumed to be dissipative via the generalized (deterministic) diffusion equation

$$\frac{\partial \rho(\mathbf{r}, t)}{\partial t} = \frac{D_T}{k_B T} \nabla_{\mathbf{r}} \cdot \left( \rho(\mathbf{r}, t) \nabla_{\mathbf{r}} \frac{\delta \mathcal{F}(T, [\rho(\mathbf{r}, t)])}{\delta \rho(\mathbf{r}, t)} \right). \quad (15)$$

Here,  $D_T$  denotes a (short-time) translational diffusion coefficient for the Brownian system. Referring to equations (3) and (4), the functional derivative in the DDFT equation can be interpreted as an inhomogeneous chemical potential

$$\mu(\mathbf{r}, t) = \frac{\delta \mathcal{F}(T, [\rho(\mathbf{r}, t)])}{\delta \rho(\mathbf{r}, t)} \quad (16)$$

such that the DDFT equation (15) corresponds to a generalized Fick's law of particle diffusion. As already mentioned, DDFT was originally invented [95, 97] for colloidal particles, which exhibit Brownian motion, but is less justified for metals and atomic systems whose dynamics are ballistic [75, 76].

### 2.2.2. Brownian dynamics: Langevin and Smoluchowski picture

The DDFT equation (15) can be derived [95] from Langevin equations that describe the stochastic motion of the  $N$  isotropic colloidal particles in an incompressible liquid of viscosity  $\eta$  at low Reynolds number (Stokes limit). In the absence of hydrodynamic interactions between the Brownian particles, these coupled Langevin equations for the positions  $\mathbf{r}_i(t)$  of the colloidal spheres with radius  $R_s$  describe completely overdamped motion plus stochastic noise [71, 73]:

$$\dot{\mathbf{r}}_i = \xi^{-1}(\mathbf{F}_i + \mathbf{f}_i), \quad i = 1, \dots, N. \quad (17)$$

Here,  $\xi$  is the Stokesian friction coefficient ( $\xi = 6\pi\eta R_s$  for spheres of radius  $R_s$  with stick boundary conditions) and

$$\mathbf{F}_i(t) = -\nabla_{\mathbf{r}_i} U(\mathbf{r}_1, \dots, \mathbf{r}_N, t) \quad (18)$$

are the deterministic forces caused by the total potential

$$U(\mathbf{r}_1, \dots, \mathbf{r}_N, t) = U_{\text{ext}}(\mathbf{r}_1, \dots, \mathbf{r}_N, t) + U_{\text{int}}(\mathbf{r}_1, \dots, \mathbf{r}_N) \quad (19)$$

with

$$U_{\text{ext}}(\mathbf{r}_1, \dots, \mathbf{r}_N, t) = \sum_{i=1}^N U_1(\mathbf{r}_i, t) \quad (20)$$

and

$$U_{\text{int}}(\mathbf{r}_1, \dots, \mathbf{r}_N) = \sum_{\substack{i,j=1 \\ i < j}}^N U_2(\mathbf{r}_i - \mathbf{r}_j). \quad (21)$$

On top of these deterministic forces, also stochastic forces  $\mathbf{f}_i(t)$  due to thermal fluctuations act on the Brownian particles. These random forces are modelled by Gaussian white noises with vanishing mean values

$$\langle \mathbf{f}_i(t) \rangle = \mathbf{0} \quad (22)$$

and with Markovian second moments

$$\langle \mathbf{f}_i(t_1) \otimes \mathbf{f}_j(t_2) \rangle = 2\xi k_B T \mathbf{1} \delta_{ij} \delta(t_1 - t_2), \quad (23)$$

where  $\otimes$  is the ordinary (dyadic) tensor product (to make the notation compact) and  $\mathbf{1}$  denotes the  $3 \times 3$ -dimensional unit matrix. This modelling of the stochastic forces is dictated by the fluctuation-dissipation theorem, which for spheres yields the Stokes-Einstein relation  $D_T = k_B T / \xi$  [64], that couples the short-time diffusion coefficient  $D_T$  of the colloidal particles to the Stokes friction coefficient  $\xi$ .

An alternate description of Brownian dynamics is provided by the Smoluchowski picture, which is stochastically equivalent to the Langevin picture [72, 73]. The central quantity in the Smoluchowski picture is the  $N$ -particle probability density  $P(\mathbf{r}_1, \dots, \mathbf{r}_N, t)$  whose time evolution is described by the Smoluchowski equation [73, 119]

$$\frac{\partial}{\partial t} P(\mathbf{r}_1, \dots, \mathbf{r}_N, t) = \hat{\mathcal{L}} P(\mathbf{r}_1, \dots, \mathbf{r}_N, t) \quad (24)$$

with the Smoluchowski operator

$$\hat{\mathcal{L}} = D_T \sum_{i=1}^N \nabla_{\mathbf{r}_i} \cdot \left( \nabla_{\mathbf{r}_i} \frac{U(\mathbf{r}_1, \dots, \mathbf{r}_N, t)}{k_B T} + \nabla_{\mathbf{r}_i} \right). \quad (25)$$

While the  $N$ -particle probability density  $P(\mathbf{r}_1, \dots, \mathbf{r}_N, t)$  in this Smoluchowski equation is a highly nontrivial function for interacting particles, it is often sufficient to consider one-body or two-body densities. The one-particle probability density  $P(\mathbf{r}, t)$  is proportional to the one-particle number density  $\rho(\mathbf{r}, t)$ . In general, all  $n$ -particle densities with  $n \leq N$  can be obtained from the  $N$ -particle probability density  $P(\mathbf{r}_1, \dots, \mathbf{r}_N, t)$  by integration over the remaining degrees of freedom:

$$\rho^{(n)}(\mathbf{r}_1, \dots, \mathbf{r}_n, t) = \frac{N!}{(N-n)!} \int d\mathbf{r}_{n+1} \cdots \int d\mathbf{r}_N P(\mathbf{r}_1, \dots, \mathbf{r}_N, t). \quad (26)$$

### 2.2.3. Derivation of DDFT

We now sketch how to derive the DDFT equation (15) from the Smoluchowski picture following the idea of Archer and Evans [97]. Integrating the Smoluchowski equation (24) over the positions of  $N - 1$  particles yields the exact equation

$$\dot{\rho}(\mathbf{r}, t) = D_T \nabla_{\mathbf{r}} \cdot \left( \nabla_{\mathbf{r}} \rho(\mathbf{r}, t) - \frac{\bar{F}(\mathbf{r}, t)}{k_B T} + \frac{\rho(\mathbf{r}, t)}{k_B T} \nabla_{\mathbf{r}} U_1(\mathbf{r}, t) \right) \quad (27)$$

for the one-particle density  $\rho(\mathbf{r}, t)$ , where

$$\bar{F}(\mathbf{r}, t) = - \int d\mathbf{r}' \rho^{(2)}(\mathbf{r}, \mathbf{r}', t) \nabla_{\mathbf{r}} U_2(\mathbf{r} - \mathbf{r}') \quad (28)$$

is an average force, that in turn depends on the nonequilibrium two-particle density  $\rho^{(2)}(\mathbf{r}_1, \mathbf{r}_2, t)$ . This quantity is approximated by an equilibrium expression. To derive this expression, we consider first the equilibrium state of equation (27). This leads to

$$\bar{F}(\mathbf{r}) = k_{\text{B}} T \nabla_{\mathbf{r}} \rho(\mathbf{r}) + \rho(\mathbf{r}) \nabla_{\mathbf{r}} \bar{U}_1(\mathbf{r}), \quad (29)$$

which is the first equation of the Yvon-Born-Green hierarchy, with a “substitute” external potential  $\bar{U}_1(\mathbf{r})$ . In equilibrium, DFT implies

$$\begin{aligned} 0 &= \frac{\delta \Omega(T, \mu, [\rho(\mathbf{r})])}{\delta \rho(\mathbf{r})} = \frac{\delta \mathcal{F}(T, [\rho(\mathbf{r})])}{\delta \rho(\mathbf{r})} - \mu \\ &= k_{\text{B}} T \ln(\Lambda^3 \rho(\mathbf{r})) + \frac{\delta \mathcal{F}_{\text{exc}}(T, [\rho(\mathbf{r})])}{\delta \rho(\mathbf{r})} + \bar{U}_1(\mathbf{r}) \end{aligned} \quad (30)$$

and after application of the gradient operator

$$0 = k_{\text{B}} T \frac{\nabla_{\mathbf{r}} \rho(\mathbf{r})}{\rho(\mathbf{r})} + \nabla_{\mathbf{r}} \frac{\delta \mathcal{F}_{\text{exc}}(T, [\rho(\mathbf{r})])}{\delta \rho(\mathbf{r})} + \nabla_{\mathbf{r}} \bar{U}_1(\mathbf{r}). \quad (31)$$

A comparison of equations (29) and (31) yields

$$\bar{F}(\mathbf{r}) = -\rho(\mathbf{r}) \nabla_{\mathbf{r}} \frac{\delta \mathcal{F}_{\text{exc}}(T, [\rho(\mathbf{r})])}{\delta \rho(\mathbf{r})}. \quad (32)$$

It is postulated, that this relation also holds in nonequilibrium. The nonequilibrium correlations are thus approximated by equilibrium ones at the same  $\rho(\mathbf{r})$  via a suitable “substitute” equilibrium potential  $\bar{U}_1(\mathbf{r})$ . With this *adiabatic approximation*, equation (27) becomes

$$\dot{\rho}(\mathbf{r}, t) = D_{\text{T}} \nabla_{\mathbf{r}} \cdot \left( \nabla_{\mathbf{r}} \rho(\mathbf{r}, t) + \frac{\rho(\mathbf{r})}{k_{\text{B}} T} \nabla_{\mathbf{r}} \frac{\delta \mathcal{F}_{\text{exc}}(T, [\rho(\mathbf{r})])}{\delta \rho(\mathbf{r})} + \frac{\rho(\mathbf{r}, t)}{k_{\text{B}} T} \nabla_{\mathbf{r}} U_1(\mathbf{r}, t) \right), \quad (33)$$

which is the DDFT equation (15).

It is important to note that the DDFT equation (15) is a deterministic equation, i. e., there are no additional noise terms. If noise is added, there would be double counted fluctuations in the equilibrium limit of equation (15) since  $\mathcal{F}(T, [\rho])$  is the *exact* equilibrium functional, which in principle includes all fluctuations. The drawback of the adiabatic approximation, on the other hand, is that a system is trapped for ever in a metastable state. This unphysical behaviour can be changed by adding noise on a phenomenological level though violating the caveat noted above. A pragmatic recipe is to add noise only when fluctuations are needed to push the system out of a metastable state or to regard a fluctuating density field as an initial density profile for subsequent deterministic time evolution via DDFT. In conclusion, the drawback of the adiabatic approximation is that DDFT is some kind of mean-field theory. For example, DDFT as such is unable to predict nucleation rates. It is rather a realistic theory, if a systematic drive pushes the system, as occurs, for example, for crystal growth.

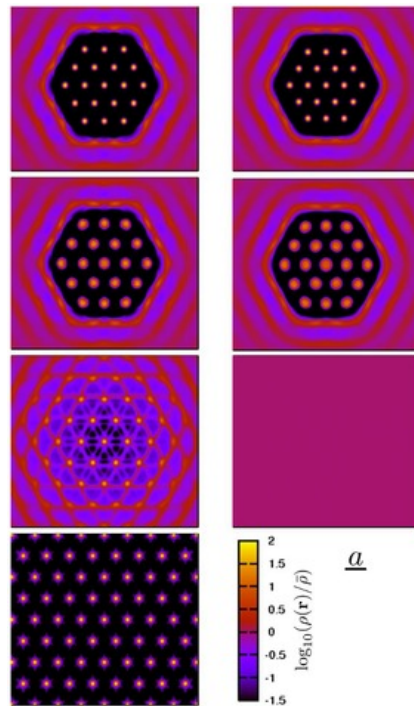


Figure 3. Crystallization starting at a colloidal cluster. The plots show DDFT results for the time-dependent density field.  $A\rho_{\text{ref}} = 0.7$  (left column) and  $A\rho_{\text{ref}} = 0.6$  (right column) at times  $t/\tau_B = 0, 0.001, 0.1, 1$  (from top to bottom) with the area  $A$  of a unit cell of the imposed crystalline seed, the Brownian time  $\tau_B$ , and the lattice constant  $a = (2/(\sqrt{3}\rho_{\text{ref}}))^{1/2}$ . For  $A\rho_{\text{ref}} = 0.7$ , the cluster is compressed in comparison to the stable bulk crystal, but there is still crystal growth possible, while the compression is too high for  $A\rho_{\text{ref}} = 0.6$ . The initial nucleus melts in this case. (Reproduced from S. van Teeffelen, C. N. Likos, and H. Löwen, *Colloidal crystal growth at externally imposed nucleation clusters*, Phys. Rev. Lett. 100 (2008), 108302, no. 10, DOI: 10.1103/PhysRevLett.100.108302 © 2008 by the American Physical Society.)

#### 2.2.4. Application of DDFT to colloidal crystal growth

An important application of DDFT is the description of colloidal crystal growth. In reference [120], DDFT was applied to two-dimensional dipoles, whose dipole moments are perpendicular to a confining plane. These dipoles interact with a repulsive inverse power-law potential  $U_2(\mathbf{r}) = u_0 r^{-3}$ , where  $r = |\mathbf{r}|$  is the interparticle distance. This model can be realized, for example, by superparamagnetic colloids at a water-surface in an external magnetic field [121]. Figures 3 and 4 show DDFT results from reference [120].

In figure 3, the time evolution of the one-particle density of an initial colloidal cluster of 19 particles arranged in a hexagonal lattice is shown. This prescribed cluster is surrounded by an undercooled fluid and can act as a nucleation seed, if its lattice constant is chosen appropriately. The initial cluster either initiates crystal growth (left column in figure 3) or the system relaxes back to the undercooled fluid (right column).

A similar investigation is also possible for other initial configurations like rows of seed particles. Figure 4 shows the crystallization process starting with six infinitely long particle rows of a hexagonal crystal, where a gap separates the first three rows from the remaining three rows. If this gap is not too big, the density peaks rearrange and a growing crystal front emerges.

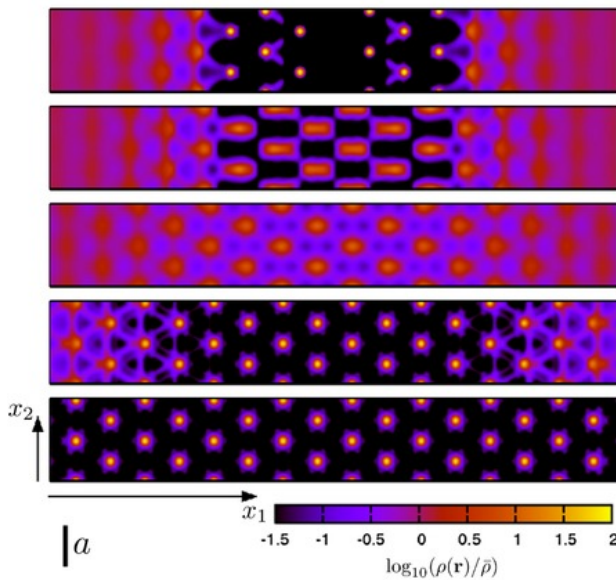


Figure 4. Crystallization starting at two triple-rows of hexagonally crystalline particles that are separated by a gap. The contour plots show the density field of a growing crystal at times  $t/\tau_B = 0, 0.01, 0.1, 0.63, 1$  (from top to bottom). (Reproduced from S. van Teeffelen, C. N. Likos, and H. Löwen, *Colloidal crystal growth at externally imposed nucleation clusters*, Phys. Rev. Lett. 100 (2008), 108302, no. 10, DOI: 10.1103/PhysRevLett.100.108302 © 2008 by the American Physical Society.)

### 2.3. Derivation of the PFC model for isotropic particles from DFT

Though approximate in practice, DFT and DDFT can be regarded to be a high level of microscopic description, which provides a framework to calibrate the more coarse-grained PFC approach. In this section, we at first describe the derivation for spherical interactions in detail and then focus more on anisotropic particles. There are two different aspects of the PFC modelling, which can be justified from DFT respectively DDFT, namely statics and dynamics. The static free energy used in the PFC model was first derived from DFT by Elder and co-workers in 2007 [26], while the corresponding dynamics was derived from DDFT by van Teeffelen and co-workers in 2009 [70]. We follow the basic ideas of these works in the sequel.

#### 2.3.1. Free-energy functional

For the static part, we first of all define a scalar dimensionless order-parameter field  $\psi(\mathbf{r})$ <sup>1</sup> by the relative density deviation

$$\rho(\mathbf{r}) = \rho_{\text{ref}}(1 + \psi(\mathbf{r})) \quad (34)$$

around the prescribed fluid reference density  $\rho_{\text{ref}}$ . This relative density deviation  $\psi(\mathbf{r})$  is considered to be small,  $|\psi(\mathbf{r})| \ll 1$ , and slowly varying in space (on the microscale). The basic steps to derive the PFC free energy are threefold: i) insert the parametrisation (34) into the (microscopic) free-energy functional (5), ii) Taylor-expand systematically in terms of powers of  $\psi(\mathbf{r})$ , iii) perform a gradient expansion [69, 88, 122–124] of  $\psi(\mathbf{r})$ . Consistent with the assumption that density deviations are small, the Ramakrishnan-Yussouff approximation (11) is used as a convenient approximation for the free-energy functional.

<sup>1</sup>Notice that the order-parameter field  $\psi(\mathbf{r})$  introduced here is not identical with the field  $\tilde{\psi}(\tilde{\mathbf{r}})$  in equation (1), although both fields are dimensionless.

For the local ideal gas free-energy functional (6) this yields<sup>2</sup>

$$\mathcal{F}_{\text{id}}[\psi(\mathbf{r})] = F_0 + \rho_{\text{ref}} k_B T \int d\mathbf{r} \left( \psi + \frac{\psi^2}{2} - \frac{\psi^3}{6} + \frac{\psi^4}{12} \right) \quad (35)$$

with the irrelevant constant  $F_0 = \rho_{\text{ref}} V k_B T (\ln(\Lambda^3 \rho_{\text{ref}}) - 1)$ . The Taylor expansion is performed up to fourth order, since this is the lowest order which enables the formation of stable crystalline phases. The nonlocal Ramakrishnan-Yussouff approximation (11) for the approximation of the excess free-energy functional  $\mathcal{F}_{\text{exc}}[\psi(\mathbf{r})]$  is gradient-expanded to make it local. For this purpose, it is important to note that – in the fluid bulk reference state – the direct pair-correlation function  $c^{(2)}(\mathbf{r}_1 - \mathbf{r}_2)$  entering into the Ramakrishnan-Yussouff theory has the same symmetry as the interparticle interaction potential  $U_2(\mathbf{r}_1 - \mathbf{r}_2)$ . For radially symmetric interactions (i. e., spherical particles), there is both *translational* and *rotational* invariance implying

$$c^{(2)}(\mathbf{r}_1, \mathbf{r}_2) \equiv c^{(2)}(\mathbf{r}_1 - \mathbf{r}_2) \equiv c^{(2)}(r) \quad (36)$$

with the relative distance  $r = |\mathbf{r}_1 - \mathbf{r}_2|$ . Then, as a consequence of equation (36), the Ramakrishnan-Yussouff approximation is a convolution integral. Consequently, a Taylor expansion of the Fourier transform  $\tilde{c}^{(2)}(\mathbf{k})$  of the direct correlation function in Fourier space (around the wave vector  $\mathbf{k} = \mathbf{0}$ )

$$\tilde{c}^{(2)}(\mathbf{k}) = \tilde{c}_0^{(2)} + \tilde{c}_2^{(2)} \mathbf{k}^2 + \tilde{c}_4^{(2)} \mathbf{k}^4 + \dots \quad (37)$$

with expansion coefficients  $\tilde{c}_i^{(2)}$  becomes a gradient expansion in real space

$$c^{(2)}(\mathbf{r}) = c_0^{(2)} - c_2^{(2)} \nabla_{\mathbf{r}}^2 + c_4^{(2)} \nabla_{\mathbf{r}}^4 \mp \dots \quad (38)$$

with the gradient expansion coefficients  $c_i^{(2)}$ . Clearly, gradients of odd order vanish due to parity inversion symmetry  $c^{(2)}(-\mathbf{r}) = c^{(2)}(\mathbf{r})$  of the direct pair-correlation function.

The gradient expansion up to fourth order is the lowest one that makes stable periodic density fields possible. We finally obtain

$$\mathcal{F}_{\text{exc}}[\psi(\mathbf{r})] = F_{\text{exc}} - \frac{\rho_{\text{ref}}}{2} k_B T \int d\mathbf{r} \left( A_1 \psi^2 + A_2 \psi \nabla_{\mathbf{r}}^2 \psi + A_3 \psi \nabla_{\mathbf{r}}^4 \psi \right) \quad (39)$$

with the irrelevant constant  $F_{\text{exc}} = \mathcal{F}_{\text{exc}}^{(0)}(\rho_{\text{ref}})$  and the coefficients

$$A_1 = 4\pi\rho_{\text{ref}} \int_0^\infty dr r^2 c^{(2)}(r), \quad A_2 = \frac{2}{3}\pi\rho_{\text{ref}} \int_0^\infty dr r^4 c^{(2)}(r), \quad A_3 = \frac{\pi\rho_{\text{ref}}}{30} \int_0^\infty dr r^6 c^{(2)}(r) \quad (40)$$

that are moments of the fluid direct correlation function  $c^{(2)}(r)$ .

Finally, the external free-energy functional (7) can be written as

$$\mathcal{F}_{\text{ext}}[\psi(\mathbf{r})] = F_{\text{ext}} + \rho_{\text{ref}} \int d\mathbf{r} \psi(\mathbf{r}) U_1(\mathbf{r}) \quad (41)$$

<sup>2</sup>This Taylor approximation of the logarithm has the serious consequence that the non-negative-density constraint  $\rho(\mathbf{r}) \geq 0$  gets lost in the PFC model.



with the irrelevant constant  $F_{\text{ext}} = \rho_{\text{ref}} \int d\mathbf{r} U_1(\mathbf{r})$ . We add as a comment here that this external part is typically neglected in most of the PFC calculations. Altogether, we obtain

$$\mathcal{F}[\psi(\mathbf{r})] = \rho_{\text{ref}} k_{\text{B}} T \int d\mathbf{r} \left( A'_1 \psi^2 + A'_2 \psi \nabla_{\mathbf{r}}^2 \psi + A'_3 \psi \nabla_{\mathbf{r}}^4 \psi - \frac{\psi^3}{6} + \frac{\psi^4}{12} \right) \quad (42)$$

for the total Helmholtz free-energy functional and the scaled coefficients

$$A'_1 = \frac{1}{2}(1 - A_1), \quad A'_2 = -\frac{1}{2}A_2, \quad A'_3 = -\frac{1}{2}A_3 \quad (43)$$

are used for abbreviation, where the coefficient  $A'_2$  should be positive in order to favour non-uniform phases and the last coefficient  $A'_3$  is assumed to be positive for stability reasons. By comparison of equation (42) with the original PFC model (1), that was initially proposed on the basis of general symmetry considerations in reference [12], analytic expressions can be assigned to the unknown coefficients in the original PFC model: when we write the order-parameter field in equation (1) as  $\tilde{\psi}(\mathbf{r}) = \alpha(1 - 2\psi(\mathbf{r}))$  with a constant  $\alpha$  and neglect constant contributions as well as terms linear in  $\psi(\mathbf{r})$  in the free-energy density, we obtain the relations

$$\alpha = \frac{1}{\sqrt{24A'_3}}, \quad \tilde{\mathcal{F}} = \frac{1}{12\rho_{\text{ref}} k_{\text{B}} T A'_3} \mathcal{F}, \quad \beta = \frac{1}{8A'_3} - \frac{A'_1}{A'_3} + \frac{A'_2}{4A'_3}, \quad k_0 = \sqrt{\frac{A'_2}{2A'_3}} \quad (44)$$

between the coefficients in equations (1) and (42).

### 2.3.2. Dynamical equations

We turn to the dynamics of the PFC model and derive it here from DDFT. Inserting the representation (34) for the one-particle density field into the DDFT equation (15), we obtain for the dynamical evolution of the order-parameter field  $\psi(\mathbf{r}, t)$

$$\frac{\partial \psi(\mathbf{r}, t)}{\partial t} = D_{\text{T}} \nabla_{\mathbf{r}} \cdot \left( (1 + \psi) \nabla_{\mathbf{r}} \left( 2A'_1 \psi + 2A'_2 \nabla_{\mathbf{r}}^2 \psi + 2A'_3 \nabla_{\mathbf{r}}^4 \psi - \frac{\psi^2}{2} + \frac{\psi^3}{3} \right) \right). \quad (45)$$

This dynamical equation (called PFC1 model in reference [70]) still differs from the original dynamical equation of the PFC model. The latter can be gained by a further constant-mobility approximation (CMA), where the space- and time-dependent mobility  $D_{\text{T}}\rho(\mathbf{r}, t)$  in the DDFT equation is replaced by the constant mobility  $D_{\text{T}}\rho_{\text{ref}}$ . The resulting dynamical equation (called PFC2 model in reference [70]) coincides with the original PFC dynamics given by

$$\frac{\partial \psi(\mathbf{r}, t)}{\partial t} = D_{\text{T}} \nabla_{\mathbf{r}}^2 \left( 2A'_1 \psi + 2A'_2 \nabla_{\mathbf{r}}^2 \psi + 2A'_3 \nabla_{\mathbf{r}}^4 \psi - \frac{\psi^2}{2} + \frac{\psi^3}{3} \right) \quad (46)$$

for the time-dependent translational density  $\psi(\mathbf{r}, t)$ . We remark that this dynamical equation can also be derived from an equivalent dissipation functional  $\mathfrak{R}$  known from linear irreversible thermodynamics [125–127]. A further transformation of this equation to the standard form of the dynamic PFC model will be established in section 3.1.1.



Figure 5. Colloidal crystal growth within DDFT (upper panel) and the PFC1 model (lower panel). The crystallization starts with an initial nucleus of 5 and 11 rows of hexagonally crystalline particles, respectively. The density field of the growing crystal is shown at times  $t/\tau_B = 0, 0.5, 1, 1.5$ . (Reproduced from S. van Teeffelen, R. Backofen, A. Voigt, and H. Löwen, *Derivation of the phase-field-crystal model for colloidal solidification*, Phys. Rev. E 79 (2009), 051404, no. 5, DOI: 10.1103/PhysRevE.79.051404 © 2009 by the American Physical Society.)

### 2.3.3. Colloidal crystal growth: DDFT versus PFC modelling

Results of the PFC1 model, the PFC2 model, and DDFT are compared for colloidal crystal growth in reference [70]. Figures 5-7 show the differences for the example of a growing crystal front starting at the edge of a prescribed hexagonal crystal. The underlying colloidal systems are the same as in section 2.2.4. In figure 5, the time evolution of the one-particle density is shown for DDFT and for the PFC1 model. The PFC2 model leads to results very similar to those for the PFC1 model and is therefore not included in this figure.

Two main differences in the results of DDFT and of the PFC1 model are obvious: first, the density peaks are much higher and narrower in the DDFT results than for the PFC1 model. While these peaks can be approximated by Gaussians in the case of DDFT, they are much broader sinusoidal modulations for the PFC1 model. Secondly, also the width of the crystal front obtained within DDFT is considerably smaller than in the PFC approach.

These qualitative differences can also be observed in figure 6. There, the laterally averaged density  $\rho_{x_2}(x_1, t) = \langle \rho(\mathbf{r}, t) \rangle_{x_2}$  associated with the plots in figure 5 is shown, where  $\langle \cdot \rangle_{x_2}$  denotes an average with respect to  $x_2$ . A further comparison of DDFT and the PFC approaches is possible with respect to the velocity  $v_f$  of the crystallization front. The corresponding results are shown in figure 7 in dependence of the total coupling constant  $\Gamma = u_0 v^{3/2} / (k_B T)$  and the relative coupling constant  $\Delta\Gamma = \Gamma - \Gamma_f$ , where  $\Gamma_f$  denotes the coupling constant of freezing. Due to the power-law potential of the considered colloidal particles, their behaviour is completely characterized by the dimensionless coupling parameter  $\Gamma$ . When plotted versus  $\Delta\Gamma$ , the growth velocity of the PFC1 model is in slightly better agreement than that of the PFC2 model.

## 3. Phase-field-crystal modelling in condensed matter physics

The original PFC model has the advantage over most other microscopic techniques, such as molecular-dynamics (MD) simulations, that the time evolution of the system can be studied on the diffusive time scale making the long-time behaviour and the large-scale structures accessible [12, 50]. As already outlined in section 2.2, we note that the diffusion-controlled relaxation dynamics the original PFC model assumes is relevant for micron-scale colloidal particles in carrier fluid [70, 120], where the self-diffusion of the particles is expected to be the dominant way of density relaxation. For normal liquids, the hydrodynamic mode of density relaxation is expected to dominate. The modified PFC (MPFC) model introduces linearised

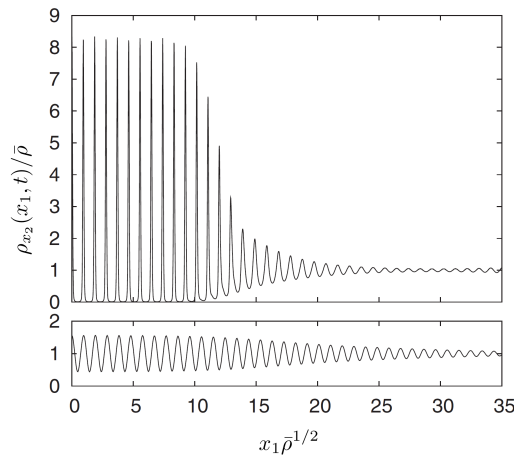


Figure 6. Comparison of DDFT (upper panel) and PFC1 (lower panel) results. For an analogous situation as in figure 5, this plot shows the laterally averaged density  $\rho_{x_2}(x_1, t) = \langle \rho(\mathbf{r}, t) \rangle_{x_2}$  at  $t = \tau_B$ . (Reproduced from S. van Teeffelen, R. Backofen, A. Voigt, and H. Löwen, *Derivation of the phase-field-crystal model for colloidal solidification*, Phys. Rev. E 79 (2009), 051404, no. 5, DOI: 10.1103/PhysRevE.79.051404 © 2009 by the American Physical Society.)

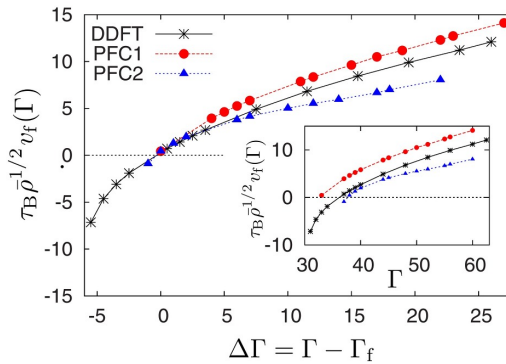


Figure 7. Comparison of DDFT, the PFC1 model, and the PFC2 model [70]. The plot shows the velocity  $v_f$  of a crystallization front in the (11)-direction in dependence of the relative coupling constant  $\Delta\Gamma = \Gamma - \Gamma_f$  with the total coupling constant  $\Gamma$  and the coupling constant of freezing  $\Gamma_f$ . In the inset, the velocity  $v_f$  is shown in dependence of  $\Gamma$ . (Reproduced from S. van Teeffelen, R. Backofen, A. Voigt, and H. Löwen, *Derivation of the phase-field-crystal model for colloidal solidification*, Phys. Rev. E 79 (2009), 051404, no. 5, DOI: 10.1103/PhysRevE.79.051404 © 2009 by the American Physical Society.)

hydrodynamics, realized via incorporating a term proportional to the second time derivative of the particle density into the EOM [51, 128], yielding a two-time-scale density relaxation: a fast acoustic process in addition to the long time diffusive relaxation of the original PFC model. A three-time-scale extension incorporates phonons into the PFC model [129, 130]. Another interesting group of models have been obtained by coarse-graining the PFC approaches [19, 20, 131], leading to equations of motion that describe the spatiotemporal evolution of the Fourier amplitudes and the respective phase information characterizing the particle density field. Combined with adaptive grid schemes, the amplitude equation models are expected to become a numerically especially efficient class of the PFC models of crystallization [20].

Finally, we address here recent advances in the modelling of molecules or liquid crystalline systems, which are composed of anisotropic particles. There is a large number of molecular and colloidal realizations of these non-spherical particles. The simplest non-spherical shape is rotationally symmetric about a certain axis (like rods, platelets, and dumbbells) and is solely described by an additional orientation vector. Liquid crystalline systems show an intricate freezing behaviour in equilibrium, where mesophases occur, that can possess both orientational and

translational ordering. Here, we show that the microscopic DFT approach for liquid crystals provides an excellent starting point to derive PFC-type models for liquid crystals. This gives access to the phase diagram of liquid crystalline phases and to their dynamics promising a flourishing future to predict many fundamentally important processes on the microscopic level.

### 3.1. The original PFC model and its generalisations

The original PFC model has several equivalent formulations and extensions that we review in this section. We first address the single-component PFC models. Then, an overview of their binary generalisations will be given. In both cases, complementing section 2, we start with presenting different forms of the free-energy functional, followed by a summary of specific forms of the EOM and of the Euler-Lagrange equation (ELE). Finally, we review the numerical methods applied for solving the EOM and ELE as well as various approaches for the amplitude equations.

#### 3.1.1. Single-component PFC models

##### 3.1.1.1. The free energy.

*The single-mode PFC model.* The earliest formulation of the single-mode PFC (1M-PFC) model [12, 50] has been derived as a SH model with conserved dynamics to incorporate mass conservation. Accordingly, the dimensionless free energy of the heterogeneous system is given by the usual SH expression (1). We note that in equations (1) and (53) the analogous quantities differ by only appropriate numerical factors originating from the difference in the length scales.

As already outlined in section 2.3, the free energy of the earliest and simplest PFC model [12] has been re-derived [26] from that of the perturbative DFT of Ramakrishnan and Yussouff [85], in which the free-energy difference  $\Delta\mathcal{F} = \mathcal{F} - \bar{\mathcal{F}}^1$  of the crystal relative to a reference liquid of particle density  $\rho_{\text{ref}}$  and free energy  $\bar{\mathcal{F}}$  is expanded with respect to the local density difference  $\Delta\rho(\mathbf{r}) = \rho(\mathbf{r}) - \rho_{\text{ref}}$ , while retaining the terms up to the two-particle term (see section 2.3.1):

$$\frac{\mathcal{F}}{k_{\text{B}}T} = \int d\mathbf{r} \left( \rho \ln \left( \frac{\rho}{\rho_{\text{ref}}} \right) - \Delta\rho \right) - \frac{1}{2} \int d\mathbf{r}_1 \int d\mathbf{r}_2 \Delta\rho(\mathbf{r}_1) c^{(2)}(\mathbf{r}_1, \mathbf{r}_2) \Delta\rho(\mathbf{r}_2) + \dots \quad (47)$$

Fourier expanding the particle density, one finds that for the solid  $\rho_{\text{s}} = \rho_{\text{ref}} (1 + \eta_{\text{s}} + \sum_{\mathbf{K}} A_{\mathbf{K}} \exp(i\mathbf{K} \cdot \mathbf{r}))$ , where  $\eta_{\text{s}}$  is the fractional density change upon freezing, while  $\mathbf{K}$  are reciprocal lattice vectors (RLVs) and  $A_{\mathbf{K}}$  the respective Fourier amplitudes. Introducing the reduced number density  $\psi = (\rho - \rho_{\text{ref}})/\rho_{\text{ref}} = \eta_{\text{s}} + \sum_{\mathbf{K}} A_{\mathbf{K}} \exp(i\mathbf{K} \cdot \mathbf{r})$  one obtains

$$\begin{aligned} \frac{\mathcal{F}}{\rho_{\text{ref}} k_{\text{B}}T} &= \int d\mathbf{r} ((1 + \psi) \ln(1 + \psi) - \psi) \\ &\quad - \frac{\rho_{\text{ref}}}{2} \int d\mathbf{r}_1 \int d\mathbf{r}_2 \psi(\mathbf{r}_1) c^{(2)}(|\mathbf{r}_1 - \mathbf{r}_2|) \psi(\mathbf{r}_2) + \dots \end{aligned} \quad (48)$$

Expanding next  $c^{(2)}(|\mathbf{r}_1 - \mathbf{r}_2|)$  in Fourier space,  $\tilde{c}^{(2)}(k) \approx \tilde{c}_0^{(2)} + \tilde{c}_2^{(2)} k^2 + \tilde{c}_4^{(2)} k^4 + \dots$ , where  $\tilde{c}^{(2)}(k)$  has its first peak at  $k = 2\pi/R_{\text{p}}$ , the signs of the coefficients alternate.

<sup>1</sup>To keep the notation simple, we ignore  $\bar{\mathcal{F}}$  and write  $\mathcal{F}$  instead of  $\Delta\mathcal{F}$  throughout this article.

(Here,  $R_p$  is the inter-particle distance.) Introducing the dimensionless two-particle direct correlation function  $c(k) = \rho_{\text{ref}} \tilde{c}^{(2)}(k) \approx \sum_{j=0}^m c_{2j} k^{2j} = \sum_{j=0}^m b_{2j} (kR_p)^{2j}$ , which is related to the structure factor as  $S(k) = 1/(1 - c(k))$ , and integrating the second term on the right-hand-side of equation (48) with respect to  $\mathbf{r}_2$  and finally replacing  $\mathbf{r}_1$  by  $\mathbf{r}$ , the free-energy difference can be rewritten as

$$\frac{\mathcal{F}}{\rho_{\text{ref}} k_B T} \approx \int d\mathbf{r} \left( (1 + \psi) \ln(1 + \psi) - \psi - \frac{\psi}{2} \left( \sum_{j=0}^m (-1)^j c_{2j} \nabla_{\mathbf{r}}^{2j} \right) \psi \right). \quad (49)$$

The reference liquid is not necessarily the initial liquid. Thus, we have here two parameters to control the driving force for solidification: the initial liquid number density  $\rho_0$  (corresponding to a reduced initial density of  $\psi_0$ ) and the temperature  $T$ , if the direct correlation function depends on temperature. Taylor-expanding  $\ln(1 + \psi)$  for small  $\psi$  one obtains

$$\frac{\mathcal{F}}{\rho_{\text{ref}} k_B T} \approx \int d\mathbf{r} \left( \frac{\psi^2}{2} - \frac{\psi^3}{6} + \frac{\psi^4}{12} - \frac{\psi}{2} \left( \sum_{j=0}^m (-1)^j c_{2j} \nabla_{\mathbf{r}}^{2j} \right) \psi \right). \quad (50)$$

For  $m = 2$ , corresponding to the earliest version of the PFC model [12], and taking the alternating sign of the expansion coefficients of  $\tilde{c}_i^{(2)}$  into account, equation (49) transforms to the following form:

$$\frac{\mathcal{F}}{\rho_{\text{ref}} k_B T} \approx \int d\mathbf{r} \left( \frac{\psi^2}{2} (1 + |b_0|) + \frac{\psi}{2} (|b_2| R_p^2 \nabla_{\mathbf{r}}^2 + |b_4| R_p^4 \nabla_{\mathbf{r}}^4) \psi - \frac{\psi^3}{6} + \frac{\psi^4}{12} \right). \quad (51)$$

Introducing the new variables

$$\begin{aligned} B_1 = 1 + |b_0| = 1 - c_0 & \quad [= (1/\kappa)/(\rho_{\text{ref}} k_B T), \text{ where } \kappa \text{ is the compressibility}], \\ B_s = |b_2|^2/(4|b_4|) & \quad [= K/(\rho_{\text{ref}} k_B T), \text{ where } K \text{ is the bulk modulus}], \\ R = R_p(2|b_4|/|b_2|)^{1/2} & \quad [= \text{the new length scale } (x = R\tilde{x}), \text{ which is now related to} \\ & \quad \text{the position of the maximum of the Taylor expanded } \tilde{c}^{(2)}(k)], \end{aligned}$$

and a multiplier  $v$  for the  $\psi^3$ -term (that accounts for the zeroth-order contribution from three-particle correlations), one obtains the form used by Berry et al. [36, 46]:

$$\begin{aligned} \mathcal{F} &= \int d\mathbf{r} f[\psi] \\ &= \rho_{\text{ref}} k_B T \int d\mathbf{r} \left( \frac{\psi}{2} (B_1 + B_s (2R^2 \nabla_{\mathbf{r}}^2 + R^4 \nabla_{\mathbf{r}}^4)) \psi - v \frac{\psi^3}{6} + \frac{\psi^4}{12} \right). \end{aligned} \quad (52)$$

Here,  $f[\psi]$  denotes the full (dimensional) free-energy density.

*The Swift-Hohenberg-type dimensionless form.* Introducing a new set of variables,  $x = R\tilde{x}$ ,  $\psi = (3B_s)^{1/2} \tilde{\psi}$ ,  $\mathcal{F} = (3\rho_{\text{ref}} k_B T R^d B_s^2) \tilde{\mathcal{F}}$ , where  $d$  is the number of spatial dimensions, the free energy can be transcribed into the following dimensionless form:

$$\tilde{\mathcal{F}} = \int d\tilde{\mathbf{r}} \left( \frac{\tilde{\psi}}{2} (-\epsilon + (1 + \nabla_{\tilde{\mathbf{r}}}^2)^2) \tilde{\psi} + p \frac{\tilde{\psi}^3}{3} + \frac{\tilde{\psi}^4}{4} \right). \quad (53)$$

Here,  $p = -(v/2)(3/B_s)^{1/2} = -v(3|b_4|/|b_2|^2)^{1/2}$  and  $\epsilon = -\Delta B/B_s = -((1 + |b_0|)/(|b_2|^2/(4|b_4|)) - 1)$ , while  $\tilde{\psi} = \psi/(3B_s)^{1/2}$ . The quantities involved in equa-

tion (53) are all dimensionless. Using the appropriate length unit, this expression becomes equivalent to equation (1) for  $p = 0$ .

Equation (53) suggests that the  $m = 2$  PFC model contains only two dimensionless similarity parameters,  $\epsilon$  and  $p$ , composed of the original model parameters. We note finally that even the third-order term can be eliminated. In the respective  $p' = 0$  SH model (1), the state ( $\epsilon' = \epsilon + p^2/3$ ,  $\psi' = \tilde{\psi} + p/3$ ) corresponds to the state ( $\epsilon, \tilde{\psi}$ ) of the original  $p \neq 0$  model. This transformation leaves the grand canonical potential difference, the ELE (see section 3.1.1.3), and the EOM (see section 3.1.1.2) invariant. Accordingly, it is sufficient to address the case  $p = 0$ .

We stress here that in these models the approximation for the two-particle direct correlation function leads to a well defined wavelength of the density waves the system tends to realize (hence the name “single-mode PFC” (1M-PFC) model). Accordingly, any periodic density distribution that honours this wavelength represents a local minimum of the free energy. Indeed, the 1M-PFC model has stability domains for the bcc, fcc, and hcp structures (see section 3.1.1.1). Furthermore, elasticity and crystal anisotropies are automatically present in the model.

Model parameters of the SH formulation have been deduced to fit to the properties of bcc Fe by Wu and Karma [40].

*The two-mode PFC model.* An attempt has been made to formulate a free energy that prefers the fcc structure at small  $\epsilon$  values [132], where a linear elastic behaviour persists. To achieve this, two well defined wavelengths were used (first and second neighbour RLVs), hence the name “two-mode PFC” (2M-PFC) model. The respective free-energy functional contains two new parameters:

$$\tilde{\mathcal{F}} = \int d\tilde{\mathbf{r}} \left( \frac{\tilde{\psi}}{2} \left( -\epsilon + (1 + \nabla_{\tilde{\mathbf{r}}}^2)^2 (R_1 + (k_{\text{rel}}^2 + \nabla_{\tilde{\mathbf{r}}}^2)^2) \right) \tilde{\psi} + \frac{\tilde{\psi}^4}{4} \right). \quad (54)$$

Here,  $R_1$  controls the relative stability of the fcc and bcc structures, while  $k_{\text{rel}}$  is the ratio of the two wave numbers ( $k_{\text{rel}} = 2/\sqrt{3}$  for fcc using the (111) and (200) RLVs). Remarkably, the 1M-PFC model can be recovered for  $R_1 \rightarrow \infty$ . Model parameters have been deduced to fit to the properties of fcc Fe by Wu and Karma [132].

We note finally that the 1M-PFC and 2M-PFC models can be cast into a form that interpolates between them by varying a single parameter  $\lambda = R_1/(1 + R_1) \in [0, 1]$  as follows [35]:

$$\tilde{\mathcal{F}} = \int d\tilde{\mathbf{r}} \left( \frac{\tilde{\psi}}{2} \left( -\epsilon + (1 + \nabla_{\tilde{\mathbf{r}}}^2)^2 (\lambda + (1 - \lambda)(k_{\text{rel}}^2 + \nabla_{\tilde{\mathbf{r}}}^2)^2) \right) \tilde{\psi} + \frac{\tilde{\psi}^4}{4} \right). \quad (55)$$

This expression recovers the 1M-PFC model limit for  $\lambda = 1$  ( $R_1 \rightarrow \infty$ ).

*The eighth-order fitting PFC model.* To approximate real bcc materials better, an eighth-order expansion of the Fourier transform of the direct correlation function around its maximum ( $k = k_m$ ) has been performed recently, leading to what is termed the eighth-order fitting version of the phase-field-crystal (EOF-PFC) model [133]:

$$\tilde{c}^{(2)}(k) \approx \tilde{c}^{(2)}(k_m) - \Gamma \left( \frac{k^2}{k_m^2} - 1 \right)^2 - E_B \left( \frac{k^2}{k_m^2} - 1 \right)^4. \quad (56)$$

The expansion parameters were then fixed so that the position, height, and the second derivative of  $\tilde{c}^{(2)}(k)$  are accurately recovered. This is ensured by

$$\Gamma = -\frac{k_m^2 (\tilde{c}^{(2)})''(k_m)}{8} \quad \text{and} \quad E_B = \tilde{c}^{(2)}(k_m) - \tilde{c}^{(2)}(0) - \Gamma. \quad (57)$$

With this choice of the model parameters and using relevant data for Fe from reference [40], they reported a fair agreement with MD simulation results for the volume change upon melting, the bulk moduli of the liquid and solid phases, and for the magnitude and anisotropy of the bcc-liquid interfacial free energy [133].

*Attempts to control the crystal structure in PFC models.* Greenwood and co-workers [134, 135] (GRP-PFC model) have manipulated the two-particle direct correlation function so that its peaks prefer the desired structural correlations – an approach that enables them to study transitions between the bcc, fcc, hcp, and sc structures. Wu, Plapp, and Voorhees [136] have investigated the possibility to control crystal symmetries within the PFC method via tuning nonlinear resonances. They have proposed a general recipe for developing free-energy functionals that realize coexistence between the liquid and periodic phases of desired crystal symmetries, and have illustrated this via presenting a free-energy functional that leads to square-lattice-liquid coexistence in 2D. A possible extension of the method to the 3D case for simple cubic (sc) structures has also been discussed.

*The vacancy PFC model.* The vacancy PFC (VPFC) model is an important extension of the PFC model that adds a term to the free energy that penalizes the negative values of the particle density, allowing thus for an explicit treatment of vacancies [56]:

$$\tilde{\mathcal{F}} = \int d\tilde{\mathbf{r}} \left( \frac{\tilde{\psi}}{2} \left( -\beta + (k_0^2 + \nabla_{\tilde{\mathbf{r}}}^2)^2 \right) \tilde{\psi} + \frac{\tilde{\psi}^4}{4} + h(|\tilde{\psi}^3| - \tilde{\psi}^3) \right). \quad (58)$$

Here,  $h$  in the last term on the right-hand-side is a constant. The new term is a piecewise function that is zero for  $\tilde{\psi} > 0$  and positive for  $\tilde{\psi} < 0$ . It is then possible to obtain a mixture of density peaks (particles) and vacant areas (where  $\tilde{\psi} \approx 0$ ), resembling thus to snapshots of liquid configurations or crystalline structures with defects. This allows structural modelling of the fluid phase and is an important step towards combining the PFC model with fluid flow. The same approach has been used to address the dynamics of glasses [47].

*The anisotropic PFC model.* Recently, Prieler et al. [137] have extended the PFC approach by replacing the Laplacian in equation (1) by more general differential operators allowing spatial anisotropy. Doing so and setting  $\tau = -(k_0^2 - \beta)$  one arrives at the dimensionless free-energy functional of the so-called anisotropic PFC (APFC) model:

$$\tilde{\mathcal{F}} = \int d\tilde{\mathbf{r}} \left( \frac{\tilde{\psi}}{2} \left( -\tau + a_{ij} \frac{\partial^2}{\partial \tilde{x}_i \partial \tilde{x}_j} + b_{ijkl} \frac{\partial^4}{\partial \tilde{x}_i \partial \tilde{x}_j \partial \tilde{x}_k \partial \tilde{x}_l} \right) \tilde{\psi} + \frac{\tilde{\psi}^4}{4} \right). \quad (59)$$

Here,  $a_{ij}$  is a symmetric matrix and  $b_{ijkl}$  is a tensor of rank 4 with the symmetry of an elastic tensor:  $i \leftrightarrow j, k \leftrightarrow l, (i, j) \leftrightarrow (k, l)$  [137]. Choudhary et al. [138, 139] proved that based on a functional of the form (59) further crystal lattices can be

assessed as hexagonal, bcc, and corresponding sheared structures, for which they have presented the elastic parameters and identified the stationary states.

**3.1.1.2. The equation of motion.** In the PFC models, different versions of the EOM have been employed. In all cases, conservative dynamics is assumed on the ground that mass conservation needs to be satisfied. (The original SH model differs from the 1M-PFC model only in the EOM, for which the SH model assumes non-conserved dynamics.) Most of the PFC models rely on an overdamped conservative EOM (see, e. g., references [12, 26–39, 43, 46, 50, 70, 132, 137, 140]). In fact, this means that the particle density relaxes diffusively, a feature more characteristic to colloidal systems than to molten metals: in colloidal systems of particles floating in a carrier fluid, Brownian motion is the dominant mechanism of particle motion, whose properties are captured reasonably well by overdamped dynamics [38, 70, 120] (see also section 2.2). On the contrary, in molten metals a density deficit can be reduced by a hydrodynamic flow of particles. Apparently, a proper dynamics of the solid (presence of phonons) requires three time scales [129, 130]. While the overdamped model has only the long diffusive time scale, the MPFC model realizes linearised hydrodynamics via adding a term proportional to the second time derivative of the density field. This new term leads to the appearance of an acoustic relaxation of the density (not true acoustic phonons) on a fast time scale, in addition to the slow diffusive relaxation at later stages [51, 128]. In a recent work, phonon dynamics, that acts on a third time scale, has also been introduced into the PFC model [129]. It has been shown that there exists a scale window, in which the longitudinal part of the full three-scale model reduces to the MPFC model, whereas the linearised hydrodynamics of the latter converges to the diffusive dynamics of the original PFC model for sufficiently long times [129, 130].

*The overdamped equation of motion.* In the majority of the PFC simulations, an overdamped conserved dynamics is assumed [that is analogous to the DDFT EOM (15) for colloidal systems, however, assuming here a constant mobility coefficient,  $M_\rho = \rho_0 D_T / (k_B T)$ ]. Accordingly, the (dimensional) EOM has the form

$$\frac{\partial \rho}{\partial t} = \nabla_{\mathbf{r}} \cdot \left( M_\rho \nabla_{\mathbf{r}} \frac{\delta \mathcal{F}}{\delta \rho} \right) + \zeta_\rho, \quad (60)$$

where  $\zeta_\rho$  stands for the fluctuations of the density flux, whose correlator reads as  $\langle \zeta_\rho(\mathbf{r}, t) \zeta_\rho(\mathbf{r}', t') \rangle = -2M_\rho k_B T \nabla_{\mathbf{r}}^2 \delta(\mathbf{r} - \mathbf{r}') \delta(t - t')$ . (For a discretised form of the conserved noise see reference [141].)

Changing from variable  $\rho$  to  $\psi$ , introducing  $M_\psi = ((1 + \psi_0) D_T / (\rho_{\text{ref}} k_B T))$ , scaling time and distance as  $t = \tau \tilde{t}$  and  $x = R_p \tilde{x}$ , where  $\tau = R_p / (D_T (1 + \psi_0))$ , and inserting the free energy from equation (51), one obtains the following dimensionless EOM:

$$\frac{\partial \psi}{\partial \tilde{t}} = \nabla_{\tilde{\mathbf{r}}}^2 \left( \psi (1 + |b_0|) + \sum_{j=1}^m |b_{2j}| \nabla_{\tilde{\mathbf{r}}}^{2j} \psi - \frac{\psi^2}{2} + \frac{\psi^3}{3} \right) + \zeta_\psi \quad (61)$$

with  $\langle \zeta_\psi(\tilde{\mathbf{r}}, \tilde{t}) \zeta_\psi(\tilde{\mathbf{r}}', \tilde{t}') \rangle = -(2 / (\rho_{\text{ref}} R_p^d)) \nabla_{\tilde{\mathbf{r}}}^2 \delta(\tilde{\mathbf{r}} - \tilde{\mathbf{r}}') \delta(\tilde{t} - \tilde{t}')$ . Analogously, the EOM corresponding to equation (52) has the form

$$\frac{\partial \psi}{\partial \tilde{t}} = \nabla_{\tilde{\mathbf{r}}} \cdot \left( M_\psi \rho_{\text{ref}} k_B T \nabla_{\tilde{\mathbf{r}}} \left( (B_1 + B_s (R^2 \nabla_{\tilde{\mathbf{r}}}^2 + R^4 \nabla_{\tilde{\mathbf{r}}}^4)) \psi - v \frac{\psi^2}{2} + \frac{\psi^3}{3} \right) \right) + \zeta'_\psi, \quad (62)$$



where  $\langle \zeta'_\psi(\mathbf{r}, t) \zeta'_\psi(\mathbf{r}', t') \rangle = -2M_\psi k_B T \nabla_{\mathbf{r}}^2 \delta(\mathbf{r} - \mathbf{r}') \delta(t - t')$ .

*Dimensionless form in Swift-Hohenberg fashion.* Introducing the variables  $t = \tau \tilde{t}$ ,  $x = R \tilde{x}$ , and  $\psi = (3B_s)^{1/2} \tilde{\psi} = (3B_s)^{1/2} (\psi' - p/3)$  into equation (62), where  $\tau = R^2 / (B_s M_\psi \rho_{\text{ref}} k_B T)$ , the EOM can be written in the form

$$\frac{\partial \psi'}{\partial \tilde{t}} = \nabla_{\tilde{\mathbf{r}}}^2 \left( \left( -\epsilon' + (1 + \nabla_{\tilde{\mathbf{r}}}^2)^2 \right) \psi' + \psi'^3 \right) + \zeta, \quad (63)$$

where  $\epsilon' = \epsilon + p^2/3 = -(\Delta B - (v/2)^2)/B_s = -((1 + |b_0|)/(|b_2|^2/(4|b_4|)) - (1 + v^2(|b_4|/|b_2|^2)))$  and the dimensionless noise strength is  $\alpha = 2/(3B_s^2 \rho_{\text{ref}} R^d) = 2^{5-d/2} |b_4|^{2-d/2} / (3R_p^d \rho_{\text{ref}} |b_2|^{4-d/2})$ , while the correlator for the dimensionless noise reads as  $\langle \zeta(\tilde{\mathbf{r}}, \tilde{t}) \zeta(\tilde{\mathbf{r}}', \tilde{t}') \rangle = -\alpha \nabla_{\tilde{\mathbf{r}}}^2 \delta(\tilde{\mathbf{r}} - \tilde{\mathbf{r}}') \delta(\tilde{t} - \tilde{t}')$ .

Summarizing, the dynamical  $m = 2$  1M-PFC model has two dimensionless similarity parameters  $\epsilon'$  and  $\alpha$  composed of the original (physical) model parameters. This is the generic form of the  $m = 2$  1M-PFC model; some other formulations [36, 46] can be transformed into this form.

*The modified PFC model.* Acoustic relaxation has been partly incorporated by applying an underdamped EOM. Stefanovic, Haataja, and Provatas [51] have incorporated a second order time derivative into the EOM of their modified PFC (MPFC) model, which extends the previous PFC formalism by generating dynamics on two time scales:

$$\frac{\partial^2 \rho}{\partial t^2} + \kappa \frac{\partial \rho}{\partial t} = \lambda^2 \frac{\delta \mathcal{F}}{\delta \rho}, \quad (64)$$

where  $\kappa$  and  $\lambda$  are constants. At early times, molecular positions relax fast, consistently with elasticity theory, whereas at late times diffusive dynamics dominates the kinetics of phase transformations, the diffusion of vacancies, the motion of grain boundaries, and dislocation climb. In other words, elastic interactions mediated by wave modes have been incorporated, which travel on time scales that are orders of magnitude slower than the molecular vibrations yet considerably faster than the diffusive time scale. A similar EOM has been proposed for the VPFC model, whose free-energy functional forces the order parameter to be non-negative. The resulting approach dictates the number of atoms and describes the motion of each of them. Solution of the respective EOM might be viewed as essentially performing MD simulations on diffusive time scales [56]. A similar approach has been adapted to study the dynamics of monatomic and binary glasses, however, using MPFT-type free-energy functionals and temperature-dependent noise terms [47].

**3.1.1.3. The Euler-Lagrange equation.** The ELE can be used to study equilibrium features including the mapping of the phase diagram [28] as well as the evaluation of the free energy of the liquid-solid interface [28] and of the nucleation barrier [35]. We note that noise may influence the phase diagram and other physical properties. Therefore, the results from the ELE and EOM are expected to converge for  $\zeta \rightarrow 0$ . We also call attention to the fact that so far as the equilibrium results (obtained by ELE) are concerned, the SH and 1M-PFC models are equivalent.

Once the free-energy functional is defined for the specific PFC model, its extremes

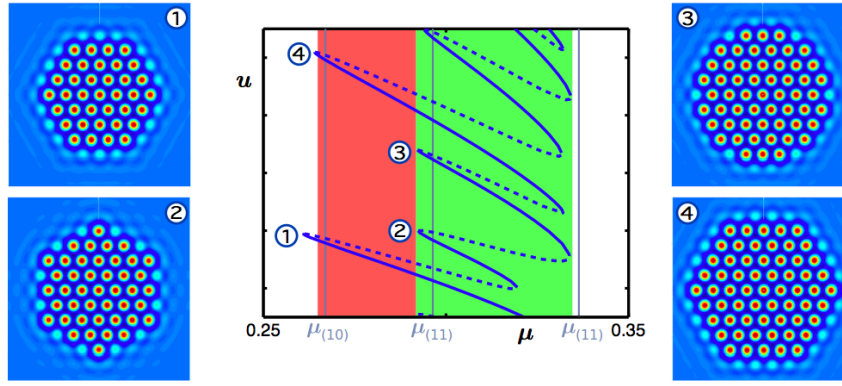


Figure 8. Multiplicity of localized hexagonal cluster solutions for the dynamic SH equation  $\partial u/\partial t = -(1 + \nabla_{\mathbf{r}}^2)^2 u - \mu u + \nu u^2 - u^3$  with  $\nu = 1.6$ . The central panel displays a part of the bifurcation diagram for localized hexagonal patches (for details see reference [142]). The solid and dashed lines stand for the stable and unstable solutions, respectively. The vertical lines in grey correspond to the fold limits of planar (10) and (11) hexagon pulses. The red and green regions indicate where temporal self-completion does or does not occur, respectively. Panels 1-4 show colour plots of the hexagon patches at the inner and outer left folds. A different parametrisation is used here:  $\mu = -\epsilon + 3\psi_0^2$ . (Reproduced with permission from D. J. B. Lloyd, B. Sandstede, D. Avitabile, and A. R. Champneys, *Localized hexagon patterns of the planar Swift-Hohenberg equation*, *SIAM J. Appl. Dyn. Syst.* 7 (2008), 1049-1100, no. 3, DOI: 10.1137/070707622 © 2008 by The Society for Industrial and Applied Mathematics.)

can be found by solving the respective ELE, which reads as

$$\frac{\delta \tilde{\mathcal{F}}}{\delta \tilde{\psi}} = \frac{\delta \tilde{\mathcal{F}}}{\delta \tilde{\psi}} \Big|_{\tilde{\psi}_0}, \quad (65)$$

where  $\tilde{\psi}_0$  is the reduced particle number density of the unperturbed initial liquid, while a no-flux boundary condition is prescribed at the boundaries of the simulation window ( $\mathbf{n} \cdot \nabla_{\mathbf{r}} \tilde{\psi} = 0$  and  $(\mathbf{n} \cdot \nabla_{\mathbf{r}}) \nabla_{\mathbf{r}}^2 \tilde{\psi} = 0$ , where  $\mathbf{n}$  is the normal vector of the boundary). For example, inserting the 1M-PFC free energy and rearranging the terms, one arrives at

$$(-\epsilon + (1 + \nabla_{\mathbf{r}}^2)^2)(\tilde{\psi} - \tilde{\psi}_0) + p(\tilde{\psi}^2 - \tilde{\psi}_0^2) - (\tilde{\psi}^3 - \tilde{\psi}_0^3) = 0. \quad (66)$$

Equation (66) together with the boundary conditions represents a fourth-order boundary value problem (BVP).

*Multiplicity of solutions of the ELE.* It is worth noting that in the case of the PFC/SH-type models, a multiplicity of solutions can usually be found for the same BVP, defined by the boundary conditions and the ELE. This feature of the stationary solutions has been recently addressed in some detail in 2D for the SH [142] and in 1D for the VPFC [143] models. (Figure 8 illustrates this phenomenon via showing the bifurcation diagram for compact hexagonal clusters in the SH model [142].)

### 3.1.2. Binary PFC models

#### 3.1.2.1. The free energy.

*Binary Swift-Hohenberg form.* The earliest binary extension of the PFC model has been proposed in the seminal paper of Elder et al. [12] obtained by adding an interaction term with coefficient  $A$  to the free energy of two mixed single-component

SH free energies. Working with particle densities  $\tilde{\psi}_1$  and  $\tilde{\psi}_2$ , this yields the free energy

$$\begin{aligned} \tilde{\mathcal{F}} = \int d\mathbf{r} & \left( \frac{\tilde{\psi}_1}{2} \left( -\beta_1 + (k_1^2 + \nabla_{\mathbf{r}}^2)^2 \right) \tilde{\psi}_1 + \frac{\tilde{\psi}_1^4}{4} \right. \\ & \left. + \frac{\tilde{\psi}_2}{2} \left( -\beta_2 + (k_2^2 + \nabla_{\mathbf{r}}^2)^2 \right) \tilde{\psi}_2 + \frac{\tilde{\psi}_2^4}{4} + A\tilde{\psi}_1\tilde{\psi}_2 \right). \end{aligned} \quad (67)$$

Here, the physical properties (bulk moduli, lattice constants, etc.) of the individual species are controlled by the parameters with subscripts 1 and 2, respectively, and by the average values of the particle densities  $\tilde{\psi}_1$  and  $\tilde{\psi}_2$ . It has been shown that the model can be used for studying structural phase transitions [12].

*DFT-based binary PFC model.* The most extensively used binary generalisation of the 1M-PFC model has been derived starting from a binary perturbative DFT, where the free energy is Taylor expanded relative to the liquid state denoted by  $\bar{\rho}_A$  and  $\bar{\rho}_B$ , respectively, up to second order in the density differences  $\Delta\rho_A = \rho_A - \bar{\rho}_A$  and  $\Delta\rho_B = \rho_B - \bar{\rho}_B$  (up to two-particle correlations) [26]:

$$\begin{aligned} \frac{\mathcal{F}}{k_B T} = \int d\mathbf{r} & \left( \rho_A \ln \left( \frac{\rho_A}{\bar{\rho}_A} \right) - \Delta\rho_A + \rho_B \ln \left( \frac{\rho_B}{\bar{\rho}_B} \right) - \Delta\rho_B \right) \\ & - \frac{1}{2} \int d\mathbf{r}_1 \int d\mathbf{r}_2 \left( \Delta\rho_A(\mathbf{r}_1) c_{AA}^{(2)}(\mathbf{r}_1, \mathbf{r}_2) \Delta\rho_A(\mathbf{r}_2) \right. \\ & \quad + \Delta\rho_B(\mathbf{r}_1) c_{BB}^{(2)}(\mathbf{r}_1, \mathbf{r}_2) \Delta\rho_B(\mathbf{r}_2) \\ & \quad \left. + 2 \Delta\rho_A(\mathbf{r}_1) c_{AB}^{(2)}(\mathbf{r}_1, \mathbf{r}_2) \Delta\rho_B(\mathbf{r}_2) \right). \end{aligned} \quad (68)$$

It is assumed here that all two-point correlation functions are isotropic, i.e.,  $c_{ij}^{(2)}(\mathbf{r}_1, \mathbf{r}_2) = c_{ij}^{(2)}(|\mathbf{r}_1 - \mathbf{r}_2|)$ . Taylor expanding the direct correlation functions in Fourier space up to fourth order, one obtains  $c_{ij}^{(2)}(|\mathbf{r}_1 - \mathbf{r}_2|) = (c_{ij,0}^{(2)} - c_{ij,2}^{(2)} \nabla_{\mathbf{r}_2}^2 + c_{ij,4}^{(2)} \nabla_{\mathbf{r}_2}^4) \delta(\mathbf{r}_1 - \mathbf{r}_2)$  in real space [26]. The partial direct correlation functions  $c_{ij}^{(2)}$  can be related to the measured or computed partial structure factors.

Following Elder et al. [26], the reduced partial particle density differences are defined as  $\psi_A = (\rho_A - \bar{\rho}_A)/\rho_0$  and  $\psi_B = (\rho_B - \bar{\rho}_B)/\rho_0$ , where  $\rho_0 = \bar{\rho}_A + \bar{\rho}_B$ . They have introduced then the new variables  $\psi = \psi_A + \psi_B$  and  $\hat{\psi} = (\psi_B - \psi_A) + (\bar{\rho}_B - \bar{\rho}_A)/\rho_0$ , obtaining fields whose amplitude expansion yields field amplitudes resembling order parameters associated with structural and composition changes in the conventional PF models. Expanding the free energy around  $\hat{\psi} = 0$  and  $\psi = 0$  one obtains

$$\begin{aligned} \frac{\mathcal{F}}{\rho_{\text{ref}} k_B T} = \int d\mathbf{r} & \left( \frac{\psi}{2} (B_1 + B_s (2R^2 \nabla_{\mathbf{r}}^2 + R^4 \nabla_{\mathbf{r}}^4)) \psi + s \frac{\psi^3}{3} + v \frac{\psi^4}{4} \right. \\ & \left. + \gamma \hat{\psi} + w \frac{\hat{\psi}^2}{2} + u \frac{\hat{\psi}^4}{4} + \frac{L^2}{2} (\nabla_{\mathbf{r}} \hat{\psi})^2 + \dots \right). \end{aligned} \quad (69)$$

This model has been used for studying a broad range of phase transitions, including the formation of solutal dendrites, eutectic structures [26, 28], and the Kirkendall effect [55].

*Binary PFC model for surface alloying.* A somewhat different formulation of the binary model has been proposed to model compositional patterning in monolayer aggregates of binary metallic systems by Muralidharan and Haataja [48]:

$$\mathcal{F} = \int d\mathbf{r} \left( \frac{\rho}{2} (\beta(c) + (k_c^2 + \nabla_{\mathbf{r}}^2)^2) \rho + \frac{\rho^4}{4} + V(c) \rho + f_0 \left( \frac{w_0^2}{2} (\nabla_{\mathbf{r}} c)^2 - \theta_c \frac{c^2}{2} + \frac{\theta}{2} ((1+c) \ln(1+c) + (1-c) \ln(1-c)) \right) \right). \quad (70)$$

In this construction, the values  $c = \pm 1$  of the concentration field stand for different atomic species,  $V(c)$  is the atom specific substrate-film interaction,  $k_c$  incorporates the bulk lattice constant of different species,  $f_0$  governs the relative strength of the elastic and chemical energies, while  $\theta_c$  is the critical temperature,  $\theta$  the scaled absolute temperature, and  $w_0$  tunes the chemical contribution to the interface energy between different species. Starting from this free-energy functional, Muralidharan and Haataja have shown, that their PFC model incorporates competing misfit dislocations and alloying in a quantitative way, and then employed the model for investigating the misfit- and line tension dependence of the domain size [48].

### 3.1.2.2. The equations of motion.

*Dimensionless binary form in Swift-Hohenberg fashion.* The same type of overdamped conservative dynamics has been assumed for the two types of atoms [12]:

$$\frac{\partial \tilde{\psi}_1}{\partial t} = M_1 \nabla_{\mathbf{r}}^2 \frac{\delta \tilde{\mathcal{F}}}{\delta \tilde{\psi}_1} + \zeta_1 \quad \text{and} \quad \frac{\partial \tilde{\psi}_2}{\partial t} = M_2 \nabla_{\mathbf{r}}^2 \frac{\delta \tilde{\mathcal{F}}}{\delta \tilde{\psi}_2} + \zeta_2. \quad (71)$$

Here,  $M_i$  and  $\zeta_i$  are the mobility and the noise term applying to species  $i \in \{1, 2\}$ .

*DFT-based binary PFC model.* In this widely used formulation of the binary 1M-PFC model, it is assumed that the same mobility  $M$  applies for the two species A and B (corresponding to substitutional diffusion) decoupling the dynamics of the fields  $\psi$  and  $\hat{\psi}$ . Assuming, furthermore, a constant effective mobility  $M_e = 2M/\rho^2$  and conserved dynamics, the equations of motions for the two fields have the form [26]

$$\frac{\partial \psi}{\partial t} = M_e \nabla_{\mathbf{r}}^2 \frac{\delta \mathcal{F}}{\delta \psi} \quad \text{and} \quad \frac{\partial \hat{\psi}}{\partial t} = M_e \nabla_{\mathbf{r}}^2 \frac{\delta \mathcal{F}}{\delta \hat{\psi}}. \quad (72)$$

In general, the coefficients  $B_1$ ,  $B_s$ , and  $R$  in equation (69) depend on  $\hat{\psi}$ . A Taylor expansion of  $B_1(\hat{\psi})$ ,  $B_s(\hat{\psi})$ , and  $R(\hat{\psi})$  in terms of  $\hat{\psi}$  yields new coefficients  $B_i^1$ ,  $B_i^s$ , and  $R_i$  with  $i = 0, 1, 2, \dots$  that are independent of  $\hat{\psi}$ . Retaining only the coefficients  $B_0^1$ ,  $B_2^1$ ,  $B_0^s$ ,  $R_0$ , and  $R_1$ , and inserting the free energy (69) into equations (72), one

obtains

$$\begin{aligned} \frac{\partial \psi}{\partial t} = & M_e \nabla_{\mathbf{r}}^2 \left( \psi (B_0^1 + B_2^1 \hat{\psi}^2) + s\psi^2 + v\psi^3 \right. \\ & + \frac{B_0^s}{2} \left( 2(R_0 + R_1 \hat{\psi})^2 \nabla_{\mathbf{r}}^2 + (R_0 + R_1 \hat{\psi}^4) \nabla_{\mathbf{r}}^4 \right) \psi \\ & \left. + \frac{B_0^s}{2} \left( 2\nabla_{\mathbf{r}}^2 (\psi (R_0 + R_1 \hat{\psi})^2) + \nabla_{\mathbf{r}}^4 (\psi (R_0 + R_1 \hat{\psi})^4) \right) \right), \end{aligned} \quad (73)$$

$$\begin{aligned} \frac{\partial \hat{\psi}}{\partial t} = & M_e \nabla_{\mathbf{r}}^2 \left( B_2^1 \hat{\psi} \psi^2 + \gamma + w\hat{\psi} + u\hat{\psi}^3 - L^2 \nabla_{\mathbf{r}}^2 \hat{\psi} \right. \\ & \left. + 2B_0^s \psi \left( (R_0 + R_1 \hat{\psi}) R_1 \nabla_{\mathbf{r}}^2 + (R_0 + R_1 \hat{\psi})^3 R_1 \nabla_{\mathbf{r}}^4 \right) \psi \right). \end{aligned} \quad (74)$$

**3.1.2.3. The Euler-Lagrange equations.** Since the derivation of the ELE is straightforward for all the binary PFC models, we illustrate it for the most frequently used version deduced from the binary Ramakrishnan-Yussouff-type classical perturbative DFT. The extremum of the grand potential functional requires that its first functional derivatives are zero, i. e.,

$$\frac{\delta \mathcal{F}}{\delta \psi} = \left. \frac{\delta \mathcal{F}}{\delta \psi} \right|_{\psi_0, \hat{\psi}_0} \quad \text{and} \quad \frac{\delta \mathcal{F}}{\delta \hat{\psi}} = \left. \frac{\delta \mathcal{F}}{\delta \hat{\psi}} \right|_{\psi_0, \hat{\psi}_0}, \quad (75)$$

where  $\psi_0$  and  $\hat{\psi}_0$  are the total and relative particle densities for the homogeneous initial state. Inserting equation (69) into equation (75), one obtains after rearranging

$$\begin{aligned} & \left( B_1 \hat{\psi} + B_s R \hat{\psi}^2 (2\nabla_{\mathbf{r}}^2 + R \hat{\psi}^2 \nabla_{\mathbf{r}}^4) + \frac{B_s}{2} (2\nabla_{\mathbf{r}}^2 (R^2) + \nabla_{\mathbf{r}}^4 (R^4)) \right) (\psi - \psi_0) \\ & = -s(\psi^2 - \psi_0^2) - v(\psi^3 - \psi_0^3), \end{aligned} \quad (76)$$

$$\begin{aligned} & L^2 \nabla_{\mathbf{r}}^2 \hat{\psi} - \frac{\partial B_1}{\partial \hat{\psi}} (\hat{\psi} \psi^2 - \hat{\psi}_0 \psi_0^2) - 2B_s R \frac{\partial R}{\partial \hat{\psi}} \psi (\nabla_{\mathbf{r}}^2 + R^2 \nabla_{\mathbf{r}}^4) \psi \\ & = w(\hat{\psi} - \hat{\psi}_0) + u(\hat{\psi}^3 - \hat{\psi}_0^3), \end{aligned} \quad (77)$$

where  $R = R_0 + R_1 \hat{\psi}$ . These equations are to be solved assuming no-flux boundary conditions at the border of the simulation box for both fields [ $\mathbf{n} \cdot \nabla_{\mathbf{r}} \psi = 0$ ,  $(\mathbf{n} \cdot \nabla_{\mathbf{r}}) \nabla_{\mathbf{r}}^2 \psi = 0$ ,  $\mathbf{n} \cdot \nabla_{\mathbf{r}} \hat{\psi} = 0$ , and  $(\mathbf{n} \cdot \nabla_{\mathbf{r}}) \nabla_{\mathbf{r}}^2 \hat{\psi} = 0$ ].

### 3.1.3. PFC models for liquid crystals

Another level of complexity is to consider interactions between particles, that are not any longer spherically symmetric. The simplest case are *oriented* particles, i. e., particles with a fixed orientation along a given direction where the interaction  $U_2(\mathbf{r}_1 - \mathbf{r}_2)$  is not any longer radially symmetric [as assumed in equation (36)]. The derivation described in section 2.3 was straightforwardly extended towards this case leading to a microscopic justification of the APFC model (59) proposed in section 3.1.1.1. Clearly, the resulting crystal lattices are anisotropic, which leads also to an anisotropic crystal growth. Much more complicated, however, is the case of *orientable* particles, which can adjust their orientation and form liquid crystalline mesophases.

Therefore, we now address orientable anisotropic particles, that possess orientational degrees of freedom. In order to keep the effort manageable, the particles are assumed to be uniaxial, i. e., they are rotationally symmetric around an internal axis. Consequently, their orientations are described by unit vectors  $\hat{\mathbf{u}}_i$  with  $i \in \{1, \dots, N\}$  along their internal symmetry axes. Most of the statistical quantities can suitably be generalized towards orientational degrees of freedom by including also the orientational configuration space on top of the translational configurational space.

**3.1.3.1. Statics.** For orientable particles, the one-particle density is now defined via

$$\rho(\mathbf{r}, \hat{\mathbf{u}}) = \left\langle \sum_{i=1}^N \delta(\mathbf{r} - \mathbf{r}_i) \delta(\hat{\mathbf{u}} - \hat{\mathbf{u}}_i) \right\rangle \quad (78)$$

and contains also the probability distribution of the orientations as expressed by the dependence on the orientational unit vector  $\hat{\mathbf{u}}$ . Its full configurational mean is given by the mean particle number density

$$\rho_0 = \frac{1}{4\pi V} \int d\mathbf{r} \int d\hat{\mathbf{u}} \rho(\mathbf{r}, \hat{\mathbf{u}}) = \frac{N}{V}, \quad (79)$$

where the orientational integral denotes integration over the two-dimensional unit sphere  $S_2$ . Now the external potential is  $U_1(\mathbf{r}, \hat{\mathbf{u}})$  and couples also to the particle orientation. In general, also the pair-interaction potential  $U_2(\mathbf{r}_1 - \mathbf{r}_2, \hat{\mathbf{u}}_1, \hat{\mathbf{u}}_2)$  has an orientational dependence. The corresponding equilibrium Helmholtz free-energy functional  $\mathcal{F}[\rho(\mathbf{r}, \hat{\mathbf{u}})]$  can be split as usual in three contributions

$$\mathcal{F}[\rho(\mathbf{r}, \hat{\mathbf{u}})] = \mathcal{F}_{\text{id}}[\rho(\mathbf{r}, \hat{\mathbf{u}})] + \mathcal{F}_{\text{exc}}[\rho(\mathbf{r}, \hat{\mathbf{u}})] + \mathcal{F}_{\text{ext}}[\rho(\mathbf{r}, \hat{\mathbf{u}})] \quad (80)$$

namely the ideal rotator-gas free-energy contribution

$$\mathcal{F}_{\text{id}}[\rho(\mathbf{r}, \hat{\mathbf{u}})] = k_{\text{B}}T \int d\mathbf{r} \int d\hat{\mathbf{u}} \rho(\mathbf{r}, \hat{\mathbf{u}}) (\ln(\Lambda^3 \rho(\mathbf{r}, \hat{\mathbf{u}})) - 1), \quad (81)$$

the nontrivial excess free-energy functional  $\mathcal{F}_{\text{exc}}[\rho(\mathbf{r}, \hat{\mathbf{u}})]$ , and the external free-energy contribution (see section 2.1)

$$\mathcal{F}_{\text{ext}}[\rho(\mathbf{r}, \hat{\mathbf{u}})] = \int d\mathbf{r} \int d\hat{\mathbf{u}} \rho(\mathbf{r}, \hat{\mathbf{u}}) U_1(\mathbf{r}, \hat{\mathbf{u}}). \quad (82)$$

Analogously to equation (8), a functional Taylor expansion

$$\mathcal{F}_{\text{exc}}[\rho(\mathbf{r}, \hat{\mathbf{u}})] = \mathcal{F}_{\text{exc}}^{(0)}(\rho_{\text{ref}}) + k_{\text{B}}T \sum_{n=1}^{\infty} \frac{1}{n!} \mathcal{F}_{\text{exc}}^{(n)}[\rho(\mathbf{r}, \hat{\mathbf{u}})] \quad (83)$$

with the  $n$ th-order contributions

$$\mathcal{F}_{\text{exc}}^{(n)}[\rho(\mathbf{r}, \hat{\mathbf{u}})] = - \int d\mathbf{r}_1 \cdots \int d\mathbf{r}_n \int d\hat{\mathbf{u}}_1 \cdots \int d\hat{\mathbf{u}}_n c^{(n)}(\mathbf{r}^{\mathbf{n}}, \hat{\mathbf{u}}^{\mathbf{n}}) \prod_{i=1}^n \Delta \rho(\mathbf{r}_i, \hat{\mathbf{u}}_i), \quad (84)$$

the  $n$ -particle direct correlation function  $c^{(n)}(\mathbf{r}^n, \hat{\mathbf{u}}^n)$ , and the abbreviations

$$\mathbf{r}^n = (\mathbf{r}_1, \dots, \mathbf{r}_n), \quad \hat{\mathbf{u}}^n = (\hat{\mathbf{u}}_1, \dots, \hat{\mathbf{u}}_n) \quad (85)$$

are used. Again, the constant zeroth-order contribution of the functional Taylor expansion (83) is irrelevant and the first-order contribution vanishes. In the Ramakrishnan-Yussouff approximation, the functional Taylor expansion is truncated at second order.

In order to derive PFC-type models for liquid crystals, one can follow the same strategy as for spherical systems: first, the full density field  $\rho(\mathbf{r}, \hat{\mathbf{u}})$  is parametrized by small and slowly varying space-dependent multi-component order-parameter fields. An insertion into the density functional together with a perturbative and gradient expansion yields a local PFC-type free energy. Then several coupling terms of the order-parameter components arise, whose prefactors are given by moments of the generalized direct fluid correlation functions. Still, the gradient expansion is more tedious, since the orientational space has a more complicated topology. For stability reasons, one has to assume that the coefficients of the highest-order terms in the gradients and order-parameter fields in the PFC model are positive in the full free-energy functional. If this appears not to be the case for a certain system, it is necessary to take further terms of the respective order-parameter field up to the first stabilizing order into account.

**3.1.3.2. Two spatial dimensions.** We now consider first the case of two spatial dimensions both for the translational and orientational degrees of freedom. Here, the topology of orientations is simpler than in three spatial dimensions. Obviously, all previous expressions can be changed towards two dimensions by replacing the volume  $V$  by an area  $A$ , by changing the unit sphere  $S_2$  into the unit circle  $S_1$ , and by replacing  $\Lambda^3$  by  $\Lambda^2$  in equation (81). The orientational vector  $\hat{\mathbf{u}}(\varphi) = (\cos(\varphi), \sin(\varphi))$  can be parametrized by a single polar angle  $\varphi \in [0, 2\pi)$ .

*Derivation of the PFC free-energy functional.* First we chose as order-parameter fields the *reduced translational density*, the *polarization*, and the *nematic tensor* field. The reduced translational density is defined via

$$\psi(\mathbf{r}) = \frac{1}{2\pi\rho_{\text{ref}}} \int d\hat{\mathbf{u}} (\rho(\mathbf{r}, \hat{\mathbf{u}}) - \rho_{\text{ref}}), \quad (86)$$

while the polarization is

$$\mathbf{P}(\mathbf{r}) = \frac{1}{\pi\rho_{\text{ref}}} \int d\hat{\mathbf{u}} \rho(\mathbf{r}, \hat{\mathbf{u}}) \hat{\mathbf{u}} \quad (87)$$

and describes the local averaged dipolar orientation of the particles. Finally, the symmetric and traceless nematic tensor with the components

$$Q_{ij}(\mathbf{r}) = \frac{2}{\pi\rho_{\text{ref}}} \int d\hat{\mathbf{u}} \rho(\mathbf{r}, \hat{\mathbf{u}}) \left( u_i u_j - \frac{1}{2} \delta_{ij} \right) \quad (88)$$

describes quadrupolar ordering of the particles. Equivalently, one could decompose the polarization  $\mathbf{P}(\mathbf{r}) = P(\mathbf{r})\hat{\mathbf{p}}(\mathbf{r})$  into its modulus  $P(\mathbf{r})$  and the local normalised dipolar orientation  $\hat{\mathbf{p}}(\mathbf{r})$  and use the two order parameters  $P(\mathbf{r})$  and  $\hat{\mathbf{p}}(\mathbf{r})$  instead

of  $\mathbf{P}(\mathbf{r})$ . Similarly, the nematic tensor can be expressed by [144, 145]

$$Q_{ij}(\mathbf{r}) = S(\mathbf{r}) \left( n_i(\mathbf{r})n_j(\mathbf{r}) - \frac{1}{2}\delta_{ij} \right) \quad (89)$$

through the *nematic order parameter*  $S(\mathbf{r})$ , which measures the local degree of quadrupolar orientational order [146], and the *nematic director*  $\hat{\mathbf{n}}(\mathbf{r}) = (n_1(\mathbf{r}), n_2(\mathbf{r}))$ . Notice that  $\hat{\mathbf{n}}(\mathbf{r})$  and  $\hat{\mathbf{p}}(\mathbf{r})$  do not necessarily coincide.

One may expand the total density in terms of its orientational anisotropy as

$$\rho(\mathbf{r}, \hat{\mathbf{u}}) = \rho_{\text{ref}}(1 + \psi(\mathbf{r}) + P_i(\mathbf{r})u_i + u_i Q_{ij}(\mathbf{r})u_j). \quad (90)$$

Inserting the parametrisation (90) into equation (81), performing a Taylor expansion of the integrand up to fourth order in the order-parameter fields, which guarantees stability of the solutions, and carrying out the angular integration yields to the approximation

$$\mathcal{F}_{\text{id}}[\psi, P_i, Q_{ij}] = F_{\text{id}} + \pi\rho_{\text{ref}} k_B T \int d\mathbf{r} f_{\text{id}}(\mathbf{r}) \quad (91)$$

with the local scaled ideal rotator-gas free-energy density

$$\begin{aligned} f_{\text{id}} = & \frac{\psi}{4}(8 - 2P_i^2 + 2P_i Q_{ij} P_j - Q_{ij}^2) + \frac{\psi^2}{4}(4 + 2P_i^2 + Q_{ij}^2) - \frac{\psi^3}{3} + \frac{\psi^4}{6} \\ & + \frac{P_i^2}{8}(4 + Q_{kl}^2) - \frac{P_i Q_{ij} P_j}{4} + \frac{P_i^2 P_j^2}{16} + \frac{Q_{ij}^2}{4} + \frac{Q_{ij}^2 Q_{kl}^2}{64}, \end{aligned} \quad (92)$$

where  $F_{\text{id}} = 2\pi\rho_{\text{ref}} k_B T A (\ln(\Lambda^2 \rho_{\text{ref}}) - 1)$  is an irrelevant constant.

If the functional Taylor expansion (83) for the excess free energy is truncated at fourth order, an insertion of the parametrisation (90) into the functional (84) and a gradient expansion yield [147]

$$\mathcal{F}_{\text{exc}}^{(n)}[\psi, P_i, Q_{ij}] = - \int d\mathbf{r} f_{\text{exc}}^{(n)}(\mathbf{r}) \quad (93)$$

with

$$\begin{aligned} f_{\text{exc}}^{(2)} = & A_1 \psi^2 + A_2 (\partial_i \psi)^2 + A_3 (\partial_k^2 \psi)^2 + B_1 (\partial_i \psi) P_i + B_2 P_i (\partial_j Q_{ij}) + B_3 (\partial_i \psi) (\partial_j Q_{ij}) \\ & + C_1 P_i^2 + C_2 P_i (\partial_k^2 P_i) + C_3 (\partial_i P_i)^2 + D_1 Q_{ij}^2 + D_2 (\partial_j Q_{ij})^2, \end{aligned} \quad (94)$$

$$\begin{aligned} f_{\text{exc}}^{(3)} = & E_1 \psi^3 + E_2 \psi P_i^2 + E_3 \psi Q_{ij}^2 + E_4 P_i Q_{ij} P_j + F_1 \psi^2 (\partial_i P_i) + F_2 \psi P_i (\partial_j Q_{ij}) \\ & + F_3 (\partial_i \psi) Q_{ij} P_j + F_4 P_i^2 (\partial_j P_j) + F_5 (\partial_i P_i) Q_{kl}^2 + F_6 P_i Q_{ki} (\partial_j Q_{kj}), \end{aligned} \quad (95)$$

$$\begin{aligned} f_{\text{exc}}^{(4)} = & G_1 \psi^4 + G_2 \psi^2 P_i^2 + G_3 \psi^2 Q_{ij}^2 + G_4 \psi P_i Q_{ij} P_j + G_5 P_i^2 Q_{kl}^2 + G_6 P_i^2 P_j^2 \\ & + G_7 Q_{ij}^2 Q_{kl}^2. \end{aligned} \quad (96)$$

Obviously, this creates a much more sophisticated series of coupling terms between gradients of the different order-parameter fields. They are all allowed by symmetry. There are altogether 28 coupling coefficients  $A_i, B_i, C_i, D_i, E_i, F_i, G_i$ , which can in



Table 2. Relevant special cases that are contained in the polar PFC model for two spatial dimensions.  $n_{\max}$  is the order of the functional Taylor expansion (83). If  $n_{\max}$  is not specified, it can be arbitrary (arb.).

$\psi$	$P_i$	$Q_{ij}$	$n_{\max}$	Associated model
0	0	<i>const.</i>	<i>arb.</i>	Landau expansion in $Q_{ij}(\mathbf{r})$
0	0	$Q_{ij}(\mathbf{r})$	2	Landau-de Gennes free energy for uniaxial nematics [145]
0	0	$Q_{ij}(\mathbf{r})$	<i>arb.</i>	Gradient expansion in $Q_{ij}(\mathbf{r})$
0	<i>const.</i>	0	<i>arb.</i>	Landau expansion in $P_i(\mathbf{r})$
0	$P_i(\mathbf{r})$	0	<i>arb.</i>	Gradient expansion in $P_i(\mathbf{r})$
<i>const.</i>	$P_i(\mathbf{r})$	$Q_{ij}(\mathbf{r})$	4	Constant-density approximation
$\psi(\mathbf{r})$	0	0	2	PFC model of Elder et al. [26]
$\psi(\mathbf{r})$	0	$Q_{ij}(\mathbf{r})$	2	PFC model of Löwen [58]
$\psi(\mathbf{r})$	$P_i(\mathbf{r})$	$Q_{ij}(\mathbf{r})$	4	Full free-energy functional

principle all be expressed as moments over the microscopic fluid direct correlation functions. These explicit expressions are summarized in appendix A.1.

The general result for the two-dimensional PFC free energy constituted by equations (94)-(96) contains several special cases, known from the literature, which we now discuss in more detail.

These special cases follow from the full free-energy functional either by choosing some of the order-parameter fields as zero or as a constant different from zero and by taking into account the contributions of the functional Taylor expansion (83) only up to a certain order  $n_{\max} \in \{2, 3, 4\}$ . Table 2 gives an overview about the most relevant special cases.

The two most simple special cases are obtained for either a constant polarization  $P_i(\mathbf{r})$  or a constant nematic tensor  $Q_{ij}(\mathbf{r})$  with an arbitrary choice for  $n_{\max}$ , when all remaining order-parameter fields are assumed to be zero. These special cases are known to be Landau expansions in  $P_i(\mathbf{r})$  and  $Q_{ij}(\mathbf{r})$ , respectively. If the polarization  $P_i(\mathbf{r})$  is not constant, but space-dependent, and the other order-parameter fields vanish, then the functional can be called a gradient expansion in the polarization. Analogously, a gradient expansion in the nematic tensor  $Q_{ij}(\mathbf{r})$  is obtained, if it is space-dependent and all other order-parameter fields vanish. If additionally  $n_{\max} = 2$  is chosen, this gradient expansion becomes the Landau-de Gennes free energy for inhomogeneous uniaxial nematics [145]. When only  $\psi(\mathbf{r})$  is constant and the other order-parameter fields are space-dependent, we recover the case of an incompressible system. If all anisotropies are neglected, we recover with  $n_{\max} = 2$  the original PFC model of Elder et al. [26]. The liquid crystalline PFC model of Löwen [58] is obtained, if in addition to the translational density also the nematic tensor is space-dependent and if it is parametrized according to equation (89). In the polar PFC model for two spatial dimensions, one can also consider the case of a space-dependent translational density  $\psi(\mathbf{r})$ , a space-dependent polarization  $P_i(\mathbf{r})$ , and a vanishing nematic tensor, that corresponds to a ferroelectric phase without orientational order, but such a phase was never observed in experiments up to the present day. Therefore, this case is not included in Tab. 2.

*Equilibrium bulk phase diagram.* While there are two independent parameters for the original PFC model (see equation (1) and figure 9), the number of coupling parameters explodes for the general liquid crystalline PFC model as proposed in equations (94)-(96) to 27 coupling coefficients. One of them can be incorporated into a length scale such that 26 coefficients remain. Therefore, a numerical exploration of the equilibrium phase diagram requires a much higher effort. Maybe not too surprising, such calculations are sparse and it was only until recently that the

phase diagram was calculated for the apolar PFC model [58], where  $\mathbf{P}(\mathbf{r}) = \mathbf{0}$ , which contains only 5 independent parameters [60]. We summarize and outline the basic findings of reference [60] in section 3.2.2.

**3.1.3.3. Three spatial dimensions.** We now discuss the three-dimensional ( $d = 3$ ) PFC model for liquid crystals. In spherical coordinates, the three-dimensional orientation vector is

$$\hat{\mathbf{u}}(\theta, \phi) = (\sin(\theta) \cos(\phi), \sin(\theta) \sin(\phi), \cos(\theta)) \quad (97)$$

with the polar angle  $\theta \in [0, \pi]$  and the azimuthal angle  $\phi \in [0, 2\pi)$ . We consider here only the apolar case, where the polarization vanishes:  $\mathbf{P}(\mathbf{r}) = \mathbf{0}$ . There exists indeed a zoo of realizations of apolar particles both in the molecular and in the colloidal regime. For suitable interactions see references [148–156].

Following similar ideas as outlined in section 3.1.3.2 for two dimensions, we define as the corresponding order parameters the reduced translational density

$$\psi(\mathbf{r}) = \frac{1}{4\pi\rho_{\text{ref}}} \int d\hat{\mathbf{u}} (\rho(\mathbf{r}, \hat{\mathbf{u}}) - \rho_{\text{ref}}) \quad (98)$$

and the  $3 \times 3$ -dimensional symmetric and traceless nematic tensor

$$Q_{ij}(\mathbf{r}) = \frac{15}{8\pi\rho_{\text{ref}}} \int d\hat{\mathbf{u}} \rho(\mathbf{r}, \hat{\mathbf{u}}) \left( u_i u_j - \frac{1}{3} \delta_{ij} \right). \quad (99)$$

Again, the nematic tensor can be expressed by the nematic order-parameter field  $S(\mathbf{r})$  and the nematic director  $\hat{\mathbf{n}}(\mathbf{r}) = (n_1(\mathbf{r}), n_2(\mathbf{r}), n_3(\mathbf{r}))$ , that is here the only unit vector that denotes a preferred direction in the liquid crystalline system. In the three-dimensional case, the decomposition of the nematic tensor is given by [144, 145]

$$Q_{ij}(\mathbf{r}) = S(\mathbf{r}) \left( \frac{3}{2} n_i(\mathbf{r}) n_j(\mathbf{r}) - \frac{1}{2} \delta_{ij} \right). \quad (100)$$

Notice that the nematic order-parameter field  $S(\mathbf{r})$  is the biggest eigenvalue of the nematic tensor  $Q_{ij}(\mathbf{r})$  and the nematic director  $\hat{\mathbf{n}}(\mathbf{r})$  is the corresponding eigenvector. Accordingly, with the order-parameter fields  $\psi(\mathbf{r})$  and  $Q_{ij}(\mathbf{r})$ , the one-particle density is approximated by

$$\rho(\mathbf{r}, \hat{\mathbf{u}}) = \rho_{\text{ref}} (1 + \psi(\mathbf{r}) + u_i Q_{ij}(\mathbf{r}) u_j). \quad (101)$$

As before, the Helmholtz free-energy functional has to be approximated by a Taylor expansion around the homogeneous reference system and by a gradient expansion [59]. The ideal rotator-gas free-energy functional is approximated by

$$\mathcal{F}_{\text{id}}[\psi, Q_{ij}] = F_{\text{id}} + \pi\rho_{\text{ref}} k_B T \int d\mathbf{r} f_{\text{id}}(\mathbf{r}) \quad (102)$$

Table 3. Relevant special cases, that are contained in the apolar PFC model for three spatial dimensions.

$\psi$	$Q_{ij}$	Associated model
0	<i>const.</i>	Landau expansion in $Q_{ij}(\mathbf{r})$
0	$Q_{ij}(\mathbf{r})$	Landau-de Gennes free energy for uniaxial nematics [145]
$\psi(\mathbf{r})$	0	PFC model of Elder et al. [26]
$\psi(\mathbf{r})$	$Q_{ij}(\mathbf{r})$	Full free-energy functional

with the local scaled ideal rotator-gas free-energy density

$$f_{\text{id}} = 4\psi \left( 1 - \frac{\text{tr}(\mathbf{Q}^2)}{15} + \frac{8 \text{tr}(\mathbf{Q}^3)}{315} \right) + 2\psi^2 \left( 1 + \frac{2 \text{tr}(\mathbf{Q}^2)}{15} \right) - \frac{2\psi^3}{3} + \frac{\psi^4}{3} + \frac{4 \text{tr}(\mathbf{Q}^2)}{15} - \frac{16 \text{tr}(\mathbf{Q}^3)}{315} + \frac{8 \text{tr}(\mathbf{Q}^4)}{315}. \quad (103)$$

Here,  $\text{tr}(\cdot)$  denotes the trace operator and  $F_{\text{id}} = 4\pi\rho_{\text{ref}}V k_{\text{B}}T(\ln(\Lambda^3\rho_{\text{ref}}) - 1)$  an irrelevant constant. For the excess free-energy functional, the Ramakrishnan-Yussouff approximation (11) is used together with equation (101) involving the direct correlation function  $c^{(2)}(\mathbf{r}_1 - \mathbf{r}_2, \hat{\mathbf{u}}_1, \hat{\mathbf{u}}_2)$ . Respecting all symmetries, one finally obtains the following approximation for the excess free-energy functional

$$\mathcal{F}_{\text{exc}}^{(2)}[\psi, Q_{ij}] = - \int d\mathbf{r} f_{\text{exc}}^{(2)}(\mathbf{r}) \quad (104)$$

with the local scaled excess free-energy density

$$f_{\text{exc}}^{(2)} = A_1\psi^2 + A_2(\partial_i\psi)^2 + A_3(\partial_k^2\psi)^2 + B_1Q_{ij}^2 + B_2(\partial_i\psi)(\partial_jQ_{ij}) + \tilde{K}_1(\partial_jQ_{ij})^2 + \tilde{K}_2Q_{ij}(\partial_k^2Q_{ij}). \quad (105)$$

The seven coupling coefficients  $A_1, A_2, A_3, B_1, B_2, \tilde{K}_1, \tilde{K}_2$  can be expressed as generalized moments of the microscopic correlation function  $c^{(2)}(\mathbf{r}_1 - \mathbf{r}_2, \hat{\mathbf{u}}_1, \hat{\mathbf{u}}_2)$ . The full expressions are summarized in appendix A.2. We remark that  $\tilde{K}_1$  and  $\tilde{K}_2$  correspond to the traditional Frank constants appearing in Frank's elastic energy [145, 157].

Special cases of the free-energy density are summarized in Tab. 3. As for the PFC model for two spatial dimensions, one obtains a Landau expansion in the nematic tensor  $Q_{ij}(\mathbf{r})$ , if the translational density  $\psi(\mathbf{r})$  is zero and the nematic tensor is constant so that all gradients vanish. When only  $\psi(\mathbf{r})$  is constant and  $Q_{ij}(\mathbf{r})$  is space-dependent, the Landau-de Gennes free energy for inhomogeneous uniaxial nematics [145] is recovered again. Clearly, the original PFC model of Elder et al. [26] for isotropic particles in three spatial dimensions can be obtained from the full free-energy functional by choosing  $Q_{ij}(\mathbf{r}) = 0$ . Finally, we note that the full functional was recently numerically evaluated for several situations by Yabunaka and Araki in reference [158].

**3.1.3.4. Dynamics.** Dynamical density functional theory (DDFT) can now be used to derive the dynamics of the PFC models for liquid crystals. DDFT is well justified for Brownian anisotropic particles (as, for example, colloidal rods or platelets). The basic derivation is similar to that performed for spherical particles in section 2.3.2, but in practice it is much more tedious. The basic derivation is performed in three steps. At first, the order-parameter fields, that have been

chosen for the statics, are assumed to be time-dependent and the time-dependent one-particle density  $\rho(\mathbf{r}, \hat{\mathbf{u}}, t)$  is approximated in terms of these time-dependent order-parameter fields. Secondly, the chain rule for functional differentiation is used to express the functional derivative  $\delta\mathcal{F}/\delta\rho$  of the Helmholtz free-energy functional  $\mathcal{F}$  in terms of the functional derivatives of the free-energy functional with respect to the chosen order-parameter fields. Finally, the time-dependent parametrisation for the one-particle density and the time-dependent expression for the functional derivative  $\delta\mathcal{F}/\delta\rho$  are inserted into the DDFT equation and a set of in general coupled dynamic equations for the single order-parameter fields is obtained by an orthogonal projection of the DDFT equation with respect to the orientation  $\hat{\mathbf{u}}$ .

We first consider the case of two spatial dimensions ( $d = 2$ ). The time-dependent noise-averaged one-particle number density is now

$$\rho(\mathbf{r}, \hat{\mathbf{u}}, t) = \left\langle \sum_{i=1}^N \delta(\mathbf{r} - \mathbf{r}_i(t)) \delta(\hat{\mathbf{u}} - \hat{\mathbf{u}}_i(t)) \right\rangle \quad (106)$$

and its order-parameter parametrisation is

$$\rho(\mathbf{r}, \hat{\mathbf{u}}, t) = \rho_{\text{ref}} (1 + \psi(\mathbf{r}, t) + P_i(\mathbf{r}, t) u_i + u_i Q_{ij}(\mathbf{r}, t) u_j). \quad (107)$$

The DDFT equation for orientational degrees of freedom in two spatial dimensions (without a hydrodynamic translational-rotational coupling) reads [99]

$$\begin{aligned} \dot{\rho}(\mathbf{r}, \hat{\mathbf{u}}, t) = \nabla_{\mathbf{r}} \cdot \left( \frac{D_{\text{T}}(\hat{\mathbf{u}})}{k_{\text{B}}T} \rho(\mathbf{r}, \hat{\mathbf{u}}, t) \nabla_{\mathbf{r}} \frac{\delta\mathcal{F}(T, [\rho])}{\delta\rho(\mathbf{r}, \hat{\mathbf{u}}, t)} \right) \\ + \frac{D_{\text{R}}}{k_{\text{B}}T} \partial_{\varphi} \left( \rho(\mathbf{r}, \hat{\mathbf{u}}, t) \partial_{\varphi} \frac{\delta\mathcal{F}(T, [\rho])}{\delta\rho(\mathbf{r}, \hat{\mathbf{u}}, t)} \right) \end{aligned} \quad (108)$$

with the translational short-time diffusion tensor

$$D_{\text{T}}(\hat{\mathbf{u}}) = D_{\parallel} \hat{\mathbf{u}} \otimes \hat{\mathbf{u}} + D_{\perp} (\mathbf{1} - \hat{\mathbf{u}} \otimes \hat{\mathbf{u}}). \quad (109)$$

Here,  $D_{\parallel}$  and  $D_{\perp}$  are the translational diffusion coefficients for translation parallel and perpendicular to the orientation  $\hat{\mathbf{u}} = (\cos(\phi), \sin(\phi))$ , respectively, and the symbol  $\mathbf{1}$  denotes the  $2 \times 2$ -dimensional unit matrix. The two terms on the right-hand-side of this DDFT equation correspond to pure translation and pure rotation, respectively.

The constant-mobility approximation (CMA) is now

$$\dot{\rho}(\mathbf{r}, \hat{\mathbf{u}}, t) = \rho_{\text{ref}} \nabla_{\mathbf{r}} \cdot \left( \frac{D_{\text{T}}(\hat{\mathbf{u}})}{k_{\text{B}}T} \nabla_{\mathbf{r}} \frac{\delta\mathcal{F}(T, [\rho])}{\delta\rho(\mathbf{r}, \hat{\mathbf{u}}, t)} \right) + \rho_{\text{ref}} \frac{D_{\text{R}}}{k_{\text{B}}T} \partial_{\varphi}^2 \frac{\delta\mathcal{F}(T, [\rho])}{\delta\rho(\mathbf{r}, \hat{\mathbf{u}}, t)}. \quad (110)$$

Within the CMA, this yields for the dynamics of the order-parameter fields

$$\dot{\psi} + \partial_i J_i^{\psi} = 0, \quad \dot{P}_i + \Phi_i^P = 0, \quad \dot{Q}_{ij} + \Phi_{ij}^Q = 0 \quad (111)$$

with the currents and quasi-currents

$$J_i^{\psi} = -2\alpha_1 \partial_i \frac{\delta\mathcal{F}}{\delta\psi} - 2\alpha_3 \partial_j \frac{\delta\mathcal{F}}{\delta Q_{ij}}, \quad (112)$$

$$\Phi_i^P = -2\alpha_2 \partial_k^2 \frac{\delta \mathcal{F}}{\delta P_i} - 4\alpha_3 \partial_i \partial_j \frac{\delta \mathcal{F}}{\delta P_j} + 2\alpha_4 \frac{\delta \mathcal{F}}{\delta P_i}, \quad (113)$$

$$\Phi_{ij}^Q = -4\alpha_1 \partial_k^2 \frac{\delta \mathcal{F}}{\delta Q_{ij}} - 2\alpha_3 \left( 2\partial_i \partial_j \frac{\delta \mathcal{F}}{\delta \psi} - \delta_{ij} \partial_k^2 \frac{\delta \mathcal{F}}{\delta \psi} \right) + 8\alpha_4 \frac{\delta \mathcal{F}}{\delta Q_{ij}}. \quad (114)$$

The coefficients  $\alpha_i$  in equations (112)-(114) are defined as

$$\alpha_1 = \frac{D_{\parallel} + D_{\perp}}{8\lambda}, \quad \alpha_2 = \frac{D_{\parallel} + 3D_{\perp}}{8\lambda}, \quad \alpha_3 = \frac{D_{\parallel} - D_{\perp}}{8\lambda}, \quad \alpha_4 = \frac{D_{\text{R}}}{2\lambda}. \quad (115)$$

Notice that  $D_{\parallel} \geq D_{\perp}$  holds for all types of uniaxial particles, if the vector  $\hat{\mathbf{u}}$  for the orientation of the axis of symmetry is chosen properly.

Finally, we remark that in three dimensions ( $d = 3$ ) the dynamics is much more involved but can in principle be derived along similar lines from DDFT [103]. Recently, the CMA dynamics was considered in reference [158]. A main result of this reference is shown in section 5.3.

### 3.1.4. Numerical methods

**3.1.4.1. The equation of motion.** The commonly used explicit time-stepping with a finite-difference (FD) scheme has been routinely applied for solving the EOM of the PFC models [159]. However, owing to the high order differential operators appearing in the EOM of the PFC models (up to 12th order), explicit time-stepping suffers from severe constraints. Energy stable large time-step implicit FD methods have been developed for the PFC [160] and MPFC [161] equations that lead to large sets of sparse algebraic equations. The resultant algebraic equations can be solved using nonlinear multigrid methods [162]. As elegant alternative, pseudo-spectral methods can be used that combine unconditionally stable time marching while resulting in algebraic equations of the diagonal form [163]. Furthermore, pseudo-spectral methods offer exponential convergence with the spatial resolution as opposed to the polynomial convergence rate of the FD schemes. This means that with smaller spatial resolution one obtains results comparable to those obtained with high spatial resolution in the real space methods. Using operator splitting techniques the domain of the spectral methods has been extended to a wide range of problems, including PDEs with variable coefficients [164]. A detailed study on the application of this method to the PFC models shows that the respective schemes can be parallelised easily and efficiently [164], yielding up to  $10^5$  times faster computations, when compared to FD schemes. Adaptive time stepping [163] may further accelerate the computations. Other numerical methods (e. g., stable semi-implicit finite element discretisation combined with adaptive time stepping [165]) have also been used for PFC models, however, further investigations are needed to assess their numerical accuracy.

**3.1.4.2. The Euler-Lagrange equation and other saddle point finding methods.** In recent works (see, e. g., references [28, 35]) the ELE has been solved using a semi-spectral successive approximation scheme combined with the operator-splitting technique [166]. A different approach termed the fixed length simplified string method has been proposed to find the minimum energy path and the nucleation barrier in reference [32].

### 3.1.5. Coarse-graining the PFC models

Soon after the appearance of the 1M-PFC model, attempts have been made to use this atomistic approach as a basis for deriving phase-field-type coarse-grained models using the amplitude equation method. This extension to the 1M-PFC formalism, when combined with the adaptive grid, has the potential to enable simulations of mesoscopic phenomena ( $\mu\text{m} \rightarrow \text{mm}$ ) that are resolved down to the atomic scale, still incorporating all the respective physics.

**3.1.5.1. Amplitude equations based on renormalisation group theory.** Goldenfeld, Athreya, and Dantzig [131] have developed a computationally efficient approach to polycrystalline solidification, based on the 1M-PFC model. The nanoscale particle density distribution is reconstructed from its slowly varying amplitude and phase, obtained by solving the rotationally covariant equations of motion derived from renormalisation group theory. They have shown in two dimensions that the microscopic density distributions from their amplitude and phase equations show a very close match to the 1M-PFC result. In later works Athreya and co-workers [19, 20] have combined this approach with adaptive mesh algorithms, leading to a substantial acceleration of the numerical code. (Possible ways of using the renormalisation group methods have been discussed in references [20, 167].)

**3.1.5.2. Phenomenological amplitude equations.** Approximate treatments based on the amplitude expansion of the free energy of the 1M-PFC models (i. e., expressing  $\mathcal{F}$  in terms of the Fourier amplitude of the dominant density waves) have been developed. They have been used for various purposes, such as determining the anisotropy of liquid-solid interfacial free energies [41, 132], the Asaro-Tiller-Grinfeld (ATG) morphological instability of a stressed crystal surface, polycrystalline growth from the melt, grain-boundary energies over a wide range of misorientation, and grain-boundary motion coupled to shear deformation [54, 168]. Yeon et al. [169] have used an amplitude-equation approach to model the evolution of a two-phase system that has been validated by investigating the Gibbs-Thomson effect in two spatial dimensions. Elder, Huang, and Provatas [31] have proposed amplitude representations for the binary PFC model in the cases of triangular lattice (2D) and bcc and fcc (3D) structures. The respective equations of motion have been related to those of the original PF theory of binary freezing and elasticity, providing explicit connection between the PF and PFC approaches. The abilities of the phenomenological amplitude models have been demonstrated for eutectic solidification, solute migration at grain boundaries, and for the formation of quantum dots on nanomembranes [31].

## 3.2. Phase diagrams the PFC models realize

The different versions and extensions of the PFC model, reviewed in section 3.1, lead to different phase diagrams, which in turn depend on the dimensionality of the system.

### 3.2.1. Phase diagram of single-component and binary systems

The phase diagrams of the 1M-PFC model [12] in two and three spatial dimensions are shown in figure 9. In two spatial dimensions, a single crystalline phase (the triangular phase) appears that coexists with the liquid and a striped phase [12]. Remarkably, phase diagrams of comparable structure have been predicted for

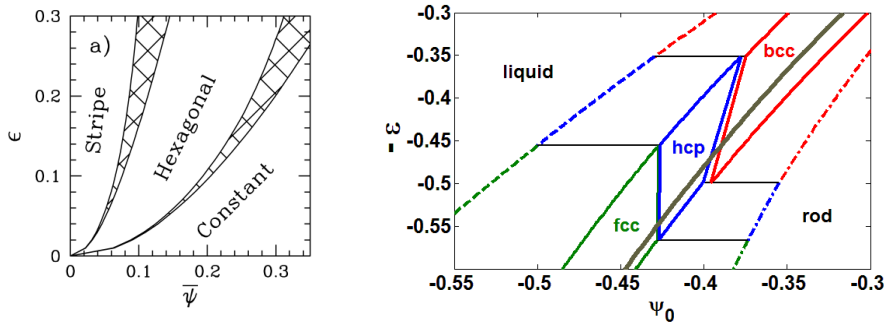


Figure 9. (a) Single-mode approximation to the phase diagram of the 1M-PFC model in two spatial dimensions with  $\epsilon \equiv \beta$  and the average reduced particle density  $\bar{\psi}$ . (Reproduced with permission from K. R. Elder, M. Katakowski, M. Haataja, and M. Grant, *Modeling elasticity in crystal growth*, Phys. Rev. Lett. 88 (2002), 245701, no. 24, DOI: 10.1103/PhysRevLett.88.245701 © 2002 by the American Physical Society.) (b) Section of the 3D phase diagram of the 1M-PFC model evaluated by the Euler-Lagrange method described in reference [28] with  $\epsilon \equiv \beta$  and the average reduced particle density  $\psi_0$ . Notice the stability domains of the bcc, hcp, and fcc phases. The homogeneous liquid is unstable right of the heavy grey line emerging from linear stability analysis [28]. (Reproduced from G. I. Tóth, G. Tegze, T. Pusztai, G. Tóth, and L. Gránásy, *Polymorphism, crystal nucleation and growth in the phase-field crystal model in 2D and 3D*, J. Phys.: Condens. Matter 22 (2010), 364101, no. 36, DOI: 10.1088/0953-8984/22/36/364101 © 2010 by Institute of Physics Publishing.)

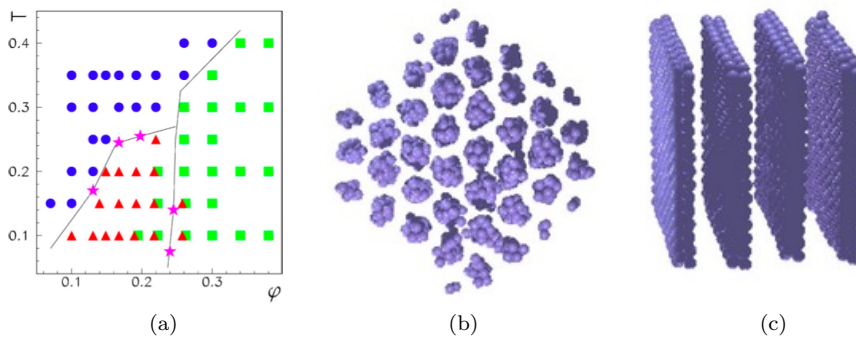


Figure 10. (a) Temperature-particle density phase diagram from MD simulations with a DLVO-type potential. Circles represent the disordered phase, triangles the columnar phase, and squares the lamellar phase. Stars stand for points, where the free energies of two phases cross. Solid lines are a guide for the eyes. Snapshots of the (b) triangular rod and (c) lamellar phases. (Reproduced with permission from A. de Candia, E. Del Gado, A. Fierro, N. Sator, M. Tarzia, and A. Coniglio, *Columnar and lamellar phases in attractive colloidal systems*, Phys. Rev. E 74 (2006), 010403R, no. 1, DOI: 10.1103/PhysRevE.74.010403 © 2006 by the American Physical Society.)

weakly charged colloids with competing interactions [170]. In three spatial dimensions, as implied earlier by EOM studies [42], and confirmed by full thermodynamic optimization [171] and an equivalent method based on solving the ELE [28], stability domains exist for the homogeneous fluid, bcc, fcc, and hcp structures, besides the 3D version of the respective 2D structures: the rod and the lamellar structures. Interestingly, the rod and lamellar structures, and a phase diagram resembling to the 1M-PFC phase diagram appear in MD simulations for a Derjaguin-Landau-Verwey-Overbeek (DLVO) type potential [172] (see figure 10), characteristic to charged colloidal systems. The 1M-PFC model prefers the formation of the bcc phase near the critical point.

In contrast, the 2M-PFC model of Wu et al. [132] designed to realize fcc crystallization, suppresses the bcc phase [see figure 11(a)]. The 2M-PFC extension incorporates the 1M-PFC model as a limiting case. Interpolation between 1M-PFC and the full fcc limit ( $R_1 = 0$ ), in terms of the parameter  $R_1$  leads to the appearance of a bcc stability domain in the vicinity of the critical point [see figure 11(b)]. ( $R_1$  is the ratio of the Fourier amplitudes for the density waves having the second and first

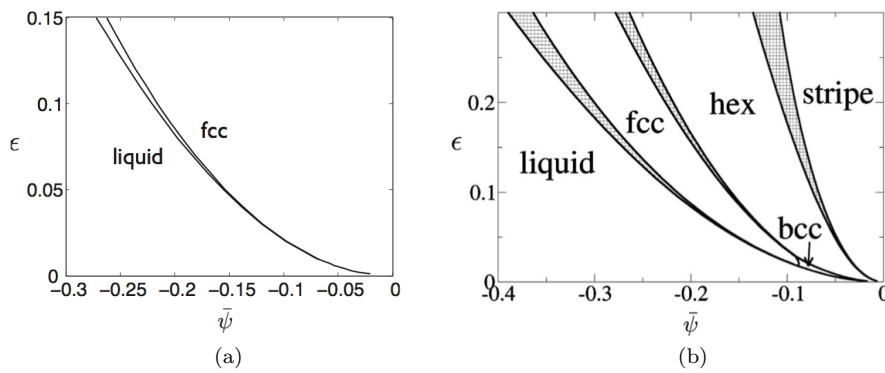


Figure 11. (a) Single-mode approximations to the phase diagram of the 2M-PFC model in 3D for  $R_1 = 0$ . (b) The same for  $R_1 = 0.05$ . Notice the small bcc stability domain near the critical point. (Reproduced with permission from K.-A. Wu, A. Adland, and A. Karma, *Phase-field-crystal model for fcc ordering*, Phys. Rev. E 81 (2010), 061601, no. 6, DOI: 10.1103/PhysRevE.81.061601 © 2010 by the American Physical Society.)

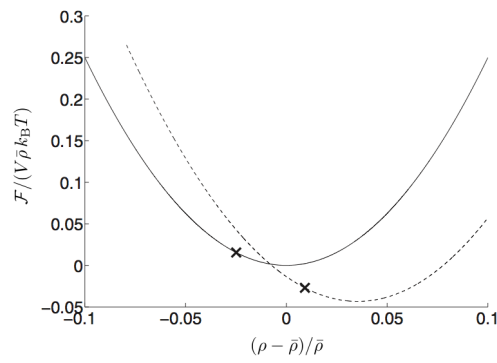


Figure 12. Free-energy density for the liquid (solid) and bcc (dashed) Fe as a function of reduced particle density in the EOF-PFC model. Crosses denote the equilibrium points obtained by the common tangent method. (Reproduced with permission from A. Jaatinen, C. V. Achim, K. R. Elder, and T. Ala-Nissila, *Thermodynamics of bcc metals in phase-field-crystal models*, Phys. Rev. E 80 (2009), 031602, no. 3, DOI: 10.1103/PhysRevE.80.031602 © 2009 by the American Physical Society.)

neighbour RLVs as wave vector.) Whether here the appearance of the bcc phase is accompanied with the appearance of a hcp stability domain, as in the 1M-PFC limit, requires further investigation.

The applicability of the EOF-PFC model has been demonstrated for Fe [133]. The free energy vs. particle density curves for the solid and liquid phases, which were used to determine the equilibrium conditions at the melting point, are shown in figure 12. No phase diagram has been published for this model. It appears that much like the original, the 1M-PFC model, it prefers bcc freezing.

An attempt to control the preferred crystal structure relies on manipulating the two-particle direct correlation function so that its peaks prefer the desired structural correlations [135]. The type of phase diagram accessible for this method and the respective free-energy curves for coexistence between the bcc and fcc structures are displayed in figure 13(a). Starting from the observation that the nonlinearities can stabilize the square lattice [173] so that it coexists with the triangular phase [174], Wu, Plapp, and Voorhees [136] have proposed a method based on nonlinear resonance for constructing PFC models that prefer the desired crystal structure, as they indeed demonstrated for the square lattice in two spatial dimensions: the relative free energies of possible competing structures are compared in figure 13(b).

Elder et al. [26] have obtained eutectic phase diagrams within the binary generalisation of the 1M-PFC model in two spatial dimensions both numerically and



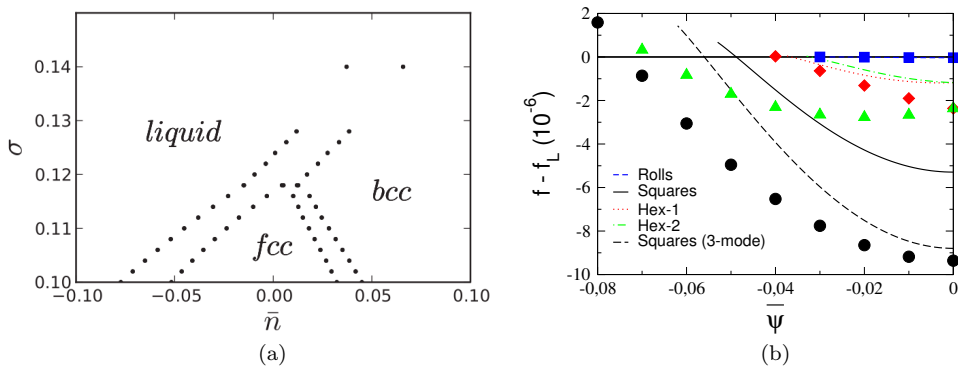


Figure 13. (a) Phase diagram in the effective temperature  $\sigma$ -mean density  $\bar{n}$ -plane for a system whose direct correlation function was manipulated so that peritectic coexistence between the fcc and bcc structures is realized. (Reproduced with permission from M. Greenwood, J. Rottler, and N. Provatas, *Phase-field-crystal methodology for modeling of structural transformations*, Phys. Rev. E 83 (2011), 031601, no. 3, DOI: 10.1103/PhysRevE.83.031601 © 2011 by the American Physical Society.) (b) Free-energy density  $f$  vs. average reduced particle density  $\bar{\psi}$  when controlling the crystal structure via nonlinear resonance.  $f_L$  denotes the free-energy density of the liquid. The analytical solutions are plotted as lines, while the numerical simulation results for rolls, squares, hex-1, and hex-2 are plotted as squares, circles, diamonds, and triangles, respectively. (Reproduced with permission from K.-A. Wu, M. Plapp, and P. W. Voorhees, *Controlling crystal symmetries in phase-field crystal models*, J. Phys.: Condens. Matter 22 (2010), 364102, no. 36, DOI: 10.1088/0953-8984/22/36/364102 © 2010 by Institute of Physics Publishing.)

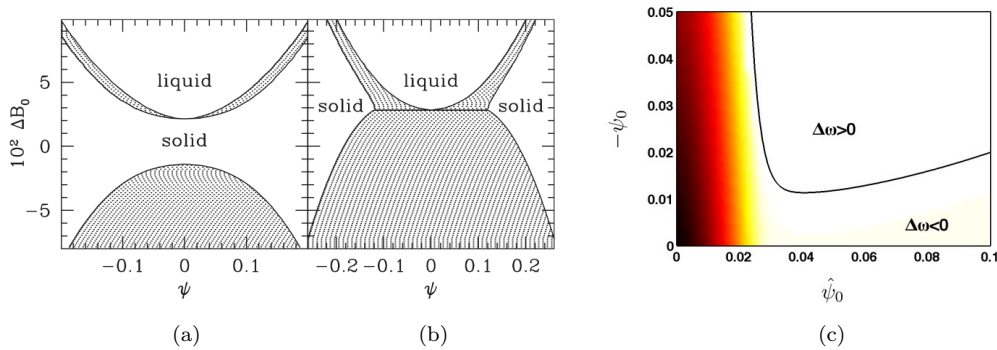


Figure 14. (a), (b) Reduced temperature  $\Delta B_0$  vs. reduced particle density difference  $\psi$  phase diagrams for the two-dimensional triangular system in the amplitude equation formalism. The filled regions correspond to regions of phase coexistence. (Reproduced with permission from K. R. Elder, Z.-F. Huang, and N. Provatas, *Amplitude expansion of the binary phase-field-crystal model*, Phys. Rev. E 81 (2010), 011602, no. 1, DOI: 10.1103/PhysRevE.81.011602 © 2010 by the American Physical Society.) (c) Colour map for the thermodynamic driving force of eutectic solidification ( $\Delta\omega$  is the grand potential density difference relative to the liquid) for the binary 1M-PFC model in 3D [28], as a function of the chemical composition  $\hat{\psi}_0$  and density  $\psi_0$ . Notice that solidification is expected in the region, where  $\Delta\omega < 0$ . (Reproduced from G. I. Tóth, G. Tegze, T. Pusztai, G. Tóth, and L. Gránásy, *Polymorphism, crystal nucleation and growth in the phase-field crystal model in 2D and 3D*, J. Phys.: Condens. Matter 22 (2010), 364101, no. 36, DOI: 10.1088/0953-8984/22/36/364101 © 2010 by Institute of Physics Publishing.)

by using the single-mode approximation. Comparable phase diagrams [see figures 14(a) and 14(b)] have been reported for triangular phases in two spatial dimensions, and for the bcc and fcc phases in 3D, by the phenomenological amplitude equation method [31]. The 3D extension of the binary 1M-PFC model has been investigated by Tóth et al. [28]. The map of the thermodynamic driving force for solidification as a function of composition and density of the initial liquid is shown in figure 14(c). 3D eutectic solidification to bcc phases of different lattice constants has indeed been observed in the domain of the largest driving force.

An essential question is how to extend the PFC framework to accommodate the physical properties of real alloys of different crystalline structures. A two-phase binary extension of the EOF-PFC model based on the 1M-PFC and 2M-PFC concepts might be worth exploring.

The VPFC extension of the 1M-PFC model leads to a restructured phase diagram

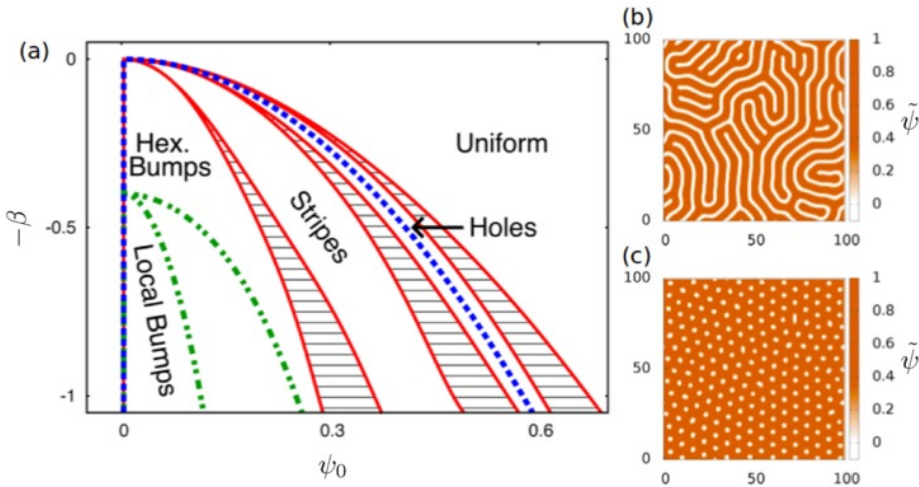


Figure 15. Phase diagram for the VPCF model in two spatial dimensions [see equation (58)] (a) for  $k_0 = 1$  [143]. The red solid lines denote coexistence curves, the green dash-dotted lines envelope the region, where localized and hexagonally ordered density peaks (bumps) coexist, whereas the blue dashed line indicates the linear stability limit of the spatially uniform phase. Snapshots of simulations for (b) stripes and (c) hexagonally ordered holes are also shown. These simulations have been performed for:  $k_0 = 1$ ,  $\beta = 0.9$ ,  $h = 1500$ ,  $M = 1$  (the mobility in the EOM) and (b)  $\psi_0 = 0.4$  and (c)  $\psi_0 = 0.53$ . (Reproduced from M. J. Robbins, A. J. Archer, U. Thiele, and E. Knobloch, *Modelling fluids and crystals using a two-component modified phase field crystal model*, Phys. Rev. E 85 (2012), 061408, no. 6, DOI: 10.1103/PhysRevE.85.061408 © 2012 by the American Physical Society.)

(see figure 15) [143], whose central region contains stability domains for the 2D hexagonal crystal and localized density peaks (“bumps”) that represent individual particles.

### 3.2.2. Phase diagram of two-dimensional liquid crystals

For liquid crystalline systems, there are much more candidates for possible bulk phases. Therefore the topology of the bulk phase diagram is getting more complex. Recently, bulk phase diagrams were computed by using the two-dimensional apolar PFC model of Löwen [58]. After an appropriate scaling in energy and length, this model reads as

$$\begin{aligned} \mathcal{F}[\psi, Q_{ij}] = \int d\mathbf{r} \left( -\frac{\psi^3}{3} + \frac{\psi^4}{6} + (\psi - 1)\frac{\psi Q_{ij}^2}{4} + \frac{Q_{ij}^2 Q_{kl}^2}{64} \right. \\ \left. + A_1 \psi^2 + A_2 \psi (\partial_k^2 + \partial_l^2) \psi \right. \\ \left. + B_3 (\partial_i \psi) (\partial_j Q_{ij}) + D_1 Q_{ij}^2 + D_2 (\partial_j Q_{ij})^2 \right). \end{aligned} \quad (116)$$

Some trends of the phase diagram can directly be read of equation (116). Since the parameter  $D_1$  controls the contribution of the nematic tensor  $Q_{ij}(\mathbf{r})$  and therefore also of the nematic order parameter  $S(\mathbf{r})$ , the nematic phase can be expected to be stable for large negative values of  $D_1$ . In the opposite case, if  $D_1$  is large and positive, the term  $D_1 Q_{ij}^2(\mathbf{r}) + Q_{ij}^2(\mathbf{r}) Q_{kl}^2(\mathbf{r})/64$  dominates the free energy and only phases with  $Q_{ij}(\mathbf{r}) \propto S(\mathbf{r}) = 0$  can be stable. Crystalline phases with a non-vanishing nematic order can therefore only appear in a region around  $D_1 = 0$ . From previous work it is known that the difference  $A_1 - A_2/4$  has a big influence on the translational density field  $\psi(\mathbf{r})$  [26, 60]. If the parameter  $A_1$  is large and positive, variations of the translational density field enlarge the free energy. Similarly, gradients of the translational density field enlarge the free energy for large and negative values of  $A_2$ . Therefore, phases without any density modulations, i. e.,

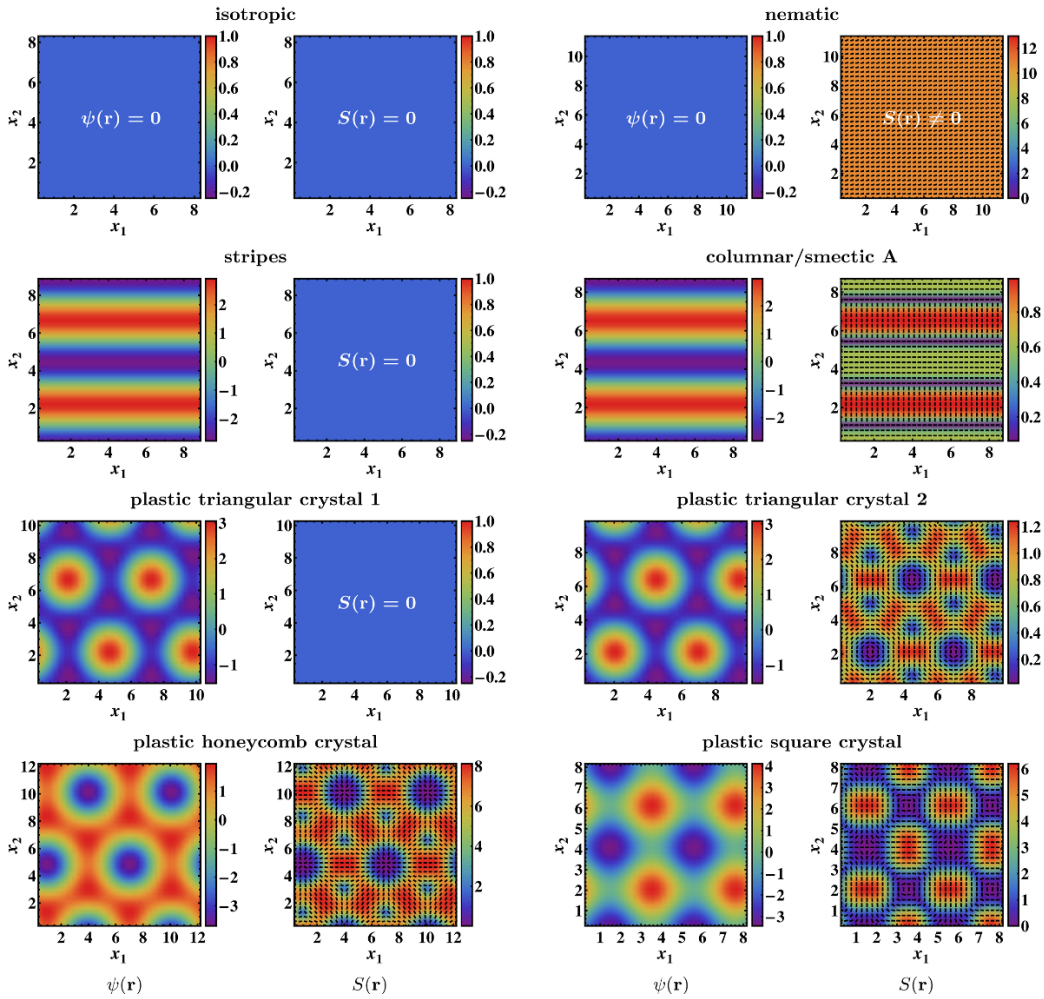


Figure 16. Stable liquid crystalline phases. The contour plots show the order-parameter fields  $\psi(\mathbf{r})$  and  $S(\mathbf{r})$  in the  $x_1$ - $x_2$ -plane for the isotropic and nematic phases, the stripe phase and columnar/smectic A phase, two plastic triangular crystals with different orientational ordering, and a plastic honeycomb crystal as well as a plastic square crystal. The black lines in the plots of the second and fourth column represent the director field  $\hat{\mathbf{n}}(\mathbf{r})$ . In the plots with  $S(\mathbf{r}) = 0$ , the director field is not shown because it is not defined. The parameters are  $A_2 = 14$ ,  $D_2 = 8$ , and  $B_3 = 0$  for the stripe phase and the plastic triangular crystal 1 and  $A_2 = 14$ ,  $D_2 = 0.8$ , and  $B_3 = -4$  for all other phases. (Reproduced from C. V. Achim, R. Wittkowski, and H. Löwen, *Stability of liquid crystalline phases in the phase-field-crystal model*, Phys. Rev. E 83 (2011), 061712, no. 6, DOI: 10.1103/PhysRevE.83.061712 © 2011 by the American Physical Society.)

the isotropic and the nematic phase, are preferred for positive values of the difference  $A_1 - A_2/4$ , while all other phases with a periodic translational density field are preferred for negative values of this difference. Furthermore, there is a symmetry concerning the reversal of the sign of the parameter  $B_3$  in the free-energy functional. From equation (116) follows directly, that the free-energy functional is invariant under a simultaneous change of the signs of the parameter  $B_3$  and the nematic order-parameter field  $S(\mathbf{r})$ . Due to this symmetry,  $B_3 \geq 0$  can be assumed without loss of generality.

Depending on the coupling parameters, a wealth of different stable liquid crystalline phases was found (see figure 16). They include an *isotropic* phase, which has no translational and no orientational ordering ( $\psi(\mathbf{r}) = 0$  and  $S(\mathbf{r}) = 0$ ), a *nematic* phase with pure orientational ordering ( $\psi(\mathbf{r}) = 0$  and  $S(\mathbf{r}) > 0$ ), a *columnar* phase (or equivalently a *smectic A* phase), where the translational density and the orientation show a one-dimensional undulation, and various *plastic crystals*. In the columnar/smectic A phase the system has positional ordering in one direction, while it is isotropic perpendicular to this direction. The nematic order-parameter

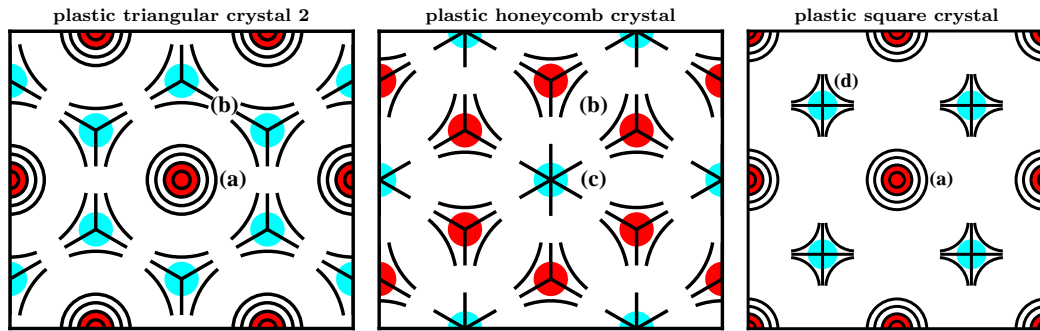


Figure 17. Topological defects in three different plastic liquid crystals in the  $x_1$ - $x_2$ -plane (schematic). The defects coincide with the maxima (red discs) and minima (cyan discs) of the translational density field  $\psi(\mathbf{r})$ . The symbols in the plots represent the following defects: (a) vortices with the *topological winding number*  $m = 1$ , (b) disclinations with  $m = -1/2$ , (c) sources/sinks with  $m = 1$ , and (d) hyperbolic points with  $m = -1$ . (Reproduced from C. V. Achim, R. Wittkowski, and H. Löwen, *Stability of liquid crystalline phases in the phase-field-crystal model*, Phys. Rev. E 83 (2011), 061712, no. 6, DOI: 10.1103/PhysRevE.83.061712 © 2011 by the American Physical Society.)

field  $S(\mathbf{r})$  for this phase has a similar profile to the reduced translational density field  $\psi(\mathbf{r})$  with maxima of these two fields at the same positions. Near the maxima of the translational density  $\psi(\mathbf{r})$ , the director field  $\hat{\mathbf{n}}(\mathbf{r})$  is preferentially parallel to the gradient  $\partial_i \psi(\mathbf{r})$ , while it is perpendicular to  $\partial_i \psi(\mathbf{r})$  around the minima of  $\psi(\mathbf{r})$ . A similar flipping of the orientational field from perpendicular to parallel to the stripe direction was identified as transverse intralayer order in the three-dimensional smectic A phase of hard spherocylinders [109].

Plastic crystals are two-dimensional modulations of the translational density and have no global (averaged) orientational direction. Interestingly, depending on the coupling-parameter combinations, three different types of plastic crystals are stable including two-dimensional triangular, square, and honeycomb lattices for the translational ordering. The orientational field of plastic crystals is schematically shown in figure 17. It exhibits an interesting defect structure in the orientation. There are defects at the density peaks and in the interstitial places of the lattice. The defect structure has not yet been explored so far outside the PFC-world. It can be confirmed in microscopic computer simulations [175] or in real-space experiments [176–178].

In a two-dimensional slice of the coupling parameter space, the phase diagram is shown in figure 18. Apart from the isotropic phase with  $\psi(\mathbf{r}) = 0$  and  $S(\mathbf{r}) = 0$ , which appears for  $A_1 > A_2/4$  and  $D_1 > 0$ , for negative and large  $D_1$  a nematic phase is stable. A rich topology occurs around  $D_1 = 0$  including columnar phases and three different plastic crystals. However, one should bear in mind that the phase transitions shown in figure 18 were assumed to be isochoric, i. e., without any density jump. While this is in general a good approximation for liquid crystalline phase transitions, it is not true in general. Independent of the particular value of the parameter  $B_3$ , the phase transition between the isotropic and the nematic phase is continuous, while all other phase transitions are discontinuous.

In conclusion, rich phase diagrams with novel liquid crystalline phases were found in the apolar PFC model. This gives confidence that in a further step interfaces between coexisting phases and the dynamics can be explored on the basis of the PFC approach. It would open the way of PFC models to enter into the rich world of liquid crystals.

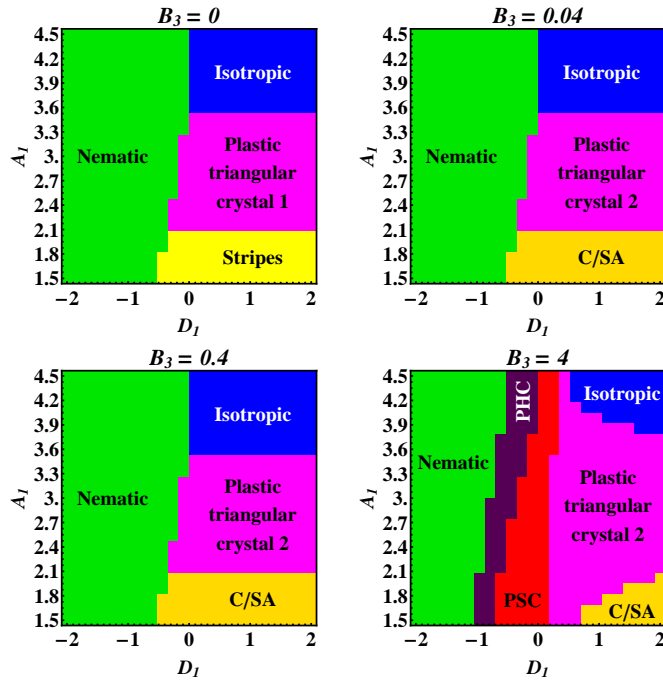


Figure 18. Phase diagrams for the parameters  $A_2 = 14$  and  $D_2 = 0.8$ . The relevant liquid crystalline phases are isotropic (blue), nematic (green), stripes (yellow), columnar/smectic A (C/SA, light orange), plastic triangular crystals (magenta), plastic honeycomb crystal (PHC, dark purple), and plastic square crystal (PSC, red). The cornered separation lines between different phases are due to the finite numerical resolution of the parameter space. (Reproduced from C. V. Achim, R. Wittkowski, and H. Löwen, *Stability of liquid crystalline phases in the phase-field-crystal model*, Phys. Rev. E 83 (2011), 061712, no. 6, DOI: 10.1103/PhysRevE.83.061712 © 2011 by the American Physical Society.)

### 3.3. Anisotropies in the PFC models

One of the most attractive features of the PFC-type models is that the anisotropies for various physical properties follow directly from the crystal structure. The anisotropy of the interfacial free energy has been addressed theoretically and numerically by several authors [33, 40–44], whereas the growth anisotropy has been evaluated numerically in 3D [42].

#### 3.3.1. Free energy of the liquid-solid interface

**3.3.1.1. Numerical results.** Backofen and Voigt [43] have determined the anisotropy of the crystal-liquid interfacial free energy for small 2D clusters from simulations performed using the 1M-PFC model. They have observed a strong dependence of the interfacial free energy on the distance from the critical point. The results have been fitted with the formula of Stashevich et al. [179] from low temperature expansion. Remarkably, the anisotropy shows strong size-dependence, when reducing the cluster size to a few particles. Comparable results have been obtained by Gránásy et al. [33, 38] for the equilibrium shapes in a broader reduced temperature range (see figure 19). Tóth et al. [28] evaluated the free energy and thickness of flat interfaces as a function of  $\epsilon$  via solving the ELE for the equilibrium  $(10\bar{1})$  triangular crystal-liquid interface, and have shown that mean-field critical exponents apply. A similar approach has been applied in 3D for a large number of orientations of the flat bcc-liquid interface forming at  $\epsilon = 0.3748$ . The orientation dependence of the interfacial free energy and the respective Wulff plot are presented in figure 20 [44]. Apparently, the rhombic-dodecahedral equilibrium shape [42] obtained from simulations performed using the EOM for the same  $\epsilon$  has been a growth form. It became also evident that the usual cubic harmonic expansion is not sufficient for reproducing reasonably the anisotropy even if terms up to

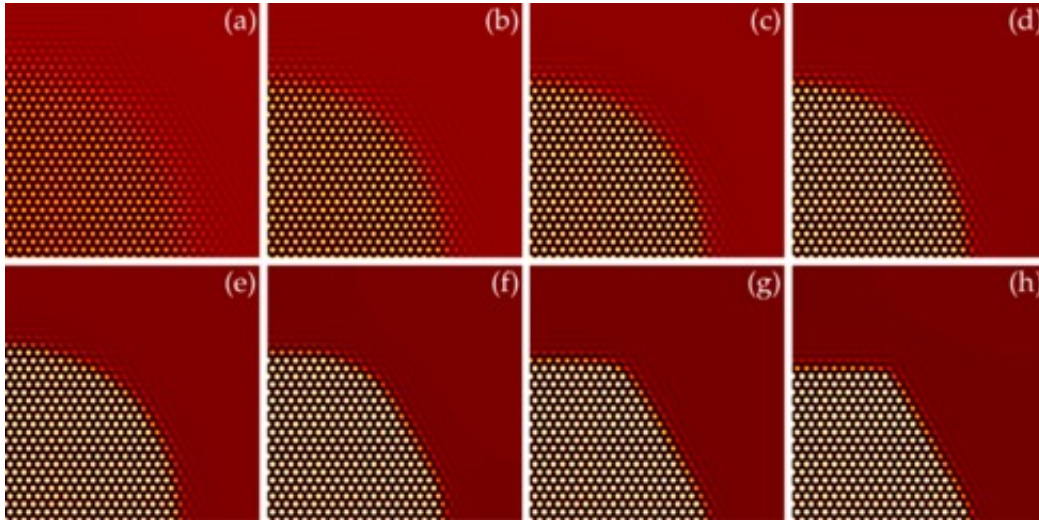


Figure 19. Equilibrium shape for the 1M-PFC model as determined by solving the EOM vs. reduced temperature  $\epsilon$  in the absence of noise [33]. (a) - (h):  $\epsilon = 0.05, 0.10, 0.15, 0.20, 0.25, 0.30, 0.325,$  and  $0.35$ . Notice that the interface thickness decreases while the anisotropy increases with an increasing distance from the critical point. The computations have been performed on a  $1024 \times 1024$  rectangular grid (the upper right quarter of the simulations is shown), whereas the crystalline fraction was  $\approx 0.3$ . Equilibration has been performed for a period of 106 dimensionless time steps. Reduced particle density maps are shown. (Reproduced from L. Gránásy, G. Tegze, G. I. Tóth, and T. Pusztai, *Phase-field crystal modelling of crystal nucleation, heteroepitaxy and patterning*, Philos. Mag. 91 (2011), 123-149, no. 1, DOI: 10.1080/14786435.2010.487476 © 2011 by Taylor & Francis.)

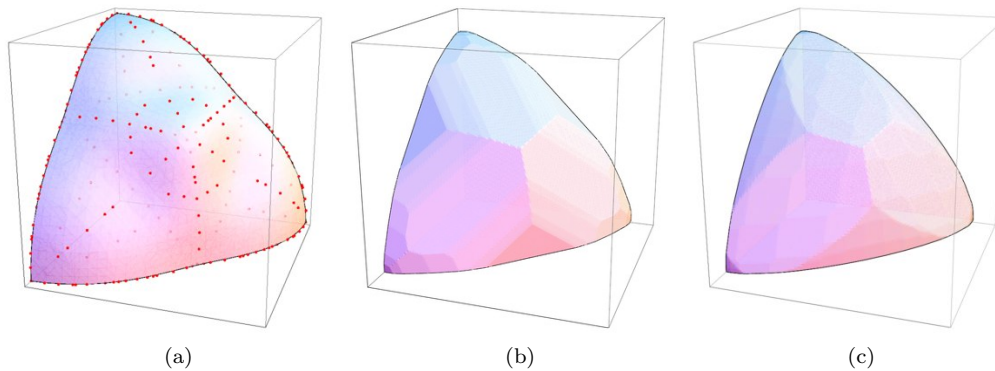


Figure 20. Anisotropy of the bcc-liquid interfacial free energy at  $\epsilon = 0.3748$  evaluated numerically for the single-component 1M-PFC model and the respective equilibrium shapes [44]. (a) Gamma plot. Red dots represent the directions for which the interfacial free energy has been evaluated. The surface is a seventh-order cubic harmonics fit. Heavy dots are on the viewer's side of the surface. Light dots are on the other side of the surface. (b) Wulff shape evaluated from the red dots in the gamma plot. (c) The Wulff shape evaluated from a seventh-order cubic harmonics fit to the gamma plot.

seventh order are considered.

**3.3.1.2. Analytical results.** Wu and Karma [40] have used multi-scale analysis close to the critical point ( $0 < \epsilon \ll 1$ ) to evaluate the anisotropy of the interfacial free energy. They have approximated the EOM of the 1M-PFC model by a set of coupled equations describing the time evolution of the amplitudes of the dominant density waves. The analysis of the stationary solution led to an anisotropy that is independent of the reduced temperature  $\epsilon$ . This finding accords with those of Majaniemi and Provatas [41], who have used a simple coarse-graining technique, the local volume averaging method, for deriving amplitude equations for liquid-solid interfaces broad relative to the periodicity of the crystalline phase. In both studies, the temperature-independent anisotropy is a direct consequence of the approxima-

tions that lead to weakly fourth-order amplitude theories of the Ginzburg-Landau type, in which all material parameters can be scaled out from the free-energy functional [40, 41]. Accordingly, the anisotropy of the interfacial free energy depends only on the crystal structure. However, this independence of the anisotropy from temperature is unphysical, as it must vanish when the correlation length (the width of the liquid-solid interface) diverges in the critical point. In contrast to these phenomenological coarse-graining techniques, the renormalisation-group-based approaches by Athreya, Goldenfeld, and Dantzig [131] lead to higher-order amplitude equations, from which the temperature cannot be scaled out; i. e., a temperature-dependent anisotropy is expected as found in the virtually exact numerical studies.

### 3.3.2. Growth anisotropy

Tegze et al. [42] have investigated the growth rate anisotropy in the 1M-PFC model at  $\epsilon = 0.3748$  for freezing to the bcc, hcp, and fcc structures. Diffusion-controlled layerwise crystal growth has been observed, a mechanism that is consistent with two-dimensional nucleation. The predicted growth anisotropies were found to decrease with increasing thermodynamic driving force (or velocity) consistently with kinetic roughening expected on the basis of 1M-PFC simulations performed in two spatial dimensions [38].

### 3.4. Glass formation

One of the most intriguing phenomena that may happen during solidification is glass formation, a process by which the undercooled liquid is transformed into an amorphous solid. An early 1M-PFC study for single-component system by Berry et al. [46] relying on conservative overdamped dynamics indicated a first-order phase transition for this phase change, whereas the amorphous structure resembled closely to the glass structure obtained by embedded-atom-potential (EAP) molecular dynamics simulations for glassy Fe or Ni [180, 181]. These findings have been confirmed for the 1M-PFC model by Tóth et al. [140] and for the EOF-PFC model fitted to Fe by Tóth et al. [28] and Gránásy et al. [33]. In a more recent study, Berry, and Grant [47] have addressed glass formation in the framework of the monatomic and binary versions of the VPFC model with equation(s) of motion like equation (64) considering inertia and damping. They have shown that important aspects of glass formation can be reproduced over multiple time scales, including the agreement with mode-coupling theory (MCT) for underdamped liquids at low undercoolings and a rapidly growing dynamic correlation length that can be associated with a fragile behaviour. It appears that in the original PFC model glass formation takes place via a first-order phase transition, while the monatomic VPFC model behaves like poor glass formers, whereas the binary VPFC model displays features consistent with good glass formers.

### 3.5. Phase-field-crystal modelling of foams

Working at extreme distances from the critical point, Guttenberg, Goldenfeld, and Dantzig [61] have shown that the 1M-PFC model can be used to describe the formation of foams. Under such conditions, the free energy of the periodic phases exceeds that for a mixture of two immiscible liquids – a situation that leads to the appearance of a foam-like structure coarsening with time. Starting from this observation, the authors present a simple PFC-type continuum scalar theory of wet and dry foams (see figure 21).

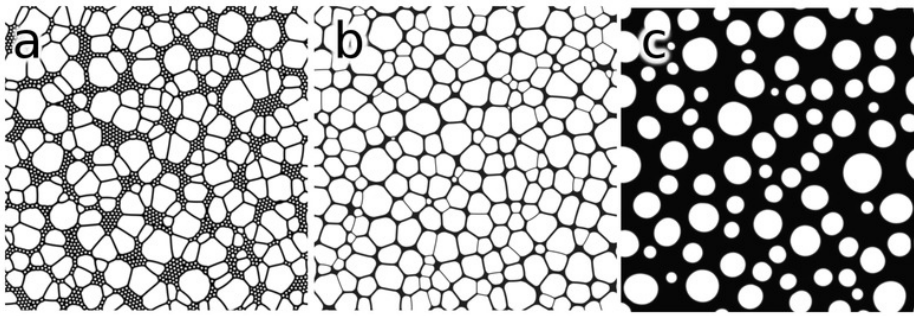


Figure 21. Foam structures predicted by the MPFC model. (a) Coexisting atoms and large cell foam. (b) Dry foam with no residual atoms. (c) Wet foam with circular bubbles. (Reproduced with permission from N. Guttenberg, N. Goldenfeld, and J. Dantzig, *Emergence of foams from the breakdown of the phase field crystal model*, Phys. Rev. E 81 (2010), 065301R, no. 6, DOI: 10.1103/PhysRevE.81.065301 © 2010 by the American Physical Society.)

### 3.6. Coupling to hydrodynamics

An interesting approach has been brought forward recently by Ramos et al. in reference [182]. It couples the PFC dynamics of the form of equation (1) to a Stokes-type dynamics as well as to an external pinning potential. The general set of equations the authors arrive at is given by

$$\begin{aligned} \frac{\partial \rho}{\partial t} &= -\nabla_{\mathbf{r}} \mathbf{g}, \\ \frac{\partial g_i}{\partial t} &= -\rho \partial_i \frac{\delta H_{\text{int}}}{\delta \rho} + \rho f_i - \eta g_i + \nu_i, \end{aligned} \quad (117)$$

where the specific configurational energy contribution  $H_{\text{int}}$  needs to be specified depending on the system. Assuming a periodic system, it is specified in reference [182] as

$$H_{\text{int}} = \int d\mathbf{r} \left( \frac{\psi}{2} (-\epsilon + (1 + \nabla_{\mathbf{r}}^2)^2) \psi + \frac{\psi^4}{4} + \psi U_{\text{p}} \right). \quad (118)$$

In equations (117),  $\rho(\mathbf{r})$  and  $\mathbf{g}(\mathbf{r})$  refer to particle and momentum density, respectively. Moreover,  $f_i$  denotes the components of an external force vector and  $\nu_i(\mathbf{r}, t)$  denotes noise components. Furthermore,  $\eta$  is a dissipative coefficient and  $U_{\text{p}}$  accounts for the pinning potential.

Even if at first glance the coupled set of equations (117) looks like a first step towards coupling of the PFC model based on equation (1) to a full Navier-Stokes (NS) type equation and thus to hydrodynamic motion, a respective extension of equations (117) is not straightforward due to the simple relation between particle density  $\rho(\mathbf{r})$  and momentum density  $\mathbf{g}(\mathbf{r})$  assumed. Thus instead of providing a step towards an extension of PFC models towards hydrodynamics, equations (117) rather provide a general framework for the inclusion of inertia effects in PFC models. The latter issue has also been addressed in references [128, 183, 184], where it was shown that the consideration of inertia terms allows to include fast degrees of freedom into the PFC approach. Furthermore, the authors of reference [128] have shown that inclusion of such fast degrees of freedom yields a two-stage relaxation process of the system. Chen et al. proved the thermodynamic consistency of such models with fast degrees of freedom [185]. Thereby, these authors validated from the viewpoint of thermodynamic theory that such a two-stage relaxation process can truly be regarded as an important qualitative feature of nonequilibrium pattern



formation in periodic systems. To do so, they developed a unified thermodynamic framework applying to both conventional PF models and PFC models with slow and fast degrees of freedom. Based on this framework it is now possible to validate also PFC models based on their thermodynamic consistency, as done previously in numerous cases for PF models (see reference [186] for examples). Experimental evidence of inertia contributions to the dynamics of a non-linear system in the form described by the PFC model with fast degrees of freedom can indeed be found for example in rapid solidification [128].

The coupling of PFC models to hydrodynamics, though, is still an open issue. It makes sense to distinguish two cases:

*Case (a):* Liquid-solid systems as, e. g., solidifying alloys, where hydrodynamic transport takes place in only the liquid phase. This implies that such systems can be treated in a multi-scale approach, where the PFC equation for the atomic scale dynamics in the interior of the solid is coupled to the long-range transport processes in the exterior, which – to be numerically efficient – couple only to the amplitude equation of the PFC equation. The reason is that in the case of PFC models it is the amplitude equation, which distinguishes between solid and liquid. Such amplitude equation approaches have been derived and solved numerically as computationally efficient representatives of PFC models, e. g., for diffusion limited polycrystalline grain growth [20] based on renormalisation group techniques (see section 3.1.5.1 for details). Since renormalisation for PFC models of equation (1) type does not directly yield NS-type equations and thus a coupling to hydrodynamics exploiting the above multi-scale idea, this is still an open issue.

*Case (b)* differs from the above picture in that it applies to systems, for which interatomic respectively intermolecular fluidic motion needs to be taken into account as, e. g., in polymers. Then one would desire a PFC model, where the PFC equation itself is directly coupled to a NS-type equation. A first step in that direction was done by Praetorius et al. [187]. They developed a PFC model with an advective term to simulate particles in a flowing solvent. To do so they followed the same route as Rauscher et al. [188] and Penna et al. [189] to derive a DDFT model for such systems, and approximated the latter further based on the Ramakrishnan-Yussouff approximation [85]. Strictly speaking the resulting PFC model applies only to potential flows. Furthermore, the coupling of the PFC variable  $\psi$  into the dynamic equations for the hydrodynamic field is constructed simply based on numerical arguments. More rigorous generalisations of these studies might require additional physically motivated coupling terms, as demonstrated for hydrogels in terms of the derivation of the corresponding PF model in reference [190] (see section 5.3 for details).

Just as in the PF case, one can expect efficient further advance of PFC models in the future. Progress will result from physical modelling concepts based upon the classical routes to patterned non-linear systems [1], analytical mathematical expansion techniques as the renormalisation group approach (see section 3.1.5.1 for details), and advanced numerical approaches [187, 191] in close comparison to experimental techniques.

#### 4. Phase-field-crystal models applied to nucleation and pattern formation in metals

Crystal nucleation can be handled in two different ways within the framework of PFC models [28, 33, 35]: (i) via finding the properties of the critical fluctuations (nuclei) by solving the ELE under appropriate boundary conditions (zero field gradients at the centre and unperturbed liquid phase in the far field), whose so-

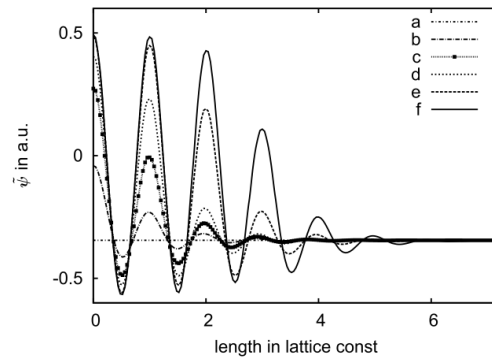


Figure 22. Particle density profiles for the critical fluctuations forming at different supersaturations (supersaturation decreases from a to f), as obtained by the adaptation of the string method for determining the extrema of the free-energy functional in the 1M-PFC model in two spatial dimensions. (Reproduced with permission from R. Backofen and A. Voigt, *A phase-field-crystal approach to critical nuclei*, *J. Phys.: Condens. Matter* 22 (2010), 364104, no. 36, DOI: 10.1088/0953-8984/22/36/364104 © 2010 by Institute of Physics Publishing.)

lution represents an extremum of the free-energy functional; (ii) by adding noise to the EOM. These approaches have their limitations. (i) is expected to work for small undercoolings, where the individual heterophase fluctuations do not interact. Furthermore, it is not immediately straightforward how one should address possible non-crystalline nucleation precursors. In turn, in the case of (ii) it is not clear conceptually, which fraction of the thermal fluctuations is already integrated into the free energy and which wavelengths should yet be added as noise to the EOM [95, 192, 193] – a question inherently related to the proper choice of the high frequency cutoff one needs to make to avoid an ultraviolet catastrophe in 3D [194, 195]. Furthermore, the addition of noise to the EOM changes the free energy, the phase diagram, and the interfacial properties. While, in principle, correction of these is possible via parameter renormalisation [196, 197], further study is needed in the case of PFC models. On the other hand, the original free-energy functional used in (i) seems to miss the effect of longer wavelength fluctuations, which could move the system out of a metastable state. Considering them, (i) and (ii) may be regarded as approaches that provide complementary, probably qualitative information of the crystallizing system, which converge when the amplitude of the noise tends to zero.

We note, however, that the results obtained via route (i) are more general than those obtained from (ii), as they follow directly from the free-energy functional, being therefore independent of the type of dynamics the EOM defines. Accordingly, results from (i) are valid even in cases, where the colloid-type diffusive dynamics is not applicable (e. g., metals). In this section, we review results obtained following route (i) for metals, or when pattern formation is governed by either chemical or surface diffusion. In turn, results obtained with the single-component PFC models with overdamped diffusive dynamics will be reviewed in section 4.3.

#### 4.1. Properties of nuclei from extremum principles

##### 4.1.1. Homogeneous nucleation

An adaptation of the string method to find the saddle point of the free-energy functional has been used by Backofen and Voigt [32] for determining the properties of the critical fluctuations in the 1M-PFC model in two spatial dimensions. The respective density profiles are shown in figure 22. It is evident that at large

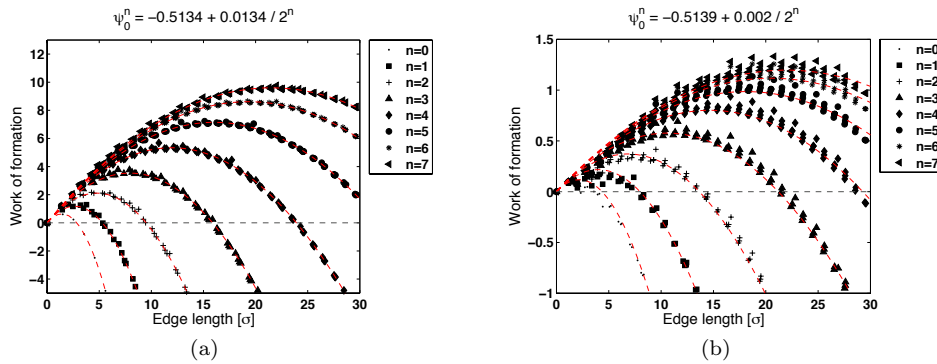


Figure 23. Nucleation barrier vs. size relationship obtained by solving the ELE for faceted nuclei ( $\epsilon = 0.5$ ) for the 1M-PFC model [28] in two spatial dimensions: (a) homogeneous crystal nuclei for  $\psi_0^n = -0.5134 + 0.0134/2^n$ , where  $n = 0, 1, 2, \dots, 7$ , respectively. (b) Heterogeneous crystal nuclei for  $\psi_0^n = -0.5139 + 0.002/2^n$ , where  $n = 0, 1, 2, \dots, 7$ , respectively. The lattice constant of the substrate is equal to the interparticle distance in the triangular crystal. Notice the substantial reduction of the nucleation barrier, a monolayer adsorption layer, and the contact angle of  $60^\circ$  determined by the crystal structure. (Reproduced from G. I. Tóth, G. Tegze, T. Pusztai, G. Tóth, and L. Gránásy, *Polymorphism, crystal nucleation and growth in the phase-field crystal model in 2D and 3D*, J. Phys.: Condens. Matter 22 (2010), 364101, no. 36, DOI: 10.1088/0953-8984/22/36/364101 © 2010 by Institute of Physics Publishing.)

supersaturations there are no bulk crystal properties at the centre of the smallest nuclei. They have also reported that small nuclei are faceted even though the large crystals are not.

Tóth et al. [28] have solved in two spatial dimensions the ELE of the 1M-PFC model for the appropriate boundary conditions (homogeneous supersaturated liquid in the far field) to find the free-energy extrema for faceted clusters far from the critical point ( $\epsilon = 0.5$ ), where even the large crystals are inherently faceted. Under such conditions, the free-energy surface has many local minima [28, 142] that map out the shape of the free-energy barrier for nucleation as a function of cluster size [see figure 23(a)]. It has also been reported that the effective interfacial free energy deduced from the barrier height using the hexagonal classical cluster model (valid owing to the interface sharp on the atomic scale) converges towards the free energy of the planar interface as the supersaturation decreases [28].

Tóth et al. [28] have performed a similar ELE analysis in 3D to study for heterophase fluctuations forming in the 1M-PFC model. They have evaluated the properties of crystal nuclei for bcc and fcc structures. It has been found that under the investigated conditions both the nucleation barrier and the driving force are fairly close for these structures, indicating comparable interfacial free energies and also Turnbull's coefficient<sup>1</sup> for the bcc and fcc structures under conditions ( $\epsilon = 0.3748$ ), where the thermodynamic properties of the crystalline phases are rather close [42]. This seems to contradict recent results from MD simulations performed using the EAP method [198]. It is worth noting, however, that Turnbull's coefficient varies with the type of interaction potential. For example, it is  $\approx 0.55$  for EAP metals of fcc structure [198], whereas  $\approx 0.36$  has been deduced for the fcc Lennard-Jones (LJ) system [199].

#### 4.1.2. Heterogeneous nucleation

The height of the nucleation barrier is often reduced by heterogeneities (walls, floating particles, templates, etc.), a phenomenon termed heterogeneous nucleation

<sup>1</sup>Turnbull's coefficient  $C_T$  is a reduced liquid-solid interfacial free energy defined via the relationship  $\gamma_{ls} = C_T \frac{\Delta H_f}{N_A^{1/3} v_m^{2/3}}$ , where  $\gamma_{ls}$ ,  $\Delta H_f$ ,  $N_A$ , and  $v_m$  are the total liquid-solid interfacial free energy, the molar heat of fusion, the Avogadro number, and the molar volume, respectively.  $C_T$  is expected to depend only on the crystal structure. Recent results indicate that besides structure the interaction potential also has influence on its magnitude.

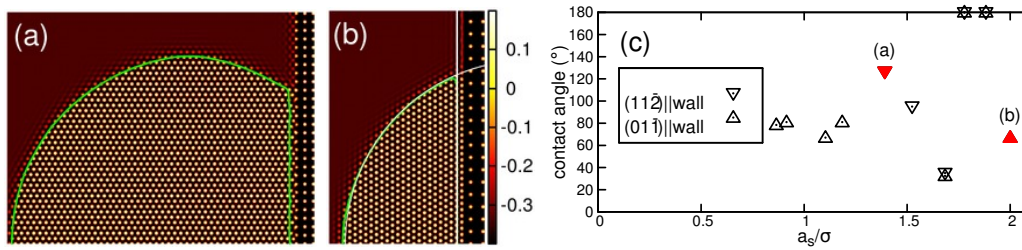


Figure 24. Heterogeneous crystal nucleation at a wall in two spatial dimensions from solving the ELE [140]: (a), (b) typical (non-faceted) nuclei obtained for  $\epsilon = 0.25$ ,  $\psi_0 = -0.341$ , while the ratio of the lattice constant of the substrate and the particle diameter is  $a_s/\sigma = 1.49$  and  $2.0$ , respectively, whereas the crystal orientations  $(11\bar{2})$  and  $(01\bar{1})$  are parallel with the wall. The intersection of the circular and linear fits (white lines) to the contour line (green line) defines the contact angle. (c) Contact angle vs.  $a_s/\sigma$  for  $\epsilon = 0.25$  and  $\psi_0 = -0.341$ . The red symbols indicate the states corresponding to panels (a) and (b). (Reproduced from G. I. Tóth, G. Tegze, T. Pusztai, and L. Gránásy, *Heterogeneous crystal nucleation: the effect of lattice mismatch*, Phys. Rev. Lett. 108 (2012), 025502, no. 2, DOI: 10.1103/PhysRevLett.108.025502 © 2012 by the American Physical Society.)

[200]. The efficiency of the heterogeneities in instigating freezing is influenced by a range of microscopic properties, such as crystal structure, lattice mismatch, surface roughness, adsorption, etc., which are often condensed into the contact angle used in the classical theory and coarse-grained continuum models. The atomic scale characteristics of the substrate surface, especially the lattice mismatch, are crucial from the viewpoint of the highly successful free-growth-limited model of particle-induced freezing by Greer and co-workers [200, 201] – a model in which cylindrical particles, whose circular faces (of radius  $R$ ) are ideally wet by the crystal, remain dormant during cooling until the radius of the homogeneous nuclei becomes smaller than  $R$  and free growth sets in. The PFC models are especially suitable to investigate such problems as they work on the diffusive time scale [12] and can handle systems containing as many as  $2.4 \times 10^7$  atoms [28].

Along this line, Tóth et al. [28] used a *periodic* external potential to incorporate a crystalline substrate into the ELE method for determining the properties of faceted heterogeneous nuclei. They have observed the adsorption of a monolayer of particles on the surface of substrate that reduced the formation energy of nuclei substantially and lead to a contact angle of  $60^\circ$  determined by the crystal structure [see figure 23(b)]. In a more recent ELE study, Tóth et al. [140] have shown for the 1M-PFC model in two spatial dimensions that the contact angle, the thickness of the crystal layer adsorbed on the substrate, and the height of the nucleation barrier vary non-monotonically with the lattice constant of a square-lattice substrate (see figure 24). They have also proven in two and three spatial dimensions that the free-growth-limited model of particle-induced freezing by Greer et al. [200, 201] is valid for larger nanoparticles and a small anisotropy of the interfacial free energy (see figure 25). Faceting due to either the small size of the foreign particle or a high anisotropy of the free energy of the liquid-solid interfacial free energy decouples free growth from the critical size of homogeneous nuclei.

#### 4.2. Pattern formation

Owing to the overdamped diffusive dynamics most of the PFC models assume, diffusional instabilities that lead to fingering of the propagating crystal front are inherently incorporated. In the case of a single-component PFC model, diffusive dynamics means that as the growing crystal (of larger particle density than the liquid) consumes the particles in the adjacent liquid; the only way they can be replenished is via long-range diffusion from the bulk liquid. Accordingly, a depletion zone forms ahead of the growing crystal [28, 38, 42, 202]. This resembles the behaviour of col-

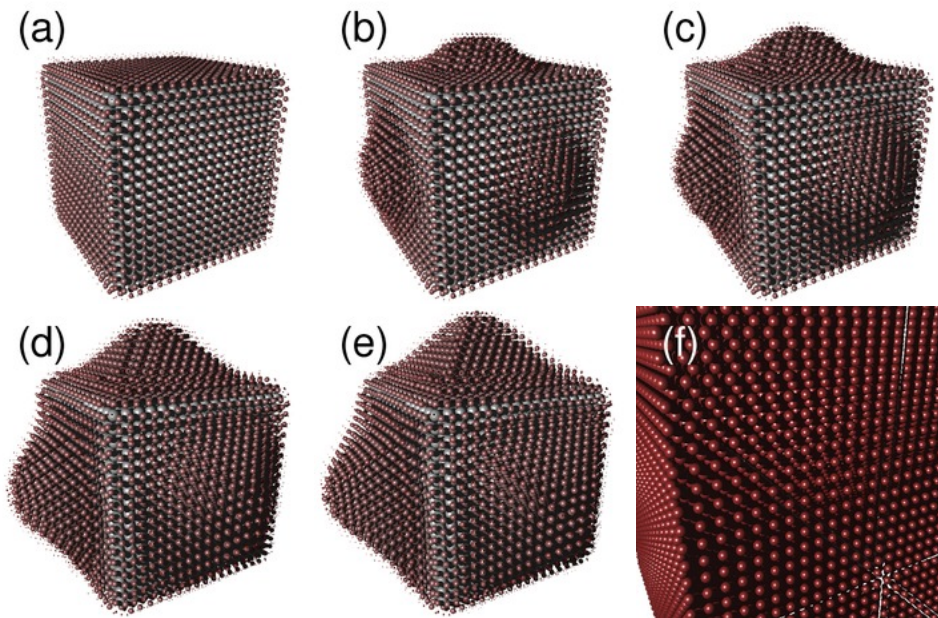


Figure 25. Free-growth limited bcc crystallization in 3D on a cube of sc structure as predicted by the ELE within the 1M-PFC model [140]. Here,  $\epsilon = 0.25$  and from left to right  $\psi_0 = -0.3538, -0.3516, -0.3504, -0.3489, -0.3482,$  and  $-0.3480$ , respectively. The linear size of the substrate is  $L_s = 16a_{\text{bcc}}$ , while  $a_{\text{bcc}}$  is the lattice constant of the stable bcc structure. Spheres centred on density peaks are shown, whose size increases with the height of the peak. Colour varies with peak height, interpolating between red (minimum height) and light grey (maximum height). The ELE has been solved on a  $256 \times 256 \times 256$  grid. (Reproduced from G. I. Tóth, G. Tegze, T. Pusztai, and L. Gránásy, *Heterogeneous crystal nucleation: the effect of lattice mismatch*, Phys. Rev. Lett. 108 (2012), 025502, no. 2, DOI: 10.1103/PhysRevLett.108.025502 © 2012 by the American Physical Society.)

loidal suspensions, in which the micron-sized colloid particles move by Brownian motion in the carrier fluid. Relying on this similarity, the single-component PFC models can be considered as reasonable tools to address colloidal crystal aggregation. One may though get rid of this type of mass-diffusion-controlled dynamics when driving the system strongly enough for a diffusion-controlled to diffusionless transition [38]. These phenomena are not necessarily present in the phenomenological coarse-grained PFC models, where the change in density upon crystallization is not always taken into account – models that might be considered, therefore, as a reasonable description of metallic alloys. Diffusive dynamics is furthermore appropriate on the surface of substrates, where the adsorbed particles indeed move by diffusion in a periodic potential. 2D PFC models relying on the interplay of the inter-particle forces and a periodic external potential representing the symmetries of the substrate can be used to capture pattern formation on such surfaces.

#### 4.2.1. PFC modelling of surface patterns

A combination of computer simulations with the solution of amplitude equations for PFC models equipped with periodic potentials has been used to investigate a range of surface phenomena including incommensurate to commensurate transitions for triangular surface layers on a square-lattice substrate [183, 184, 203], the deposition of monolayers on quasi-crystalline substrates [204], sliding friction [182, 184], and the formation of quantum dots/islands on nanomembranes [205, 206] (see figure 26).

Muralidharan and Haataja [48] have extended the PFC model for describing stress-induced alloying of bulk-immiscible binary systems on a substrate by adding a potential energy term describing the substrate and a regular solution term. Fixing the model parameters to data for CoAg/Ru(0001), they demonstrated that

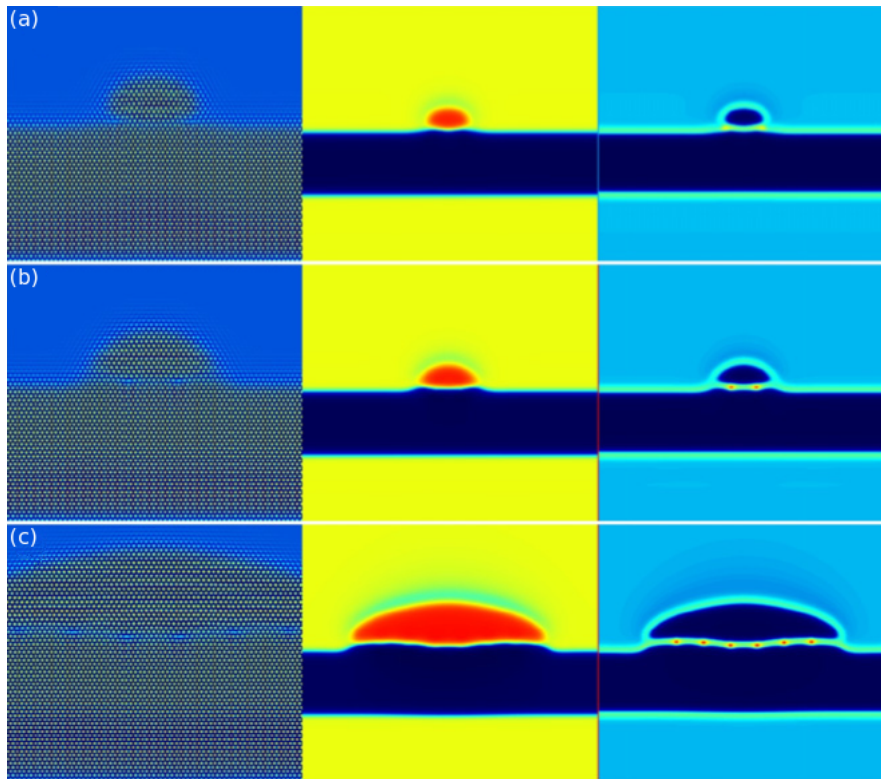


Figure 26. Growth of an island on a nanomembrane of approximately 30 atomic layers thickness at times (a)  $t = 60000$ , (b)  $t = 80000$ , (c)  $t = 400000$  as predicted by the amplitude equations of reference [206]. Similar to figure 9, the left, middle, and right columns correspond to the results of the total particle density, the difference of the particle densities for the two components, and the local free-energy density, respectively. Also for clarity, the particle density images have been expanded by a factor of two. (Reproduced with permission from K. R. Elder and Z.-F. Huang, *A phase field crystal study of epitaxial island formation on nanomembranes*, *J. Phys.: Condens. Matter* 22 (2010), 364103, no. 36, DOI: 10.1088/0953-8984/22/36/364103 © 2010 by Institute of Physics Publishing.)

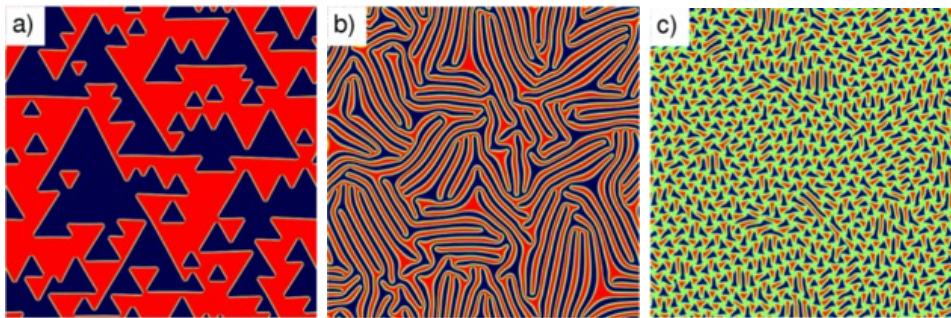


Figure 27. Surface patterns the amplitude equations predict for a decreasing dimensionless coupling  $u_0$  between the layer and the substrate [49]. From left to right:  $u_0 = 12.1 \times 10^{-3}$ ,  $3.2 \times 10^{-3}$ , and  $0.87 \times 10^{-3}$ , respectively. Colouring: fcc domains are blue, hcp domains are red, and the domain walls are green. (Reproduced with permission from K. R. Elder, G. Rossi, P. Kanerva, F. Sanches, S. C. Ying, E. Granato, C. V. Achim, and T. Ala-Nissila, *Patterning of heteroepitaxial overlayers from nano to micron scales*, *Phys. Rev. Lett.* 108 (2012), 226102, no. 22, DOI: 10.1103/PhysRevLett.108.226102 © 2012 by the American Physical Society.)

the model captures experimentally observed morphologies. A similar approach has been proposed by Elder et al. [49] using amplitude equations that allow large-scale simulations for stress-induced alloying in heteroepitaxial overlayers. Quantitative predictions, that are in an excellent agreement with experiments, have been obtained for the stripe, honeycomb, and triangular superstructures emerging in the metal/metal systems, Cu on Ru(0001) and Cu on Pd(111) (see figure 27).

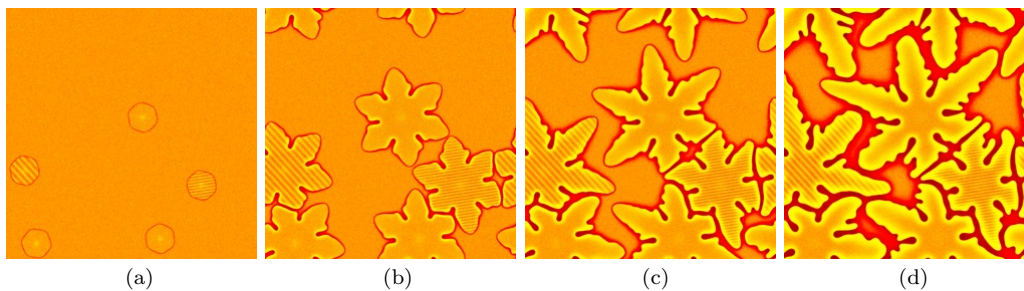


Figure 28. Growth of five dendrites in the binary PFC model (the distribution of the field  $\hat{\psi}$  is shown). The snapshots taken at 1000, 5000, 10000 and 20000 time steps are shown. The simulations have been performed on a  $16384 \times 16384$  grid, using a semi-implicit spectral method [164]. (Reproduced from T. Pusztai, G. Tegze, G. I. Tóth, L. Környei, G. Bansel, Z. Fan, and L. Gránásy, *Phase-field approach to polycrystalline solidification including heterogeneous and homogeneous nucleation*, *J. Phys.: Condens. Matter* 20 (2008), 404205, no. 40, DOI: 10.1088/0953-8984/20/40/404205 © 2008 by Institute of Physics Publishing.)

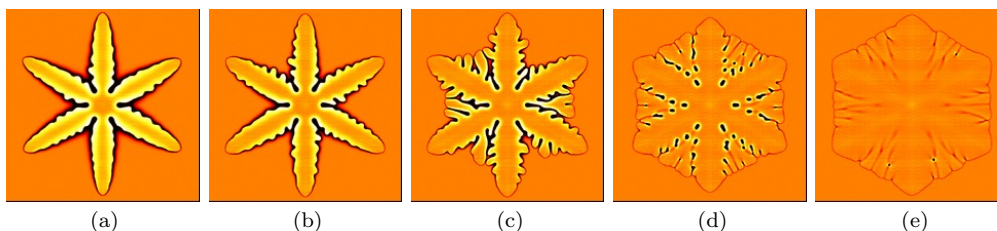


Figure 29. Morphological transition from dendritic needle crystals to compact hexagonal shape with increasing driving force for crystallization [29]. Conditions/properties are as described for dendrites in reference [164] except that the initial total number densities are  $\psi_0 = 0.009, 0.0092, 0.0094, 0.0096,$  and  $0.0098$  (from left to right). The reduced number density  $\hat{\psi}$  is shown. Notice the reducing contrast of the images from left to right indicating an increasing solute trapping. A  $8192 \times 8192$  grid has been used. (Reproduced from G. Tegze, *Application of atomistic phase-field methods to complex solidification problems*, PhD Thesis, Eötvös University, Budapest, Hungary (2009).)

#### 4.2.2. Pattern formation during binary solidification

**4.2.2.1. Dendritic freezing.** The possibility of growing solutal dendrites has been first addressed within numerical 1M-PFC simulations by Elder et al. [26]. Studies of the transformation kinetics for many particles including several dendrites have been performed using the same approach by Pusztai et al. [27] for system sizes containing about  $1.6 \times 10^6$  atoms (see figure 28). Tegze [29] has investigated the behaviour of solutal dendrites using binary 1M-PFC simulations of similar size. With increasing driving force obtained by increasing the total number density, transitions from dendritic needle crystals to compact hexagon shape crystals have been observed as in the conventional PF models (see figure 29). It has also been shown that (i) a steady state tip velocity is attained after a time, and (ii) tip oscillations do not occur, i. e., from the viewpoint of side branch formation the dendrite tip works like a selective amplifier of the fluctuations at the tip (see figure 30).

**4.2.2.2. Eutectic solidification.** Eutectic solidification in binary 1M-PFC simulations has been first observed in two spatial dimensions in the seminal paper by Elder et al. [26]. The formation of lamellar eutectic grains has been explored by Elder, Huang, and Provatas [31] using an approach based on amplitude equations (see figure 31). For the relatively large lattice mismatch they assumed for the two crystalline phases (8.4% in equilibrium), spontaneous nucleation of dislocations at the lamellar interfaces has been observed – a phenomenon expected to modify the spacing selection mechanism predicted by earlier eutectic solidification theories. Larger-scale binary 1M-PFC simulations relying on a numerical solution

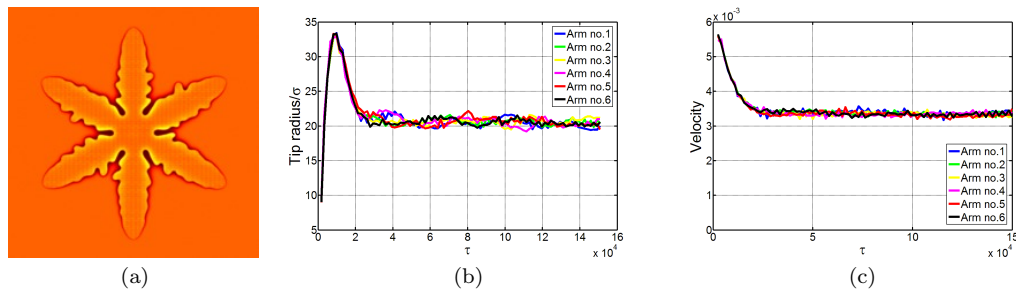


Figure 30. Analysis of a solutal dendrite grown in the binary 1M-PFC model [29]. The dendrite arms are numbered clockwise from the top arm. Apparently, there are no tip radius or velocity oscillations and steady state growth is reached after  $\approx 4000$  time steps. A  $8192 \times 8192$  grid has been used and  $\psi_0 = 0.0092$ , whereas other conditions as for figure 25 are present. (Reproduced from G. Tegze, *Application of atomistic phase-field methods to complex solidification problems*, PhD Thesis, Eötvös University, Budapest, Hungary (2009).)

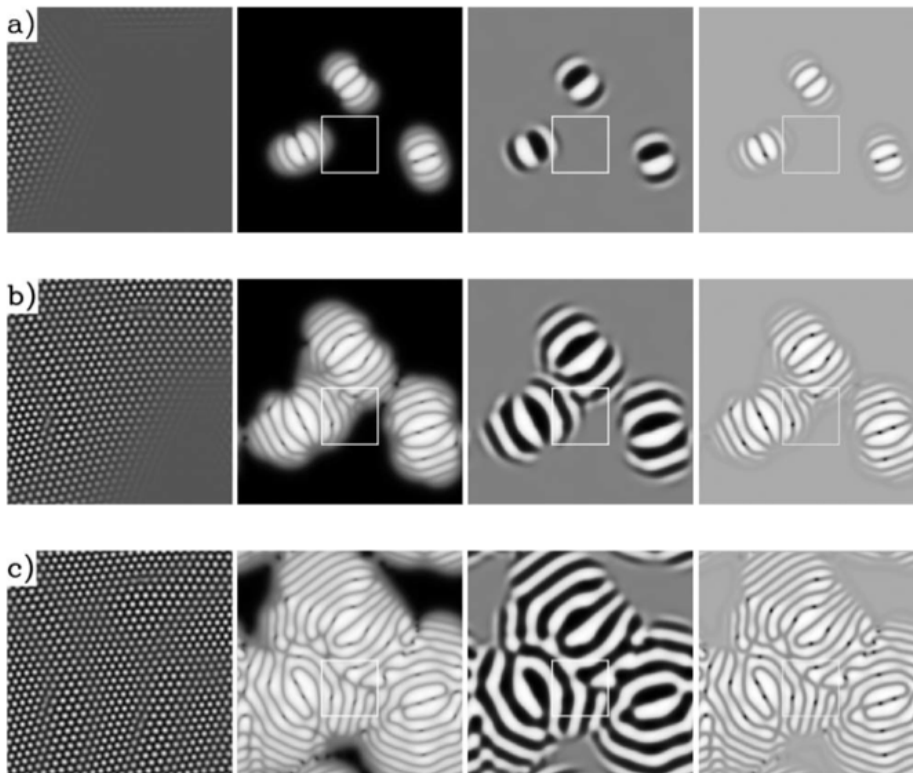


Figure 31. Time evolution of equiaxed eutectic solidification within the amplitude equation formalism proposed by Elder, Huang, and Provatas [31]. Panels (a), (b), and (c) correspond to dimensionless times 30000, 60000, and 105000, respectively. From left to right the columns display the reduced total number density in the boxed region, the coarse-grained number density, the reduced difference of the number densities for the two species, and the local free-energy density. Dislocations appear as small black dots in the local free-energy density. (Reproduced with permission from K. R. Elder, Z.-F. Huang, and N. Provatas, *Amplitude expansion of the binary phase-field-crystal model*, Phys. Rev. E 81 (2010), 011602, no. 1, DOI: 10.1103/PhysRevE.81.011602 © 2010 by the American Physical Society.)

of the EOMs (73) and (74) in two spatial dimensions imply owing to the diffusive dynamics of the total particle density in the binary 1M-PFC model, eutectic colonies may form even in binary systems [28] (see figure 32). Here, the morphological change occurs as a result of the diffusional instability emerging from the diffusive EOM, many of the PFC models assume. Using the same approach in 3D, eutectic crystallization to the bcc structure has been reported by Tóth et al. [28] (see figure 33). These atomistic simulations indicate a remarkable time evolution of the eutectic pattern after solidification.



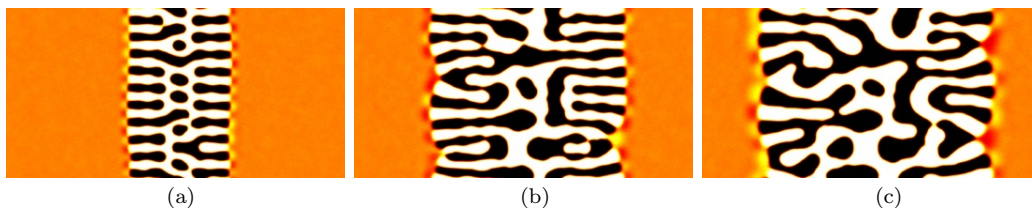


Figure 32. Snapshots of eutectic solidification on the atomistic scale in the binary 1M-PFC model in two spatial dimensions [28]: composition  $\hat{\psi}$  maps corresponding to  $2 \times 10^5$ ,  $6 \times 10^5$ , and  $10^6$  time steps are shown. White and black denote the two crystalline phases, while yellow stands for the liquid phase. The simulation has been performed on a  $2048 \times 1024$  rectangular grid. Crystallization has been started by placing a row of supercritical crystalline clusters of alternating composition into the simulation window. Interestingly, the eutectic pattern evolves inside the solid region on a timescale comparable to the timescale of solidification. (Reproduced from G. I. Tóth, G. Tegze, T. Pusztai, G. Tóth, and L. Gránásy, *Polymorphism, crystal nucleation and growth in the phase-field crystal model in 2D and 3D*, J. Phys.: Condens. Matter 22 (2010), 364101, no. 36, DOI: 10.1088/0953-8984/22/36/364101 © 2010 by Institute of Physics Publishing.)

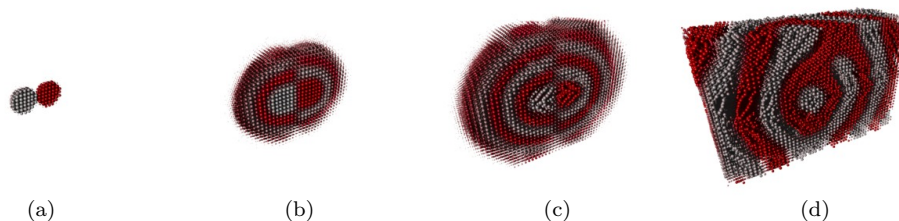


Figure 33. Snapshots of eutectic solidification as predicted by the binary 1M-PFC model in 3D [28]: time elapses from left to right. The simulation has been performed on a  $450 \times 300 \times 300$  rectangular grid. Solidification has been started by placing two touching supercritical bcc clusters of different compositions into the simulation window. Remarkably, the nanoscale solid-phase eutectic pattern roughens on a timescale comparable to the time of solidification. Brown and grey colours denote the terminal solutions of the two crystalline phases. Spheres of size reflecting the height  $\psi$  of the total number density peak and coloured according to the local composition  $\hat{\psi}$  are centred to the particle density maxima. Only half of the simulation window is shown. (Reproduced from G. I. Tóth, G. Tegze, T. Pusztai, G. Tóth, and L. Gránásy, *Polymorphism, crystal nucleation and growth in the phase-field crystal model in 2D and 3D*, J. Phys.: Condens. Matter 22 (2010), 364101, no. 36, DOI: 10.1088/0953-8984/22/36/364101 © 2010 by Institute of Physics Publishing.)

### 4.3. Phenomena in the solid state

One of the most successful areas, where the PFC models make a real difference is the modelling of solid state transitions including grain-boundary dynamics, melting, crack formation, stress-induced morphology evolution, and the modelling of the Kirkendall effect, to mention a few.

#### 4.3.1. Dislocation dynamics and grain-boundary melting

Already the first paper on the PFC method [12, 50] has addressed grain boundaries and shown that the model automatically recovers the Read-Shockley relationship between grain-boundary energy and misorientation (see figure 34). It has also been shown that PFC models are ideal for modelling grain-boundary dynamics [12, 50] (see figure 34) and offers the possibility to link mechanical properties with the grain structure [50]. Two mechanisms of dislocation glide have been observed: for high strain rates, continuous glide is observed, while at lower strain rate the dislocation set into a stick-slip motion [51]. Grain-boundary melting has been addressed in several works [36, 37, 167]. It has been reported that dislocations in low-angle to intermediate-angle grain boundaries melt similarly until an angle-dependent first-order wetting transition occurs, when neighbouring melted regions coalesce. In the large-angle limit, the grain-boundary energy becomes increasingly uniform along its length and can no longer be interpreted in terms of individual dislocations (see figure 34). The difference between high- and low-angle boundaries appears to be reflected in the dependence of the disjoining potential on the width of the pre-melted layer  $w$ : it is purely repulsive for all widths for

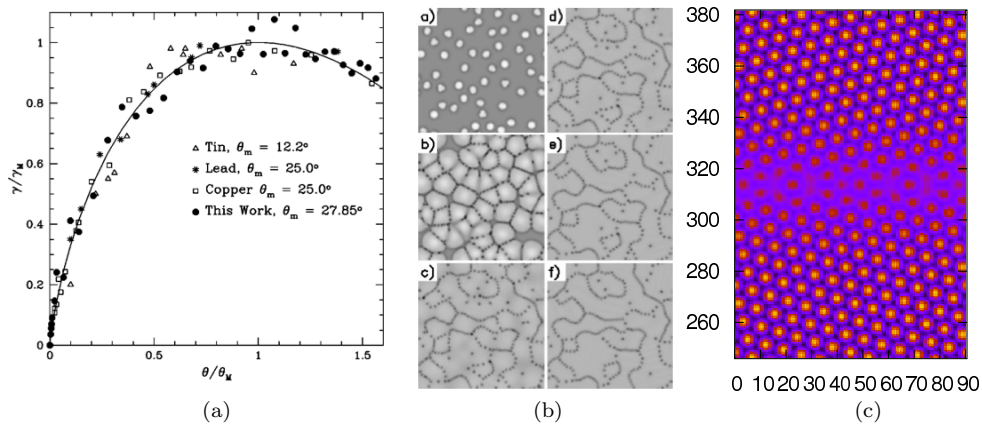


Figure 34. PFC modelling of defect and pattern formation in solids. From left to right: (a) grain-boundary energy vs. Read-Shockley relationship and (b) grain-boundary dynamics. (Reproduced with permission from K. R. Elder and M. Grant, *Modeling elastic and plastic deformations in nonequilibrium processing using phase field crystals*, Phys. Rev. E 70 (2004), 051605, no. 5, DOI: 10.1103/PhysRevB.75.064107 © 2004 by the American Physical Society.) (c) Grain-boundary melting at a large-angle grain boundary. (Reproduced with permission from J. Mellenthin, A. Karma, and M. Plapp, *Phase-field crystal study of grain-boundary premelting*, Phys. Rev. B 78 (2008), 184110, no. 18, DOI: 10.1103/PhysRevB.78.184110 © 2008 by the American Physical Society.)

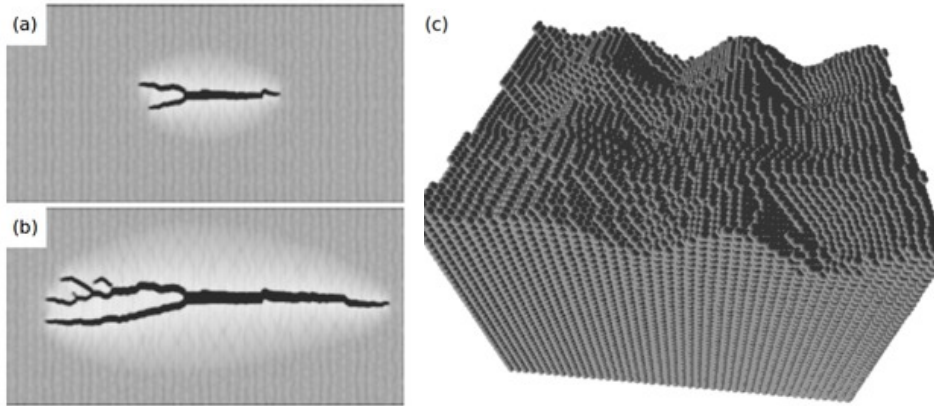


Figure 35. Crack formation (left) and strain-induced epitaxial islands (right) in the single-component 1M-PFC model. (a), (b) Snapshots of the energy density map taken at dimensionless times 25000 and 65000. (Reproduced with permission from K. R. Elder and M. Grant, *Modeling elastic and plastic deformations in nonequilibrium processing using phase field crystals*, Phys. Rev. E 70 (2004), 051605, no. 5, DOI: 10.1103/PhysRevB.75.064107 © 2004 by the American Physical Society.) (c) Gray scale image of epitaxial islands in an 1M-PFC simulation for a 4.8% tensile film. (Reproduced with permission from Z.-F. Huang and K. R. Elder, *Mesoscopic and microscopic modeling of island formation in strained film epitaxy*, Phys. Rev. Lett. 101 (2008), 158701, no. 15, DOI: 10.1103/PhysRevLett.101.158701 © 2008 by the American Physical Society.)

misorientations larger than a critical angle, however, it switches from repulsive at small  $w$  to attractive for large  $w$  [37].

#### 4.3.2. Crack formation and propagation

Elder and Grant [50] have demonstrated that the 1M-PFC model can be used to model crack propagation. A small notch cut out of a defect-free crystal placed under 10% strain in the vertical direction and filled with coexisting liquid has been used as a nucleation cite for crack propagation. Snapshots of crack development are shown in figure 35.

#### 4.3.3. Strain-induced morphologies

Huang and Elder [52] have studied strain-induced film instability and island formation using numerical 1M-PFC simulations and amplitude equations (see fig-

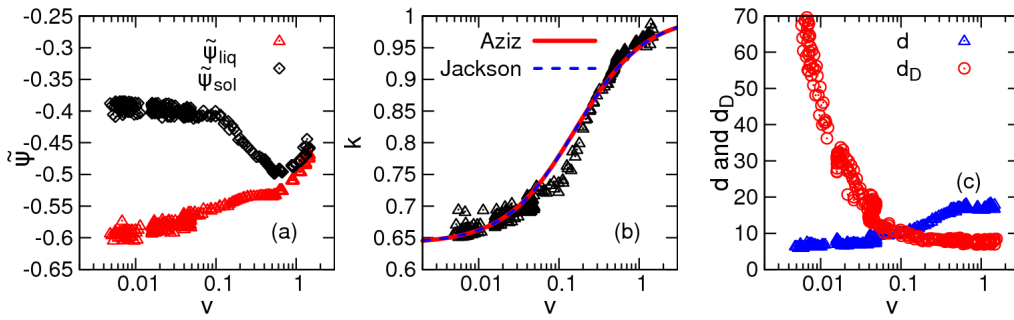


Figure 36. Density trapping as predicted by the single-component 1M-PFC model [38, 39]. (a) Coarse-grained particle densities  $\tilde{\psi}$  for the liquid and solid phases at the growth front as a function of growth velocity  $v$ . (b) Effective partition coefficient  $k$  defined using the liquidus and solidus densities vs. growth velocity. For comparison, fits of the models by Aziz [207] and Jackson et al. [208] are also displayed. (c) Comparison of the interface thickness  $d$  and the diffusion length  $d_D$  as a function of growth velocity. (Reproduced from G. Tegze, L. Gránásy, G. I. Tóth, J. F. Douglas, and T. Pusztai, *Tuning the structure of nonequilibrium soft materials by varying the thermodynamic driving force for crystal ordering*, *Soft Matter* 7 (2011), 1789-1799, no. 5, DOI: 10.1039/c0sm00944j © 2011 by Royal Society of Chemistry Publishing.)

ure 34). They have identified a linear regime for the island wave number scaling and recovered the continuum ATG instability in the weak strain limit. The ATG instability has been studied in two spatial dimensions by Spatschek and Karma [54] using a different amplitude equations approach. Qualitatively similar surface roughening has been reported by Tegze et al. [42] for heteroepitaxial body-centred tetragonal (bct) films grown on sc crystalline substrates of tuned lattice constant – a phenomenon interpreted in terms of the Mullins-Sekerka/ATG instability.

#### 4.3.4. Kirkendall effect

Elder, Thornton, and Hoyt [55] have used a simple extension of the binary 1M-PFC model incorporating unequal atomic mobilities to investigate different aspects of the Kirkendall effect. They have shown that the model indeed captures such phenomena as crystal (centre-of-mass) motion, pore formation via vacancy supersaturation, and enhanced vacancy concentration near grain boundaries.

#### 4.3.5. Density/solute trapping

In recent works by Tegze et al. [38, 39], it has been reported for the 1M-PFC model (of diffusive dynamics) that at large  $\epsilon$  ( $= 0.5$ ) and high driving force a transition from diffusion-controlled to diffusionless solidification can be observed, during which the interface thickness increases, whereas the density difference between the crystal and the liquid decreases drastically (see figure 36). This “density trapping” phenomenon is analogous to solute trapping observed in rapid solidification of alloys (where due to a lack of time for partitioning, solids of nonequilibrium compositions form) and can be fitted reasonably well using the models of Aziz [207] and Jackson et al. [208]. In a very recent work, Humadi, Hoyt, and Provatas [45] have investigated solute trapping in the binary MPFC model. In agreement with the findings for density trapping, they have found that pure diffusive dynamics leads to a velocity-dependent partition coefficient that approaches unity for large velocities – consistently with the model of Aziz and Kaplan [209]. In contrast, the wavelike dynamics, the second-order time derivatives of the MPFC-type EOMs realize, leads to a solute trapping behaviour similar to the predictions of Galenko et al. [210].

#### 4.3.6. Vacancy/atom transport in the VPFC model

The VPFC model by Chan, Goldenfeld, and Dantzig [56] is one of the most exciting extensions of the original PFC approach. The extra term added to the free

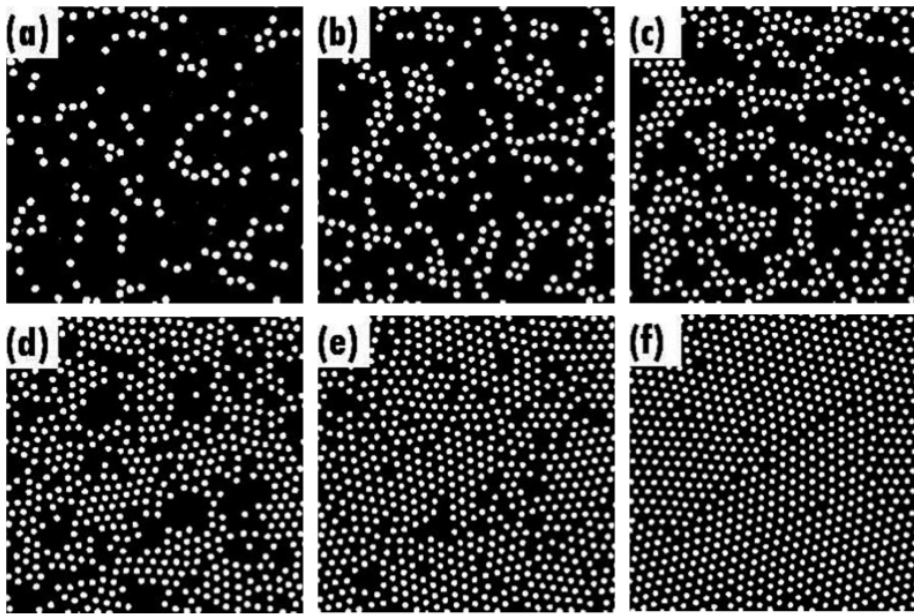


Figure 37. VPFC modelling of fluid and crystalline states of different particle densities. The number of atoms increases from left to right and from top to bottom. (Reproduced with permission from P. Y. Chan, N. Goldenfeld, and J. Dantzig, *Molecular dynamics on diffusive time scales from the phase-field-crystal equation*, Phys. Rev. E 79 (2009), 035701R, no. 3, DOI: 10.1103/PhysRevE.79.035701 © 2009 by the American Physical Society.)

energy makes particle density non-negative and allows for the formation of individual density peaks (“atoms” forming the fluid) and vacancies in the crystal. This, combined with the MPFC EOM (64), that considers inertia and damping, makes it a kind of MD-like approach working on a still far longer time scale than the usual MD simulations. Accordingly, one can obtain configurations that look like snapshots of the fluid state (see figure 37) and may evaluate the structure factor for the fluid state, which is evidently impossible for the original PFC model. (Apparently, similar images can be obtained in the 1M-PFC model as a *transient state* during solidification [38], however, with different dynamics owing to the differences in free energy and EOM.)

A comparison with another recent development, termed the diffusive molecular dynamics (DMD) technique, by Li et al. [211] would be very interesting. The latter approach works on the diffusive time scale too, while maintaining atomic resolution, by coarse-graining over atomic vibrations and evolving a smooth site-probability representation.

## 5. Phase-field-crystal modelling in soft matter physics

### 5.1. Applications to colloids

In this section, we review results obtained using different PFC models relying on overdamped conservative dynamics – a reasonable approximation for colloidal crystal aggregation. We concentrate on three major areas: crystal nucleation, pattern formation in free growth, and pattern formation in the presence of external potentials.

As mentioned previously, using of the EOM for simulating crystallization is not without difficulties. In the DDFT-type models, the system cannot leave a metastable state (e. g., the homogeneous initial fluid) unless Langevin noise representing thermal fluctuations is added to the EOM. This raises, however, essential

questions: considering the number density an ensemble-averaged quantity, all the fluctuations are (in principle) incorporated into the free-energy functional. Adding noise to the EOM, a part of the fluctuations might be counted twice [95, 192]. If in turn the number density is viewed as being coarse-grained in time, there is phenomenological motivation to add a noise term to the EOM [193]. The latter approach is appealing in several ways: crystal nucleation is feasible from a homogeneous state and capillary waves appear at the crystal-liquid interface. To investigate how nucleation and growth happen on the atomistic level, a conserved noise term is usually incorporated into the EOM [see equations (60)-(63)]. To overcome some difficulties occurring when discretising the noise [194, 195], coloured noise obtained by filtering out the unphysical short wavelengths smaller than the inter-particle distance is often used (this removes both the ultraviolet catastrophe expected in 3D [212] and the associated dependence of the results on spatial resolution). The majority of the studies we review below follows this approach.

### 5.1.1. Nucleation in colloidal crystal aggregation

#### 5.1.1.1. Homogeneous nucleation.

*The effect of noise.* A systematic study of the effect of the noise strength on the grain size distribution performed in two spatial dimensions by Hubert et al. [34] for the original 1M-PFC model implies that grain size decreases with increasing noise amplitude, resulting in both a smaller average grain size and a reduced maximum grain size. They have distinguished two regimes regarding the cluster size distribution: for small noise amplitudes a bimodal cluster size distribution is observed, whereas for large noise amplitudes a monotonically decreasing distribution is reported.

*Phase selection in 2D and 3D.* Mounting evidence indicates that the classical picture of crystal nucleation, which considers heterophase fluctuations of only the stable phase, is oversimplified. Early analysis by Alexander and McTague suggests a preference for bcc freezing in simple liquids [213]. Atomistic simulations for the LJ system have verified that small heterophase fluctuations have the metastable bcc structure, and even larger clusters of the stable fcc structure have a bcc interface layer [214], while the ratio of the two phases can be tuned by changing the pressure [215]. Composite bcc-fcc nuclei have also been predicted by continuum models [216]. Two-stage nucleation has been reported in systems that have a metastable critical point in the undercooled liquid (including solutions of globular proteins [217]); the appearance of the crystalline phase is assisted by dense liquid droplets, whose formation precedes and helps crystal nucleation [218]. Recent studies indicate a similar behaviour in simple liquids such as the LJ [219] or hard-sphere (HS) [220] fluids, where a dense liquid or amorphous precursor assists crystal nucleation. Analogous behaviour has been reported for colloidal systems in two spatial dimensions [221] and 3D [222]. These findings imply that the nucleation precursors are fairly common. Since the 1M-PFC model has bcc, fcc, and hcp stability domains [28], the appearance of an amorphous phase and two-step nucleation has also been reported [46], and the 2M-PFC model incorporates the 1M-PFC model [132]. This class of the dynamic PFC models is especially suitable for investigating phase selection during freezing of undercooled liquids.

In two spatial dimensions, it has been shown within the framework of the 1M-PFC model that at relatively small supersaturations direct crystal nucleation takes place. Increasing the thermodynamic driving force, first copious crystal nucleation is observed, and at higher driving forces an amorphous precursor precedes crys-

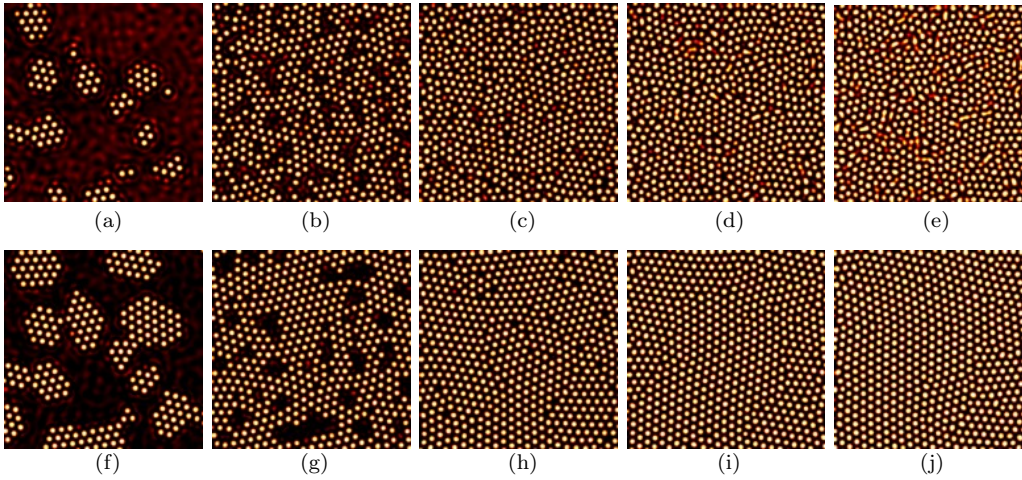


Figure 38. Snapshots of early and late stages of isothermal solidification in 1M-PFC quenching simulations performed in two spatial dimensions with initial reduced particle densities of  $\psi_0 = -0.55, -0.50, -0.45, -0.40$  and  $-0.35$  [33]. (a)-(e): Early stage: the respective reduced times are  $\tau/\Delta\tau = 10000, 3000, 1500, 1000$ , and  $700$ . (f)-(j): Late stage: the same areas are shown at reduced time  $\tau/\Delta\tau = 60000$ . Reduced particle density maps in  $418 \times 418$  sized fractions of  $2048 \times 2048$  sized simulations are shown. Other simulation parameters were  $\epsilon = 0.75$  and  $\alpha = 0.1$  (noise strength). (Reproduced from L. Gránásy, G. Tegze, G. I. Tóth, and T. Pusztai, *Phase-field crystal modelling of crystal nucleation, heteroepitaxy and patterning*, Philos. Mag. 91 (2011), 123-149, no. 1, DOI: 10.1080/14786435.2010.487476 © 2011 by Taylor & Francis.)

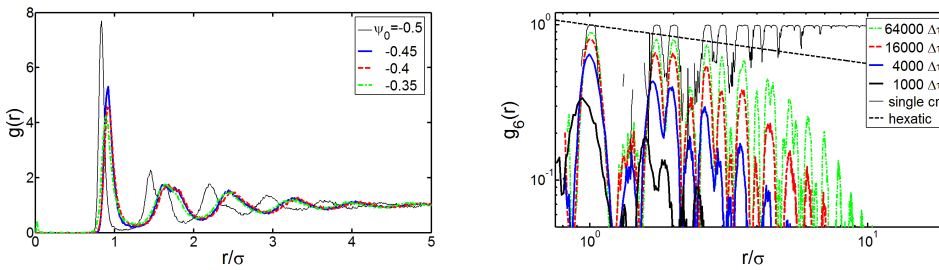


Figure 39. Structural properties evolving after quenching in 1M-PFC simulations [33]: (a) pair-correlation function  $g(r)$  for the early-stage solidification structures shown in figures 20(b)-(e). (b) Time evolution of the bond-order correlation function  $g_6(r)$  for  $\psi_0 = -0.4$  on log-log scale.  $g_6(r)$  is shown at  $\tau/\Delta\tau = 1000, 4000, 16000$ , and  $64000$ . For comparison, the upper envelope expected for the hexatic phase and the result for a single crystal are also shown. These curves describe an amorphous to polycrystalline transition [see figures 20(d) and 20(i)]. Notice that the upper envelope of the  $g_6(r)$  curves decay faster than expected for the hexatic phase. (Reproduced from L. Gránásy, G. Tegze, G. I. Tóth, and T. Pusztai, *Phase-field crystal modelling of crystal nucleation, heteroepitaxy and patterning*, Philos. Mag. 91 (2011), 123-149, no. 1, DOI: 10.1080/14786435.2010.487476 © 2011 by Taylor & Francis.)

talline nucleation [33] [see figures 38 and 39(a)]. Similarly to quenching experiments for two spatial dimensions colloidal systems [223], no hexatic phase is observed in the 1M-PFC quenching simulations [33, 38] [as demonstrated by the form of the radial decay of the bond-order correlation function [33], see figure 39(b)].

In 3D, a systematic dynamic study of the 1M/2M-PFC models by Tóth et al. [35] shows that in these systems the first appearing solid is amorphous, which promotes the nucleation of bcc crystals (see figure 40) but suppresses the appearance of the fcc and hcp phases. The amorphous phase appears to coexist with the liquid indicating a first-order phase transition between these phases in agreement with the observed nucleation of the amorphous state. Independent ELE studies determining the height of the nucleation barrier have confirmed that density and structural changes take place on different times scales [35]. This finding suggests that the two time scales are probably present independently of the type of dynamics assumed. These findings have been associated with features of the effective interaction potential deduced from the amorphous structure using Schommer's iterative method

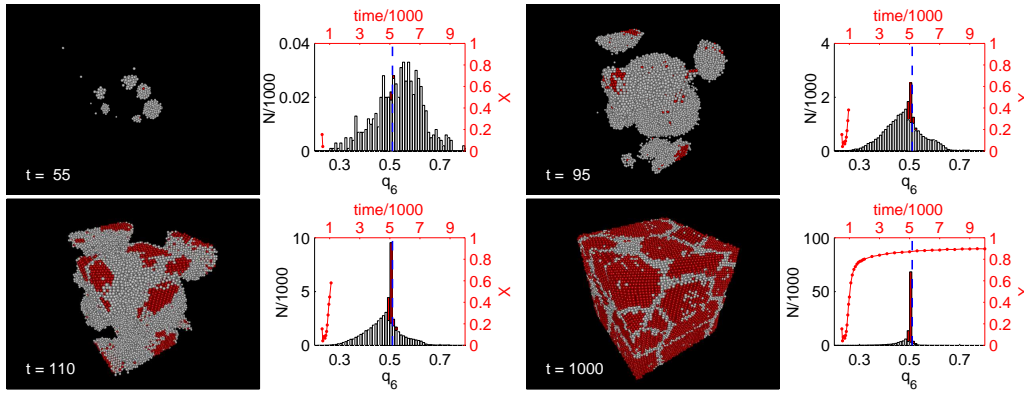


Figure 40. Two-step nucleation in the 1M-PFC model at  $\psi_0 = -0.1667$  and  $\epsilon = 0.25$  [35]. Four pairs of panels are shown, where  $t$  indicates the time elapsed,  $N$  is the total number of particles, and  $q_i$  is the bond orientational order parameter with index  $i$ . Left: snapshots of the density distribution taken at the dimensionless times  $\tau = 57.74t$ . Spheres of the diameter of the inter-particle distance centred on density peaks higher than a threshold ( $= 0.15$ ) are shown. They are coloured red if  $q_4 \in [0.02; 0.07]$  and  $q_6 \in [0.48; 0.52]$  (bcc-like) and light grey otherwise. Right: population distribution of  $q_6$  (histogram painted similarly) and the time dependence of the fraction  $X$  of bcc-like neighbourhoods (solid line). (Reproduced from G. I. Tóth, T. Pusztai, G. Tegze, G. Tóth, and L. Gránásy, *Amorphous nucleation precursor in highly nonequilibrium fluids*, Phys. Rev. Lett. 107 (2011), 175702, no. 17, DOI: 10.1103/PhysRevLett.107.175702 © 2011 by the American Physical Society.)

[224] that shows a maximum at  $r_0\sqrt{2}$ , where  $r_0$  is the radius corresponding to the main minimum of the potential. Such a maximum in the interaction potential is expected to suppress crystallization to the close-packed structures fcc and hcp [225], whereas the multiple minima also found are expected to lead to coexisting disordered structures [226]. By combining the results available for various potentials (LJ [219], HS [220], and the PFC potentials [28, 35]), it appears that a repulsive core suffices for the appearance of a disordered precursor, whereas the peak at  $r_0\sqrt{2}$  correlates with the observed suppression of fcc and hcp structures, while the coexistence of the liquid and amorphous phases seen here can be associated with multiple minima of the interaction potential.

3D studies, performed for bcc crystal nucleation in molten pure Fe in the framework of the EOF-PFC model [28, 33], lead to similar results, however, still with diffusive dynamics. In these simulations, the initial density of the liquid has been increased until the solidification started – a procedure that has led to an extreme compression owing to the small size and short time accessible for the simulations. While this raises some doubts regarding the validity of the applied approximations, the behaviour observed for the EOF-PFC Fe is fully consistent with the results obtained for the 1M-PFC model: with increasing driving force first an amorphous precursor nucleates and the bcc phase appears inside these amorphous regions [28, 33]. At higher driving forces the amorphous precursor appears nearly homogeneously in space and the bcc phase nucleates into it later. Apparently, direct nucleation of the bcc phase from the liquid phase requires a longer time than via the amorphous precursor, suggesting that the appearance of the bcc phase is assisted by the presence of the amorphous phase and in line with recent predictions by DFT [219] and atomistic simulations [220]. Remarkably, the interaction potential evaluated for Fe from the pair-correlation function of the amorphous structure is oscillatory and is qualitatively similar to the ones evaluated from experimental liquid structures [227].

**5.1.1.2. Heterogeneous nucleation.** Prieler et al. [137] have explored crystal nucleation on an unstructured hard wall in an anisotropic version of the 1M-PFC

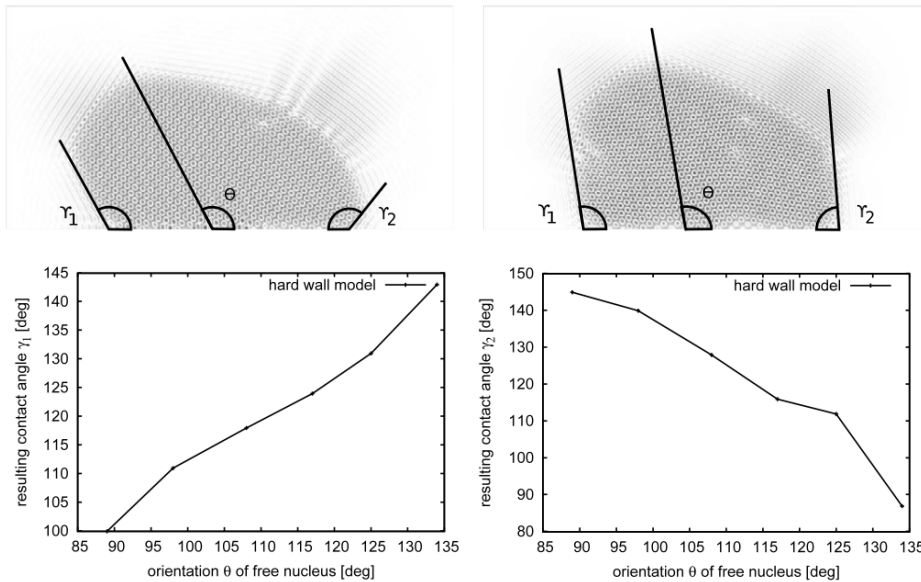


Figure 41. Heterogeneous nuclei formed on a hard wall in the APFC model proposed in reference [137] and the dependence of the left and right side contact angle ( $\gamma_1$  and  $\gamma_2$ , respectively) on the crystal orientation. (Reproduced from R. Prieler, J. Hubert, D. Li, B. Verleye, R. Haberkern, and H. Emmerich, *An anisotropic phase-field crystal model for heterogeneous nucleation of ellipsoidal colloids*, *J. Phys.: Condens. Matter* 21 (2009), 464110, no. 46, DOI: 10.1088/0953-8984/21/46/464110 © 2009 by Institute of Physics Publishing.)

model, in which the particles are assumed to have an ellipsoidal shape. In particular, they have investigated how the contact angle depends on the orientation of the ellipsoids and the strength of the wall potential (see figure 41). A complex behaviour has been observed for the orientational dependence, while increasing the strength of the wall potential reduced the contact angle.

Gránásy et al. [136] have studied crystal nucleation in an rectangular corner of structured and unstructured substrates within the 1M-PFC model in two spatial dimensions. Despite expectations based on the classical theory of heterogeneous nucleation and conventional PF simulations [228], which predict that a corner should be a preferred nucleation site, in the atomistic approach such a corner is not a preferable site for the nucleation of the triangular crystal structure (see figure 42) owing to the misfit of the triangular crystal structure with a rectangular corner. Crystals of different orientation nucleate on the two substrate surfaces, which inevitably leads to the formation of a grain boundary starting from the corner when the two orientations meet. The energy cost of forming the grain boundary makes the rectangular corner an unfavoured place for nucleation. In contrast, a  $60^\circ$  corner helps the nucleation of the triangular phase.

### 5.1.2. Pattern formation in colloidal crystal aggregation

**5.1.2.1. Colloid patterns in two dimensions.** Choosing a large value for the parameter  $\epsilon$  where the liquid-solid interface is faceted, Tegze et al. [38, 39] have investigated solidification morphologies as a function of the thermodynamic driving force. It has been found that the diffusion-controlled growth mode observed at low driving forces and characterized by faceted interfaces changes to a diffusionless growth mode of a diffuse liquid-solid interface that produces a crystal, whose density is comparable to the density of the liquid due to quenched-in vacancies (see section 4.3.5). These two modes have already been observed experimentally in colloidal systems [229]. It has been shown that the two modes can coexist and lead to a new branching mechanism that differs from the usual diffusional instability



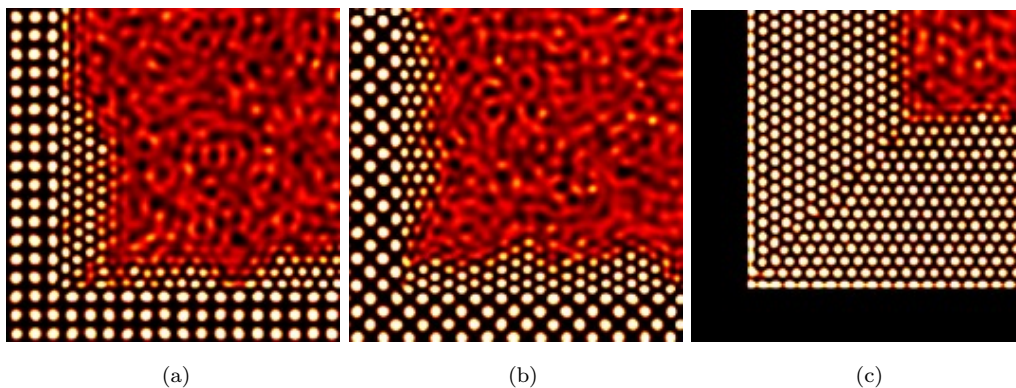


Figure 42. Heterogeneous nucleation in rectangular inner corners of the 1M-PFC model in two spatial dimensions [33]. (a) Nucleation on (01) surfaces of a square lattice (ratio of lattice constant of substrate to inter-particle distance  $a_0/\sigma \approx 1.39$ ). (b) Nucleation on (11) surfaces of a square lattice. (c) Nucleation on an unstructured substrate. Notice the frustration at the corner and the formation of a grain boundary starting from the corner at later stages. (Reproduced from L. Gránásy, G. Tegze, G. I. Tóth, and T. Pusztai, *Phase-field crystal modelling of crystal nucleation, heteroepitaxy and patterning*, *Philos. Mag.* 91 (2011), 123-149, no. 1, DOI: 10.1080/14786435.2010.487476 © 2011 by Taylor & Francis.)

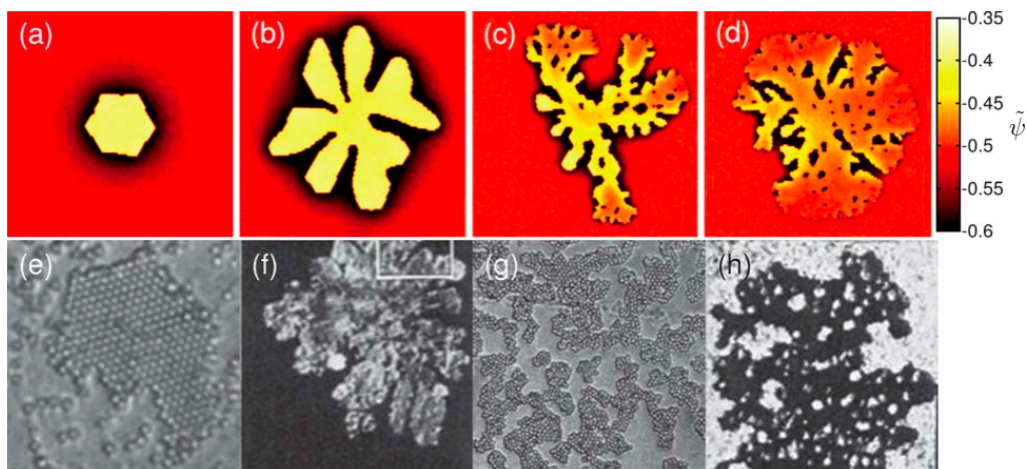


Figure 43. Single crystal growth morphologies (a)-(d) in the 1M-PFC model [38] (top) and experiment (bottom) (e)-(h): 2D colloid crystals by Skjeltorp. (Reproduced with permission from A. T. Skjeltorp, *Visualization and characterization of colloidal growth from ramified to faceted structures*, *Phys. Rev. Lett.* 58 (1987), 1444-1447, no. 14, DOI: 10.1103/PhysRevLett.58.1444 © 1987 by the American Physical Society.) The driving force increases from left to right. In the case of the simulations, the coarse-grained particle density map is shown. The fractal dimensions of the single crystal aggregates evaluated from the slope of the plot  $\log(N)$  vs.  $\log(R_g)$  ( $N$  is the number of particles in the cluster and  $R_g$  is its radius of gyration) are: (a)  $f_d = 2.012 \pm 0.3\%$ , (b)  $1.967 \pm 0.3\%$ , (c)  $1.536 \pm 0.9\%$ , (d)  $1.895 \pm 0.3\%$ . The fast growth mode is recognizable via the lack of a (dark) depletion zone at the interface, whose presence is indicative to the slow mode. A  $2048 \times 2048$  rectangular grid corresponding to  $\approx 13000$  particles, or  $118 \mu\text{m} \times 118 \mu\text{m}$  (assuming  $1.1 \mu\text{m}$  particles) has been used – a size comparable to that shown by the experimental images. (Reproduced from G. Tegze, L. Gránásy, G. I. Tóth, J. F. Douglas, and T. Pusztai, *Tuning the structure of nonequilibrium soft materials by varying the thermodynamic driving force for crystal ordering*, *Soft Matter* 7 (2011), 1789-1799, no. 5, DOI: 10.1039/c0sm00944j © 2011 by Royal Society of Chemistry Publishing.)

driven branching by which dendritic structures form. This new mechanism explains the fractal-like and porous growth morphologies [230] observed in 2D colloidal systems (see figure 43) and may be relevant for the diffusion-controlled to diffusionless transition of crystallization in organic glasses.

**5.1.2.2. Colloid patterns in three dimensions.** Tóth et al. [28] have demonstrated first that owing to the conservative dynamics, the EOM of the 1M-PFC model realizes, dendritic growth forms of bcc and fcc structure evolve in the single-component theory. Tegze [29] and Gránásy et al. [231] have shown by simulations

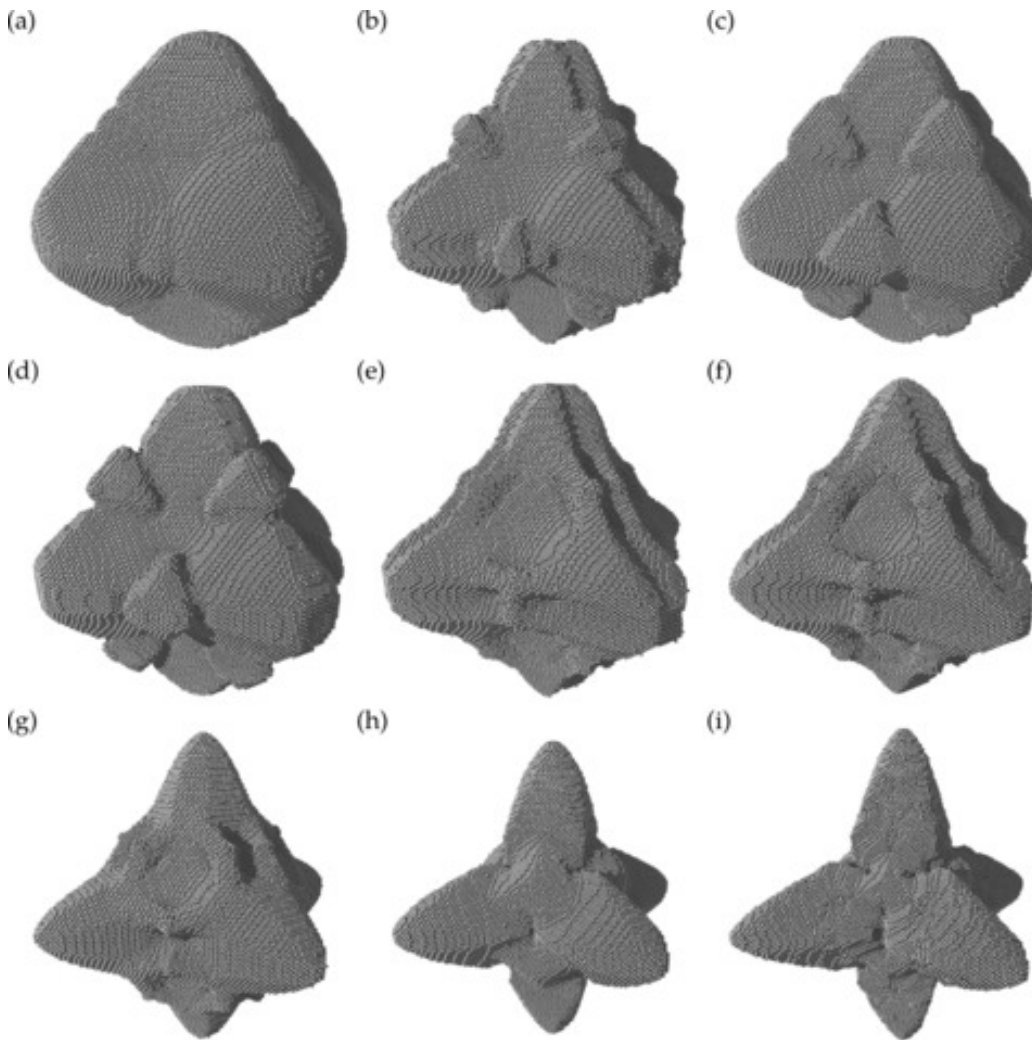


Figure 44. 3D crystal growth morphologies grown from a bcc seed in the single-component 1M-PFC model at  $\epsilon = 0.3748$  in a system containing about  $3 \times 10^6$  colloidal particles [29]. The initial fluid density decreases as (a)  $\psi_0 = -0.015$ , (b)  $-0.0175$ , (c)  $-0.01875$ , (d)  $-0.02$ , (e)  $-0.02062$ , (f)  $-0.0225$ , (g)  $-0.025$ , (h)  $-0.03$ , (i)  $-0.0325$ . The simulations have been performed on a  $1024 \times 1024 \times 1024$  grid. Assuming  $1 \mu\text{m}$  diameter for the particles, the linear size of the simulation box is  $\approx 0.16 \text{ mm}$  – comparable to the smaller colloidal dendrites seen in microgravity experiments [233]. (Reproduced from G. Tegze, *Application of atomistic phase-field methods to complex solidification problems*, PhD Thesis, Eötvös University, Budapest, Hungary (2009).)

containing  $\approx 3 \times 10^6$  particles that due to a kinetic roughening of the crystal-liquid interface that leads to interface broadening, a transition can be seen from faceted dendrites to compact rounded crystals (see figure 44) – a phenomenon reported earlier in experiments for dendritic growth of  $\text{NH}_4\text{Br}$  crystals [232]. Notice that such a kinetic effect cannot be easily incorporated into conventional PF models. Remarkably, as pointed out in reference [28], assuming a micrometer diameter for the “atoms”, these dendritic structures are comparable in size to those formed in colloid experiments in microgravity [233]. This is a unique situation indeed: an “atomistic” theory works here on the size scale of experimental dendrites.

In a recent work, Tang et al. [30] have performed a geometric analysis of bcc and fcc dendrites grown in the respective stability domains of the 1M-PFC model, and evaluated dynamic exponents characterizing dendritic growth in the (100), (110), and (111) directions. They associate the relatively large values obtained for the stability constant from the geometry of the dendrite tip with the faceted morphology of the crystals.

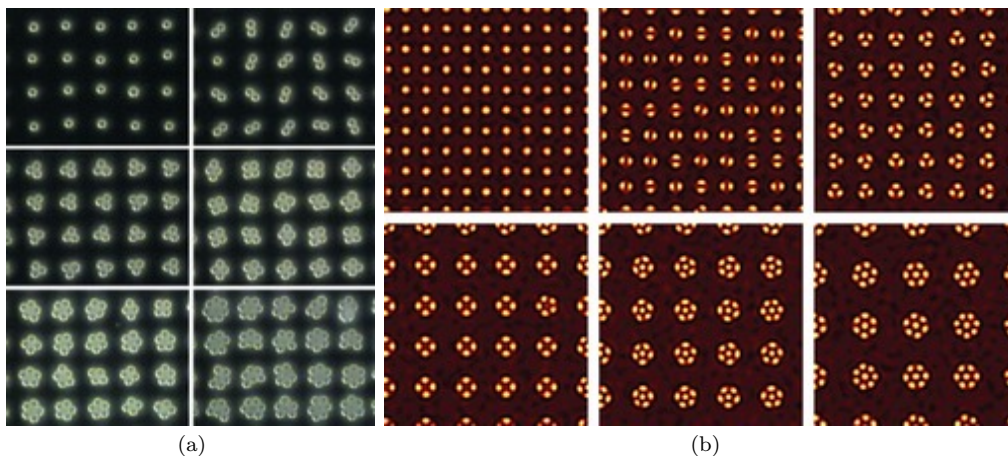


Figure 45. (a) Single and multiple occupation of a chemically patterned periodic substrate by colloidal particles as a function of increasing patch size in the experiments. (Reproduced with permission from I. Lee, H. Zheng, M. F. Rubner, and P. T. Hammond, *Controlled cluster size in patterned particle arrays via directed adsorption on confined surfaces*, *Adv. Mater.* 14 (2002), 572-577, no. 8, DOI: 10.1002/1521-4095(20020418)14:8<572::AID-ADMA572>3.0.CO;2-B © 2002 by Wiley.) (b) 1M-PFC simulations [33] with increasing diameter of circular attractive potential wells. Reduced particle density maps are shown. The ratio of the potential well diameters relative to the single occupation case has been 1, 1.25, 1.5, 2, 2.13, and 2.5. (Reproduced from L. Gránásy, G. Tegze, G. I. Tóth, and T. Pusztai, *Phase-field crystal modelling of crystal nucleation, heteroepitaxy and patterning*, *Philos. Mag.* 91 (2011), 123-149, no. 1, DOI: 10.1080/14786435.2010.487476 © 2011 by Taylor & Francis.)

### 5.1.3. Colloid patterning

Colloid patterning under the influence of periodic substrates can be realized via creating patches that are chemically attractive to the colloidal particles [234]. Depending on the size of the patches single, double, triple, etc., occupations of the patches are possible (see figure 45), whereas the distance of the patches may lead to the formation of various ordered patterns, as predicted by Langevin simulations, in which the patterned substrate is represented by appropriate periodic potentials [235]. Gránásy et al. [33] has employed a 1M-PFC model supplemented with a periodic potential of circular potential wells arranged on a square lattice, to reproduce the patterns seen in the experiments (see figure 45). Another problem, exemplifying the abilities of PFC simulations in modelling colloid patterning, is colloidal self-assembly under the effect of capillary-immersion forces acting on the colloid particles in thin liquid layers due to capillarity and a periodically varying depth of the liquid layer due to a wavy substrate surface. Experiments of this kind have been used to produce single and double particle chains [236] and the otherwise unfavourable square-lattice structure [237]. The capillary-immersion forces can often be well represented by a potential of the form  $U = u_1 \cos(kx)$ , where  $u_1$  is a constant,  $k = 2\pi/\lambda$ , and  $\lambda$  the wavelength of the periodic potential. Setting  $\lambda = \sigma/\sqrt{2}$ , where  $\sigma$  is the interparticle distance, and varying the orientation of the grooves relative to the crystallization (drying) front, patterns seen in the experiments [237] are observed to form in the 1M-PFC model: for grooves parallel to the front, a frustrated triangular structure of randomly alternating double and triple layers appears. For grooves perpendicular to the front, the particles align themselves on a square lattice with the (11) orientation lying in the interface, while for a  $\pi/4$  declination of the grooves the same structure forms, however, now with the (10) face lying in the front. Using larger wavelengths for the potential and adding a weak transversal modulation, while starting from a homogeneous initial particle density, nucleation and growth of wavy single and double chains resembling closely to the experiments [236] are seen [33] (see figure 46).

Epitaxial growth on the (100) surface of a sc substrate has been investigated in 3D using the 1M-PFC model by Tegze et al. [42]. The lattice constant  $a_s$  of the

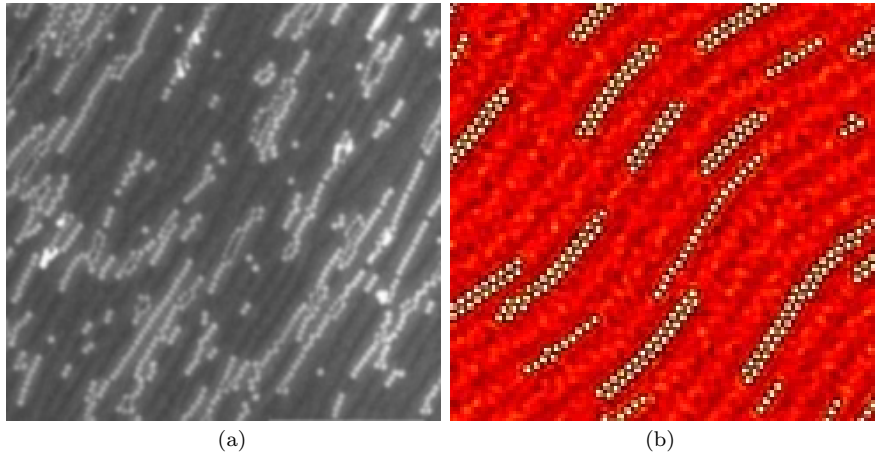


Figure 46. Patterning in experiment vs. 1M-PFC simulation: (a) single and double particle chains evolving in experiment due to capillary-immersion forces on the surface of a rippled substrate. (Reproduced with permission from A. Mathur, A.-D. Brown, and J. Erlebacher, *Self-ordering of colloidal particles in shallow nanoscale surface corrugations*, *Langmuir* 22 (2006), 582-589, no. 2, DOI: 10.1021/la0520379 © 2006 by the American Chemical Society.) (b) The particle chains forming in the 1M-PFC simulation performed with a tilted and wavy version of the potential described in the text [33]. Only a fraction of the reduced particle density map is shown. (Reproduced from L. Gránásy, G. Tegze, G. I. Tóth, and T. Pusztai, *Phase-field crystal modelling of crystal nucleation, heteroepitaxy and patterning*, *Philos. Mag.* 91 (2011), 123-149, no. 1, DOI: 10.1080/14786435.2010.487476 © 2011 by Taylor & Francis.)

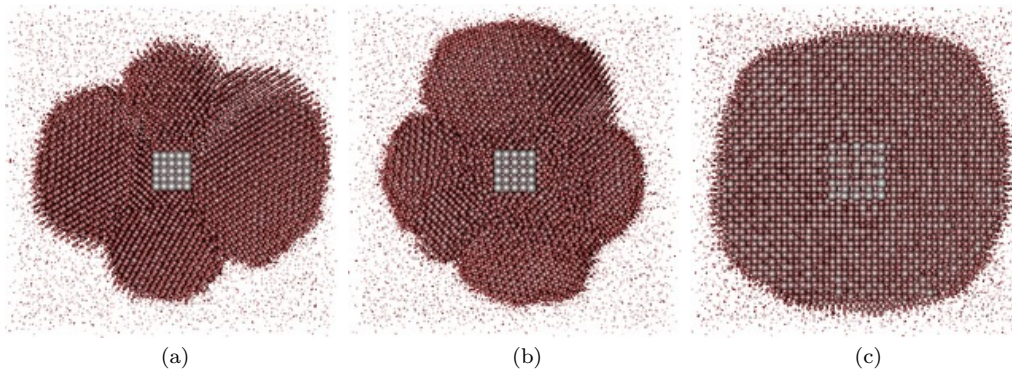


Figure 47. In-plane snapshot of crystalline aggregates grown on  $5 \times 5$  square-lattice templates of  $a_s/\sigma_{\text{fcc}} = 1.0, 1.1547, \text{ and } 1.56$  in 3D as predicted by 1M-PFC simulations [240]. Here,  $\sigma_{\text{fcc}} = 1.056$ . A  $256 \times 256 \times 128$  grid has been used. The visualization is as in figure 25.

substrate has been varied in a range that incorporates the interatomic distance of the bulk fcc structure and the lattice constant of the bulk bcc phase, where the (100) face of the sc structure is commensurable with the (100) faces of the bulk fcc and bcc structures, respectively. A bct structure has grown, whose axial ratio  $c/a$  varies continuously with the lattice constant of the substrate, where  $c$  and  $a$  are the lattice constants of the bct structure perpendicular and parallel to the surface of the substrate, respectively. At the matching values of  $a_s$ , fcc and bcc structures have been observed respectively, as observed in colloid patterning experiments [238]. Analogous results have been obtained for the (100) face of an fcc substrate using 1M-PFC simulations, however, for large lattice mismatch amorphous phase mediated bcc nucleation has been seen [140].

Optical tweezers are used widely to realize 2D periodic templates for influencing colloidal crystal aggregation in 3D [239]. Such templates, depending on the mismatch to the crystalline structure evolving, may instigate the formation of single-crystal or polycrystalline structures [240]. Growth textures, obtained when supplementing the 1M-PFC model with a  $5 \times 5$  flat square-lattice template (realized by a periodic potential term), show remarkable resemblance to the experiments (see figure 47) [241].

## 5.2. Applications to polymers

In the field of soft matter simulations the study of polymers plays an important role. Understanding the relation between the statistical physics on the molecular scale and the resulting material properties is of great relevance with respect to principal questions, chemical and pharmaceutical applications, as well as the study of biopolymers in living cells. The investigation of polymer systems and the development of new polymer materials and composites with specific properties depend essentially on suitable numerical and simulation techniques. One of the big challenges is closing the gap between the atomistic and the microscale. Furthermore, in many polymer systems structures develop rather slowly and on very different length scales. Since particle-based simulations are strongly restricted, especially regarding the time scale, there is the demand for continuum models such as PF and PFC theories.

Polymer systems are studied in various systems, in the form of polymer solutions and melts, in hydrogels, in glasses, and in polymer crystals. A principle problem of continuum models for polymers is the connectivity of the chains, which leads to long-ranging interactions between spatially separated atoms of the same polymer chain and, due to entanglements, also between atoms of different chains. For an implementation of these effects into continuum theories, appropriate simplifications are necessary.

One major continuum method for polymer systems is the self-consistent field (SCF) theory. Starting from an equilibrium theory, it has been extended in order to study dynamic systems. It is therefore interesting to compare the SCF theory with the PF method, which, during the last years, has increasingly been applied on polymer systems, and the PFC method, which is suited for studying pronounced periodic structures in polymers. In this context, we will also elucidate the relation between the PF and the PFC method, especially for the case of polymer systems.

In many applications of polymers, the structure and dynamics of the system are sensitive to various parameters like temperature, flow velocity, velocity gradients, gravity or stresses. In polyelectrolytes, also charge densities, ion concentrations, the pH value, and external fields need to be considered. Several of these aspects have been taken into account in PF calculations, as we will demonstrate for some examples. We begin with a description of the SCF theory, after which we discuss the PF and the PFC approaches to polymer systems.

### 5.2.1. Self-consistent field theory for polymer systems

In general, the SCF theory is a molecular-based, approximate description of many-body systems. For polymer blends, it has originally been developed to describe equilibrium systems [242, 243]. Later it was extended to dynamic self-consistent field (DSCF) theory, which allows investigating dynamic processes (for an review see reference [244]).

The SCF method is used to study fluctuations, pattern formation, and segregation in various kinds of polymer mixtures (see references [244–247] and references therein). In many works, the method is applied on a mixture of different types of homopolymers or block copolymers built of two types of monomers A and B. In most cases, it is assumed that the polymer chains have a Gaussian distribution. This means that the polymer path is distributed like a random walk and corresponds to the situation where the persistence length is much smaller than the polymer length. It should be mentioned that one can also use semiflexible, worm-like polymers instead [245]. Assuming an incompressible polymer melt, the total polymer density  $\varphi_0$  is fixed. The canonical partition function can be written as

[245]

$$\mathcal{Z} \approx \int \prod_i \delta \mathbf{r}_i P(\mathbf{r}_i) \exp\left(-\frac{\mathcal{F}_{\text{FH}}}{k_{\text{B}}T}\right) \delta(\varphi_{\text{A}} + \varphi_{\text{B}} - \varphi_0) \quad (119)$$

Here,  $\int \delta \mathbf{r}_i P(\mathbf{r}_i)$  is a path integral of a polymer weighted by the Gaussian distribution  $P(\mathbf{r}_i)$  and  $\mathcal{F}_{\text{FH}}$  is the Flory-Huggins free energy for polymers, which favours adjacent monomers of the same type: A-A and B-B. The delta function generates the incompressibility. The problematic parts of  $\mathcal{Z}$  in equation (119) are the polymer-polymer interactions (the steric and the Flory-Huggins interactions). They are avoided by rewriting  $\mathcal{Z}$  in a form in which single polymers are subject to auxiliary fields that represent the effect of the other polymers. For the system with monomers A and B, two auxiliary fields  $V$  and  $W$  are introduced, where  $V$  is conjugated to the total density  $\varphi_{\text{A}} + \varphi_{\text{B}}$ , while  $W$  is conjugated to the composition  $\varphi_{\text{A}} - \varphi_{\text{B}}$ . Auxiliary fields are an essential concept of all SCF theories. The canonical partition function  $\mathcal{Z}$  can now be written as

$$\mathcal{Z} \approx \int \delta V \delta W \exp\left(-\frac{\mathcal{H}(V, W)}{k_{\text{B}}T}\right), \quad (120)$$

where the Hamiltonian  $\mathcal{H}(V, W)$  is determined by the partition functions  $\mathcal{Z}_{\text{sp}}$  of single polymers in the presence of the auxiliary fields. The partition functions can be calculated with the help of propagator functions. The propagator functions are the solution of diffusion equations [243], which depend on  $V$  and  $W$ . Equation (120) is still equivalent to equation (119), but the expression is much simpler.

**5.2.1.1. Equilibrium SCF theory.** In principle, one can use equation (120) to extract equilibrium values of the average concentration  $\langle \varphi_{\text{A}} \rangle$  (and thus of  $\langle \varphi_{\text{B}} \rangle = \varphi_0 - \langle \varphi_{\text{A}} \rangle$ ) and fluctuation terms. In fact, in some cases, this has been done numerically with the help of “field MC” simulations [248] or complex Langevin simulations [249]. However, for most systems the numerical cost for treating expression (119) with fully fluctuating auxiliary fields  $V$  and  $W$  is extremely high. The problem can be simplified with the help of a saddle-point approximation: instead of integrating over the whole  $V$  and  $W$  space, one determines the minimum of the Hamiltonian  $\mathcal{H}$  with respect to  $V$  and  $W$ ,

$$\frac{\partial \mathcal{H}(V^*, W^*)}{\partial V} = \frac{\partial \mathcal{H}(V^*, W^*)}{\partial W} = 0, \quad (121)$$

which provides saddle-point fields  $V^*$  and  $W^*$  for given concentration fields  $\varphi_{\text{A}}$  and  $\varphi_{\text{B}}$ . In turn, the concentration fields can be calculated from the partition function by solving the diffusion equation that depends on  $V^*$  and  $W^*$ . Thus, the problem can be solved self-consistently by iterating the calculation of concentration and auxiliary fields [250]. This is the basic principle of the SCF theory. In this form, it enables calculation of equilibrium properties of concentration fields, including microphase separation and global phase separation for polymer blends including homopolymers and block copolymers. A more precise description is given by the external potential theory, which allows fluctuations of the composition field  $W$  [251].

**5.2.1.2. Dynamic SCF theory.** The dynamic self-consistent field theory (DSCF) is an extension of the SCF theory that allows to study nonequilibrium polymer blends. For an incompressible fluid, the saddle point values  $V^*$  and  $W^*$  are determined by  $\varphi_A$  so that we can define the energy functional

$$\mathcal{F}[\varphi_A] = \mathcal{H}(V^*(\varphi_A), W^*(\varphi_A)) . \quad (122)$$

The dynamics of  $\varphi_A$  is described by a Langevin equation

$$\frac{\partial \varphi_A(\mathbf{r}, t)}{\partial t} = -\nabla_{\mathbf{r}} \cdot \mathbf{J}_{\varphi}(\mathbf{r}, t) + \zeta(\mathbf{r}, t) \quad (123)$$

with a flux density  $\mathbf{J}_{\varphi}(\mathbf{r}, t)$  and a Gaussian random noise term  $\zeta(\mathbf{r}, t)$ . The flux density is given by

$$\mathbf{J}_{\varphi} = \int d\mathbf{r}' \Lambda_{\varphi}(\mathbf{r}, \mathbf{r}') \nabla_{\mathbf{r}'} \frac{\delta \mathcal{F}}{\delta \varphi_A(\mathbf{r}', t)} \quad (124)$$

with an Onsager coefficient  $\Lambda_{\varphi}(\mathbf{r}, \mathbf{r}')$ , which is in general nonlocal, due to the forces that propagate along the polymer backbone. Nonlocal effects can be considered with the Rouse model [252] or the reptation model [72]. In the simplest case, the interactions due to the chain connectivity are neglected and a local Onsager coefficient  $\Lambda_{\varphi}(\mathbf{r}, \mathbf{r}') = k \varphi_A(\mathbf{r}, t) \varphi_B(\mathbf{r}, t) \delta(\mathbf{r} - \mathbf{r}')$  with a constant  $k$  is used [26, 85], leading to

$$\frac{\partial \varphi_A}{\partial t} = -k \nabla_{\mathbf{r}} \cdot \left( \varphi_A (\varphi_0 - \varphi_A) \nabla_{\mathbf{r}} \frac{\delta \mathcal{F}}{\delta \varphi_A} \right) + \zeta . \quad (125)$$

Notice that  $\mathcal{F}$  still includes the auxiliary fields and each propagation in time requires the iterative calculation of these fields. In the random phase approximation, which is valid for suitably small fluctuations, one can derive an approximate expression for  $\mathcal{F}$ , which has the form of a Ginzburg-Landau free energy [245],

$$\mathcal{F}_{\text{GL}} = \int d\mathbf{r} \left( f_{\text{FH}}(\varphi_A) + b(\nabla_{\mathbf{r}} \psi)^2 \right) , \quad (126)$$

with the Flory-Huggins free-energy density  $f_{\text{FH}}(\varphi_A)$  and the parameter  $b$ .

In analogy to DSCF, a dynamic version of the external potential (DEP) method can be applied. The DSCF method and the DEP theory have been used to study spinodal decomposition. A quantitative comparison with Monte-Carlo (MC) simulations shows a distinctly higher accuracy of the DEP method [253]. The DSCF has been combined with the NS equation and a convection term has been added to the Langevin equation [254–256].

## 5.2.2. Phase-field methods for polymer systems

**5.2.2.1. Conventional phase-field models.** In recent years, there has been a growing number of articles that apply the PF method to polymer systems, i. e., to systems in which at least one phase is a polymer melt or a polymer solution (see, for example, references [257–261]). Here, the PF method is used to describe the nonequilibrium dynamics of phase boundaries. The method is based on a free-

energy functional of a phase variable  $\psi(\mathbf{r})$ , which has the form [24]

$$\mathcal{F} = \int d\mathbf{r} (f(\psi) + f_{\text{inh}}(\nabla_{\mathbf{r}}\psi)), \quad (127)$$

where  $f$  is the free-energy density of the bulk – usually an asymmetric double-well potential. The second part considers spatial inhomogeneities. A simple example of the free energy in equation (127) is the standard Ginzburg-Landau free energy

$$\mathcal{F} = \int d\mathbf{r} \left( a(\psi^2 - \psi_0^2)^2 + b(\nabla_{\mathbf{r}}\psi)^2 \right) \quad (128)$$

with coefficients  $a$  and  $b$ . If  $\psi$  is conserved, then the dynamics is described by a Cahn-Hilliard (CH) equation [262]:

$$\frac{\partial\psi}{\partial t} = -\nabla_{\mathbf{r}} \cdot \mathbf{J}. \quad (129)$$

Here, the flux density is given by

$$\mathbf{J} = -M \nabla_{\mathbf{r}} \frac{\delta\mathcal{F}}{\delta\psi} \quad (130)$$

with a mobility  $M$ , which in general may depend on  $\psi$ .

**5.2.2.2. Polymer liquids.** In a fluid polymer blend,  $\psi$  is often taken as the concentration of one component and the bulk free-energy density  $f(\mathbf{r})$  is the Margules activity from the Flory-Huggins theory [263, 264]. In many cases, a Gaussian noise term  $\zeta(\mathbf{r}, t)$  is added to the CH equation so that the equation has a Langevin form

$$\frac{\partial\psi}{\partial t} = -\nabla_{\mathbf{r}} \cdot \mathbf{J} + \zeta = \nabla_{\mathbf{r}} \cdot \left( M \nabla_{\mathbf{r}} \frac{\delta\mathcal{F}}{\delta\psi} \right) + \zeta. \quad (131)$$

Notice the similarity to equation (123) from SCF theory. The expressions differ in the free-energy functional  $\mathcal{F}$ , which includes the auxiliary fields in the SCF theory. Considering a flow velocity  $\mathbf{v}$ , equation (131) can be extended to the convective CH equation with a noise term [265]:

$$\frac{\partial\psi}{\partial t} + \mathbf{v} \cdot \nabla_{\mathbf{r}} \psi = \nabla_{\mathbf{r}}^2 \frac{\delta\mathcal{F}}{\delta\psi} + \zeta. \quad (132)$$

Fluid dynamics is described by a continuity equation and an extended NS equation, which can generally be written as

$$\rho \left( \frac{\partial}{\partial t} + \mathbf{v} \cdot \nabla_{\mathbf{r}} \right) \mathbf{v} = -\nabla_{\mathbf{r}} p + 2\nabla_{\mathbf{r}} \cdot \hat{\boldsymbol{\mu}}_{\text{visc}} + \mathbf{k}_{\text{surf}} + \mathbf{k}_{\text{ext}} + \mathbf{k}_{\text{elast}}, \quad (133)$$

where  $\rho$  is the mass density,  $p$  is the pressure,  $\hat{\boldsymbol{\mu}}_{\text{visc}}$  is the viscous stress tensor, and  $\mathbf{k}_{\text{surf}}$  considers the surface tension from the interfaces [259]. The term  $\mathbf{k}_{\text{ext}}$  represents external forces like gravity, while  $\mathbf{k}_{\text{elast}} \propto (r_0^{-2} \langle \mathbf{r} \mathbf{r} \rangle - \mathbf{1})$  with an appropriate length scale  $r_0$  denotes the elastic response of polymers to a flow field leading to viscoelastic behaviour [266]. An alternative description of viscoelasticity is the Oldroyd-B model [267], which has been used together with the PF method



to study the elongation and burst of viscoelastic droplets [268] and the coalescence of polymer drops and interfaces [261, 269].

The connection of the CH and the NS equation is called “model H” in the nomenclature of Hohenberg and Halperin [1]. In many cases, the term  $\mathbf{k}_{\text{elast}}$  is neglected so that the polymer phase is described as a Newtonian fluid. In principle, all terms on the right-hand-side (besides  $p$ ) can be coupled to the PF variable  $\psi$ , since the involved material parameters may depend on the composition. Model H has been used to study spinodal decomposition with and without external velocity fields and Rayleigh-Taylor instabilities [257, 259, 270]. The described method with a slightly different CH free energy has been used to study the shape of fluid films on a dewetting substrate [271].

**5.2.2.3. Polymer crystals.** Another important topic is the growth of polymer crystals in a polymer melt or solution [260, 272, 273]. So far, polymer crystals have not been studied explicitly with the help of the PFC method. Polymer crystallization has been investigated with the standard PF method, in which the extension of the crystalline phase is characterized by a phase field  $\psi$ , while the crystalline structure is not considered. The dynamics of the crystal growth is described with the Allen-Cahn equation [274]

$$\frac{\partial \psi}{\partial t} = -\Gamma \frac{\delta \mathcal{F}}{\delta \psi}, \quad (134)$$

where  $\mathcal{F}$  again consists of a bulk free-energy density and a gradient term. Frequently, the heat transport is taken into account by a heat transfer equation with an extra term considering the production of latent heat at the crystal growth front [260, 273]. In various cases, two PF variables  $\psi_{\text{mat}}$  and  $\psi_{\text{cryst}}$  are used to represent the concentration (or relative concentration) and the crystallization. This way the system is investigated with model C PF equations [258, 275]. By adding flow equations, a heat equation, and external fields, like an electrical field [258], a wide range of multiphase polymer systems can be studied.

**5.2.2.4. Hydrogels.** The PF method has also been applied to hydrogels [265], where the calculations consider free ions and charges fixed to the polymer network. The connectivity of the polymer network results in a shape elasticity as the hydrogel is swollen. This model is used to study the swelling of the hydrogel as the ion concentration in the surrounding is changed. Its PF variable  $\psi(\mathbf{r}, t)$  changes continuously (and monotonously) from  $\psi \cong 0$  in the surrounding bath to  $\psi \cong 1$  in the hydrogel region. The dynamics of  $\psi(\mathbf{r}, t)$  is described by

$$\frac{\partial \psi}{\partial t} = -M_{\psi} \left( h'(\psi) \left( \mu \varepsilon_{ij}^2 + \frac{\lambda - \tilde{\lambda}}{2} \varepsilon_{kk}^2 - (p - p_{\text{eq}}) \right) + \frac{W}{V_{\text{m}}} g'(\psi) - K_{\psi} \nabla_{\mathbf{r}}^2 \psi \right), \quad (135)$$

corresponding to equation (134), where  $M_{\psi}$  is a mobility. Here, the term

$$\mu \varepsilon_{ij}^2 + \frac{\lambda - \tilde{\lambda}}{2} \varepsilon_{kk}^2 - (p - p_{\text{eq}}) \quad (136)$$

is the driving force for the phase field that depends on the osmotic pressure  $p$  and the elasticity of the hydrogel, which is given by the shear modulus  $\mu$ , and the difference  $\lambda - \tilde{\lambda}$  of the Lamé constants inside and outside the hydrogel. The

deformation of the hydrogel is described by the strain

$$\varepsilon_{ij} = \frac{1}{2} \left( \frac{\partial v_i}{\partial r_j} + \frac{\partial v_j}{\partial r_i} \right) \quad (137)$$

and the osmotic pressure at equilibrium is denoted by  $p_{\text{eq}}$ . The function  $h(\psi) = \psi^2(3 - 2\psi)$  in equation (135) satisfies  $h(0) = 0$  and  $h(1) = 1$ . Its derivative  $h'(\psi) = dh/d\psi$  vanishes at  $\psi = 0$  and  $\psi = 1$  so that the first term in equation (135) contributes only at the interface between hydrogel and bath. In the second term, the quantities  $W$  and  $V_m$  denote the potential height and the molar volume of the mixture, respectively, and the function  $g(\psi) = \psi^2(1 - \psi^2)$  provides a double-well potential with minima at the bulk phases. Finally, the parameter  $K_\psi$  controls the diffusion of the phase field. The sum of the second and the third term in equation (135) is the functional derivative of the free-energy functional in equation (128), if we set  $\psi \rightarrow \psi - 1/2$ ,  $\psi_0 = 1/2$ ,  $a = W/V_m$ , and  $b = K_\psi/2$ .

Assuming suitably slow swelling dynamics, mechanical equilibrium provides a relation between strain  $\varepsilon_{ij}$  and pressure  $p$ :

$$\frac{\partial}{\partial x_j} \left( h(\psi)(2\mu\varepsilon_{ij} + \lambda\varepsilon_{kk}\delta_{ij}) + (1 - h(\psi))\tilde{\lambda}\varepsilon_{kk}\delta_{ij} - h(\psi)(p - p^{\text{eq}})\delta_{ij} \right) = 0. \quad (138)$$

The osmotic pressure is induced by the average concentration difference of free ions inside and outside the hydrogel. If  $c_i$  is the local concentration of type  $i$ , one has

$$\frac{p(t)}{N_A k_B T} = \sum_i N \frac{\int d\mathbf{r} \psi(\mathbf{r}, t) c_i(\mathbf{r}, t)}{\int d\mathbf{r} \psi(\mathbf{r}, t)} - \frac{\int d\mathbf{r} (1 - \psi(\mathbf{r}, t)) c_i(\mathbf{r}, t)}{\int d\mathbf{r} (1 - \psi(\mathbf{r}, t))}. \quad (139)$$

With equations (138) and (139) the first term in equation (135) can be calculated, if the local concentrations  $c_i$  of the ions are known. The time dependence of the ion concentrations is given by the Nernst-Planck equation

$$\frac{\partial c_i}{\partial t} = \nabla_{\mathbf{r}} \cdot \left( D_i \left( \nabla_{\mathbf{r}} c_i + \frac{z_i}{F_r} N_A k_B T c_i \nabla_{\mathbf{r}} U_{\text{el}} \right) \right), \quad (140)$$

where ions of type  $i$  have a concentration  $c_i$ , a diffusion constant  $D_i$  and a valence  $z_i$ . The quantity  $F_r$  is the Faraday constant and the electric potential  $U_{\text{el}}$  is given by the Poisson equation

$$\nabla_{\mathbf{r}} \cdot (\varepsilon \nabla_{\mathbf{r}} U_{\text{el}}) + F_r \left( \sum_i z_i c_i + z_f c_f \right) = 0, \quad (141)$$

where  $\varepsilon$  is the absolute permittivity of the medium and the quantities  $c_f$  and  $z_f$  are the concentration and the valence of the fixed charges on the polymer network, respectively. Since the total number of fixed charges does not change, one has

$$c_f(\mathbf{r}, t) = \frac{\psi(\mathbf{r}, t)}{\int d\mathbf{r}' \psi(\mathbf{r}', t)} c_f^{\text{eq}} \int d\mathbf{r}' \psi(\mathbf{r}', t) \quad (142)$$

for the concentration of fixed charges  $c_f$ , which is  $c_f^{\text{eq}}$  at equilibrium. With the help of these equations, the system, consisting of a charged polymer-network in a solvent with ions, has been investigated and the swelling behaviour of the hydrogel has been analysed. This section demonstrates how the PF equation can be coupled with

other equations that control the mechanical, chemical, and electric properties of the system. It shows that short-range interactions at the moving hydrogel-solution interface can be coupled with long-range fields and dynamics.

**5.2.2.5. Phase-field-crystal method for polymer systems.** The connectivity of polymer chains makes it difficult to apply the PFC method on the atomistic structure of polymers. However, PFC models are a useful tool to investigate structure formation on a larger scale. One example is the investigation of density correlations in polymer solvents. This has been done by Praetorius and Voigt, who studied the density profile of a polymer solvent in the vicinity of moving colloids [187]. The model considers soft interactions of polymer coils that flow around spherical colloids. The colloid diameter and the effective polymer diameter are of the same order, leading to pronounced density oscillations in the vicinity of the colloid. The calculations are based on a free-energy functional of the SH-type,

$$\frac{\mathcal{F}[\Psi]}{k_B T} = C \int d\mathbf{r} \left( \frac{\Psi}{2} (-\epsilon + (1 + \nabla_{\mathbf{r}}^2)^2) \Psi + \frac{\Psi^4}{4} + \rho U_1 \right), \quad (143)$$

where the phase field  $\Psi(\mathbf{r}, t) = 2(\rho_0 - \rho(\mathbf{r}, t))$  characterizes the deviation of the local density  $\rho(\mathbf{r}, t)$  from the average density  $\rho_0$ ,  $C = 1/(48\rho_0^4)$ , and  $U_1(\mathbf{r}, t)$  represents the rotationally-symmetric potential inferred by the colloid in units of  $k_B T$ . The free-energy expression is derived analogously for equation (53). The calculation of a polymer solution passing a fixed colloid shows pronounced density modulations around the colloid with pronounced oscillations in the side, where the flow hits the colloid. The example shows that the PFC model can also be used to analyse order in a fluid polymer system.

Typically, the occurrence of structured patterns results from the interplay of competing interactions. In the case of crystals there are typically short-range repulsions on one hand and the external pressure plus attractive forces on the other hand. In various soft matter systems, other types of competing interactions may lead to periodic patterns on a distinctly longer scale. Seul and Andelman have described many pattern formation phenomena with the help of phase modulations with a preferred wavelength [4]. The variety of materials ranges from fluid films of dipolar molecules over ferrofluids to fluid membranes and block copolymers.

We consider a system with two components A and B that tend to demix. The phase variable  $\Psi$  defines the deviation from the homogeneous distribution. A Ginzburg-Landau expansion of the free energy is given by

$$\mathcal{F}_{\Psi} = \mathcal{F}_0[\Psi] + \frac{b}{2} \int d\mathbf{r} (\nabla_{\mathbf{r}} \Psi(\mathbf{r}))^2 = \mathcal{F}_0[\Psi] + \frac{b}{2} \int d\mathbf{k} \tilde{\Psi}(-\mathbf{k}) k^2 \tilde{\Psi}(\mathbf{k}), \quad (144)$$

where  $\tilde{\Psi}(\mathbf{k})$  is the Fourier transform of  $\Psi(\mathbf{r})$ . The bulk contribution  $\mathcal{F}_0[\Psi]$  is typically a Landau free-energy expansion. Without extra interactions,  $\mathcal{F}_{\Psi}$  corresponds to the standard PF model. Now we assume a long-range interaction between molecules at positions  $\mathbf{r}$  and  $\mathbf{r}'$ , which is proportional to a correlation function  $g(\mathbf{r}, \mathbf{r}')$ . This provides an extra free-energy term

$$\mathcal{F}_g = \frac{C_g}{2} \int d\mathbf{r} \int d\mathbf{r}' \Psi(\mathbf{r}) g(\mathbf{r}, \mathbf{r}') \Psi(\mathbf{r}') \quad (145)$$

with a constant  $C_g$ . A simple example, given in reference [4], is a 2D film of molecules A and B, in which molecules A have a dipole moment  $\mu$ . In this case,

one has  $C_g = -\mu^2$  and  $g(\mathbf{r}, \mathbf{r}') = |\mathbf{r} - \mathbf{r}'|^{-3}$  [4]. If  $g(\mathbf{r}, \mathbf{r}') = g(|\mathbf{r} - \mathbf{r}'|)$ , the free energy  $\mathcal{F}_g$  can be expressed as

$$\mathcal{F}_g = \frac{C_g}{2} \int d\mathbf{k} \tilde{\Psi}(-\mathbf{k}) \tilde{g}(k) \tilde{\Psi}(\mathbf{k}), \quad (146)$$

where  $\tilde{g}(k)$  is the 2D Fourier transform of  $g(|\mathbf{r} - \mathbf{r}'|)$ . Combining equations (144) and (146), one has

$$\mathcal{F} = \mathcal{F}_\Psi + \mathcal{F}_g = \mathcal{F}_0 + \int d\mathbf{k} \tilde{\Psi}(-\mathbf{k}) \tilde{g}_c(k) \tilde{\Psi}(\mathbf{k}) \quad (147)$$

with  $\tilde{g}_c(k) = C_g \tilde{g}(k) + bk^2$ . It can be shown that  $\tilde{g}_c(k)$  has a minimum for a finite  $k_m$  and that the system forms a periodic pattern with wave number  $k_m$ .

A free-energy expression like in equation (147) is also found in the Leibler-Ohta-Kawasaki (LOK) theory for AB-block copolymers [276, 277]. The theory allows the investigation of microphase separation providing lamellar, cylindrical, and spherical domains. The theory starts with a model Hamiltonian, which integrates interactions along all pairs of polymers. The ansatz corresponds to that of the SCF theory [243, 278]. As a next step, the LOK theory applies a random-phase approximation (RPA), which leads to an expression for the free energy  $\mathcal{F}[\Psi] = \mathcal{F}_g + \mathcal{F}_{\text{ho}}[\Psi]$ , where  $\mathcal{F}_g$  corresponds to equation (146) with

$$C_g g(\mathbf{r}, \mathbf{r}') = \frac{1}{c} \Gamma(\mathbf{r}, \mathbf{r}') - 2\chi \delta(\mathbf{r} - \mathbf{r}'), \quad (148)$$

and  $\mathcal{F}_{\text{ho}}[\Psi]$  contains higher-order terms of  $\Psi$ . In equation (148),  $\chi$  is the Flory-Huggins parameter. With some approximations, a simple expression for  $\tilde{\Gamma}(\mathbf{k}, \mathbf{k}')$ , which is the Fourier transform of  $\Gamma(\mathbf{r}, \mathbf{r}')$ , is derived [277]. This leads to a free-energy expression of the form

$$\mathcal{F}_g = \frac{1}{2\rho_0 N} \frac{1}{(2\pi)^d} \int d\mathbf{k} \tilde{\Psi}(-\mathbf{k}) \tilde{h}(k) \tilde{\Psi}(\mathbf{k}), \quad (149)$$

with a polymerization degree  $N$ , the average density  $\rho_0$ , and

$$\tilde{h}(k) = \tilde{B}k^2 + \tilde{A}k^{-2} - \tilde{\chi}. \quad (150)$$

Here,  $\tilde{A} = 3/(N\phi^2(1-\phi)^2)$  and  $\tilde{B} = N/(4\phi(1-\phi))$  with  $\phi$  being the fraction of A monomers per polymer. Furthermore,  $\tilde{\chi} = 2\rho_0 N\chi - \tilde{h}_0(\phi)$  with a function  $\tilde{h}_0(\phi)$ . Again, minimization of  $\tilde{g}_c(k)$  provides a preferred wave number  $k_c = (\tilde{A}/\tilde{B})^{1/4}$ , while  $\tilde{\chi}_c = 2(\tilde{A}\tilde{B})^{1/2}$  is the critical value, above which  $\tilde{g}_c(k_c)$  gets negative and the spatially homogeneous distribution gets unstable.

In the vicinity of the critical point,  $\tilde{g}_c(k)$  can be expanded around  $k_c$ , which leads to

$$\mathcal{F}_g = \frac{1}{2\rho_0 N k_c^2} \frac{1}{(2\pi)^d} \int d\mathbf{k} \tilde{\Psi}(-\mathbf{k}) \left( -k_c^2 (\tilde{\chi} - \tilde{\chi}_c) + \tilde{B}(k^2 - k_c^2)^2 \right) + \tilde{\Psi}(\mathbf{k}). \quad (151)$$

Transformed into real space, one has

$$\mathcal{F}_g = \frac{\tilde{B}}{\rho_0 N k_c^2} \int d\mathbf{r} \frac{\Psi(\mathbf{r})}{2} \left( -\frac{k_c^2 (\tilde{\chi} - \tilde{\chi}_c)}{\tilde{B}} + (k_c^2 + \nabla_{\mathbf{r}}^2)^2 \right) \Psi(\mathbf{r}). \quad (152)$$

If we set  $k_0 = k_c$  and  $\beta = k_c^2(\bar{\chi} - \bar{\chi}_c)/\tilde{B}$ , the integrand in equation (152) corresponds to that in the PFC free energy in equation (1), up to a term proportional to  $\Psi^4$ , which is included in  $\mathcal{F}_{\text{ho}}[\Psi]$ . The free energy  $\mathcal{F} = \mathcal{F}_g + \mathcal{F}_{\text{ho}}[\Psi]$  with  $\mathcal{F}_g$  as in equation (152) has already been derived by Leibler. It is only valid in the weak-segregation case close to the critical point.

Tsori and Andelman have investigated a copolymer system in contact with a chemically patterned substrate [279]. Such systems are important for the creation of bulk structures controlled by a surface structure. Considering systems reasonably close to the critical point, the authors have used a bulk free-energy functional of the PFC-type. The interaction with the surface is described by a free-energy functional

$$\mathcal{F}_s = \int d\mathbf{r} (U_s(\mathbf{r})\Psi(\mathbf{r}) + \tau_s\Psi^2(\mathbf{r})) . \quad (153)$$

Here, the surface potential  $U_s(\mathbf{r})$  prefers A monomers in regions with  $U_s(\mathbf{r}) < 0$ . The  $\Psi^2$ -term of  $\mathcal{F}_s$  is a surface correction to the Flory parameter  $\chi$ . Depending on whether the system is below or above the critical point  $\chi_c$ , the bulk phase is either homogeneous or lamellar. In both cases, the surface pattern modulates the bulk phase. The Fourier transformation of the surface pattern shows that Fourier modes with  $k > k_c$  persist only close to the surface, while modes with  $k < k_c$  can propagate over long distances.

In the strong segregation regime, which is present in segregating systems far from the critical point, the LOK theory provides a solution in which the  $k^{-2}$ -term in equation (150) is treated more accurately, leading to

$$\mathcal{F} = \frac{1}{2\rho_0 N} \int d\mathbf{r} \left( \tilde{B}(\nabla_{\mathbf{r}}\Psi)^2 + \bar{\chi}\Psi^2 + \tilde{A} \int d\mathbf{r}' \Psi(\mathbf{r})G(\mathbf{r}, \mathbf{r}')\Psi(\mathbf{r}') \right) + \mathcal{F}_{\text{ho}}[\Psi] , \quad (154)$$

where the Green's function  $G(\mathbf{r}, \mathbf{r}')$  obeys

$$-\nabla_{\mathbf{r}}^2 G(\mathbf{r}, \mathbf{r}') = \delta(\mathbf{r} - \mathbf{r}') . \quad (155)$$

In the strong segregation limit the interfacial regions are small compared to the size of the phase domains. The LOK theory for the strong-segregation limit has been combined with the PF method in order to investigate fluctuations in block copolymer systems [280]. The dynamics of the relative concentration difference is studied with a CH equation as given in equation (129). As the free energy in equation (154) includes long-range interactions explicitly, the method goes beyond the standard PF theory and also beyond the standard PFC method. However, inserting equation (154) into equation (129) provides a rather simple equation, namely

$$M^{-1} \frac{\partial \Psi}{\partial t} = \nabla_{\mathbf{r}}^2 \left( 2\bar{\chi} - \frac{\tilde{B}}{\rho_0 N} \nabla_{\mathbf{r}}^2 \right) \Psi - \frac{\tilde{A}}{\rho_0 N} \Psi , \quad (156)$$

where we have used equation (155) and assumed that  $M$  is constant.

The combination of LOK theory and PF method allows the calculation of statistical and dynamical properties of the diblock copolymer system, down to the length scale of the A-B interface width. In reference [280] the method has been used to investigate fluctuations of the domain boundaries in a periodic structure of alternating A and B layers. The method can be easily transferred to other types of micro-segregations.

Another example of pattern formation in polymer system exists in the case of fluid membranes. Such membranes typically consist of amphiphiles, which aggregate in a layer such that the polar end groups screen the non-polar hydrocarbon chains from the surrounding water. In most cases, the membranes consist of two adjacent layers that point towards each other with their hydrophobic chains, but there are also various examples of fluid single-layer membranes. Seul and Andelman introduced a simple model of a fluctuating membrane consisting of two components A and B, which influence the bending behaviour of the membrane [4]. The local concentration is characterized by a quantity  $\Psi$ , with  $\Psi = 1$  for pure A regions and  $\Psi = 0$  for pure B regions. In the most simple case, the membrane consists of a monolayer. The undulations of the membrane are described by a height profile  $h(\mathbf{r})$ , where  $\mathbf{r}$  is a 2D vector in the  $x_1$ - $x_2$ -plane. For the elastic part of the free energy the expression

$$\mathcal{F}_c = \int d\mathbf{r} \left( \frac{\sigma}{2} (\nabla_{\mathbf{r}} h)^2 + \frac{\kappa}{2} (\nabla_{\mathbf{r}}^2 h)^2 + \Lambda \Psi \nabla_{\mathbf{r}}^2 h \right) \quad (157)$$

is used. Here,  $\sigma$  is the surface tension and  $\kappa$  is the bending modulus. The coefficient  $\Lambda$  in the last term considers a coupling between the curvature and the local composition  $\Psi$ . The term  $\nabla_{\mathbf{r}}^2 h(\mathbf{r})$  is positive for convex bending and negative for concave bending. Thus, the free energy depends on the bending direction. This sign-dependent bending term does not vanish if the components A and B are asymmetric. The total free energy of the system is given by  $\mathcal{F} = \mathcal{F}_{\Psi} + \mathcal{F}_c$  with the Ginzburg-Landau expression  $\mathcal{F}_{\Psi}$  from equation (144). By minimizing  $\mathcal{F}$  with respect to the membrane shape  $h(\mathbf{r})$ , the authors find the expression

$$\mathcal{F} = \mathcal{F}_0 + \int d\mathbf{r} \left( \frac{b'}{2} (\nabla_{\mathbf{r}} \Psi)^2 + \frac{\Lambda^2 \kappa}{2\sigma^2} (\nabla_{\mathbf{r}}^2 \Psi)^2 \right) \quad (158)$$

with  $b' = b - \Lambda^2/\sigma$ . The important aspect is here that the coupling of the fields  $h(\mathbf{r})$  and  $\Psi(\mathbf{r})$  leads to a coefficient  $b'$  in front of the term  $(\nabla_{\mathbf{r}} \Psi)^2$ , which may be negative. For  $b' < 0$ , the membrane shows a curvature instability, and periodic patterns occur in the shape and the composition of the membrane.

Partial integration of the free energy in equation (158) leads to

$$\begin{aligned} \mathcal{F} &= \mathcal{F}_0 + \int d\mathbf{r} \left( \frac{\Lambda^2 \kappa}{2\sigma^2} \Psi \nabla_{\mathbf{r}}^4 \Psi - \frac{b'}{2} \Psi \nabla_{\mathbf{r}}^2 \Psi \right) \\ &= \mathcal{F}_0 + \int d\mathbf{r} \frac{\Lambda^2 \kappa}{\sigma^2} \frac{\Psi}{2} \left( - \left( \frac{\sigma^2 b'}{2\Lambda^2 \kappa} \right)^2 + \left( \nabla_{\mathbf{r}}^2 - \frac{\sigma^2 b'}{2\Lambda^2 \kappa} \right)^2 \Psi \right), \end{aligned} \quad (159)$$

where boundary terms have been neglected. In the relevant case of  $b' < 0$  the free energy can be written as

$$\mathcal{F} = \mathcal{F}_0 + \frac{\Lambda^2 \kappa}{\sigma^2} \int d\mathbf{r} \frac{\Psi}{2} \left( -k_{\text{ref}}^4 + (k_{\text{ref}}^2 + \nabla_{\mathbf{r}}^2)^2 \right) \Psi, \quad (160)$$

with the reference wave number

$$k_{\text{ref}} = \sqrt{\frac{\sigma |b|}{2\Lambda^2 \kappa}}. \quad (161)$$

If  $\mathcal{F}_0$  is a double-well potential that can be approximated by a fourth-order poly-

nomial in  $\Psi$ , the free energy in equation (160) corresponds to the PFC free energy in equation (1). As a simple example we consider that  $\mathcal{F}_0$  is a symmetric potential

$$\mathcal{F}_0^s = a \left( \tilde{\Psi}^2 - \tilde{\Psi}_0^2 \right)^2, \quad (162)$$

where  $\tilde{\Psi} = \Psi - \bar{\Psi}$  is the deviation of  $\Psi$  from the overall A concentration  $\bar{\Psi}$ . Since integrals over terms linear in  $\Psi$  are constant, we can write the total free energy as

$$\mathcal{F}^s = 4a \int d\mathbf{r} \left( \frac{\tilde{\Psi}}{2} \left( -(\tilde{\Psi}_0^2 + R^4 k_{\text{ref}}^2) + R^4 (k_{\text{ref}}^2 + \nabla_{\mathbf{r}}^2)^2 \right) \tilde{\Psi} + \frac{1}{4} \tilde{\Psi}^4 \right) + C_s \quad (163)$$

with a constant  $C_s$  and

$$R = \left( \frac{\lambda^2 \kappa}{4a\sigma^2} \right)^{1/4}. \quad (164)$$

If we introduce the rescaled spatial coordinates  $\tilde{\mathbf{r}} = R\mathbf{r}$  and the quantity  $k_0 = Rk_{\text{ref}}$ , the free energy is given by

$$\mathcal{F}^s = 4aR^2 \int d\tilde{\mathbf{r}} \left( \frac{\tilde{\Psi}}{2} \left( -\left( \tilde{\Psi}_0^2 + \frac{|b'|}{8a} \right) + \left( k_0^2 + \nabla_{\tilde{\mathbf{r}}}^2 \right)^2 \right) \tilde{\Psi} + \frac{\tilde{\Psi}^4}{4} \right) + C_s. \quad (165)$$

The integral term is proportional to the free energy in equation (1) with  $\beta = \tilde{\Psi}_0^2 + |b'|/8a$ .

### 5.2.3. Comparison of the methods

The SCF theory, the PF theory and the PFC theory are three alternative methods for studying polymer systems. Depending on the specific problem, each of the three methods may be most suited. The SCF theory has originally been an equilibrium theory, which has been extended during the last years to study dynamic systems. Dynamic SCF uses a Langevin equation, in which the dynamics of the system is controlled by the functional derivative of a free-energy functional. The same type of equation, with or without a random noise term, is used in the PF and the PFC theories. The three methods differ in the form of the free-energy functionals.

The SCF method is more microscopically founded than the other two. The underlying concept takes into account the behaviour of single polymer chains in an effective mean field provided by the surrounding polymers. This way, the connectivity and the entropy of the chains are taken into account more explicitly than in the PF or the PFC method. The price for this accuracy is a comparably high calculation effort, which limits the treatable length and time scale of the studied system. If details of molecular fluctuations and the connectivity of the chains are crucial, the SCF method is most accurate. The PF and PFC method depend on various parameters that have to be taken from other calculations and experiments. If these parameters are known, the two methods are an elegant and powerful way to study the dynamics of multiphase systems on a large scale.

The SCF theory has been used to study microphase separations in copolymer systems. In the LOK theory, the free energy used in the SCF method is simplified with the help of the RPA. Close to the critical point, the LOK free-energy functional is of the PFC type. This way the PFC method can be used for copolymer systems as an approximation of the SCF theory, valid in the weak segregation limit. By adding a surface free-energy functional, also surface interactions have been taken

into account [279]. In the more usual case of strong segregation, a more general LOK free-energy functional has been inserted into the PF equation [280]. The resulting model can be seen as an extended version of the PFC method applied on copolymers.

Free energies of the PFC type, which lead to pronounced periodic structures with a preferred wavelength, can be found for various polymer systems. As pointed out in reference [4], there are two mechanisms that can stabilize patterns with a preferred wavelength. One is the competition of long-range and short-range forces. The other is the interplay of two order parameters, like the shape and the composition of multi-component fluid membranes. In many cases, one can derive a free-energy functional of the PFC type, including second- and fourth-order spatial derivatives of the phase field. In the case of the fluid membrane, the  $\nabla_{\mathbf{r}}^4 \Psi$  term is proportional to the bending modulus  $\kappa$ . Thus, by reducing  $\kappa$ , the PFC equation can be transformed smoothly into a PF equation. At the same time, the reference wave number  $k_{\text{ref}}$  diverges. This means that the equilibrium system shows a complete phase separation rather than a microphase separation. While the PFC is well suited for studying the dynamics of systems that form periodic structures in equilibrium or in a steady state, the PF method enables the study of “intermediate” pattern formation of phase-separating systems (where the intermediate structure can be extremely long-living).

As shown for the case of colloids flowing in a polymer solution [187], the PFC method can be used to consider the steric repulsion of polymer coils. Here, it reveals oscillatory structures with a wavelength in the range of the coil diameter, while similar patterns are absent in calculations comparable with the PF theory. The PF theory has been applied on various polymer systems, including polymer solutions, polymer melts, growing polymer crystals and hydrogels. It has been demonstrated that system properties like charge and ion distributions, flow velocity, gravitation, and hydrodynamics can be successfully included into the model. The according methods can be transferred to PFC calculations in polymer systems, resulting in extra terms in the free-energy functional, additional differential equations or advective PFC equations.

The SCF theory is useful, if details of molecular fluctuations and connectivity of the chains are crucial. The PF and PFC method depend on various parameters that have to be taken from other calculations and experiments. If these parameters are known, the methods provide an elegant and powerful way to study the dynamics of multiphase systems on a large scale. The application of PFC models on polymer systems has just started and opened many perspectives for studying polymer systems with pronounced pattern formation.

### 5.3. Application to liquid crystals

The different forms of PFC models for orientable particles as discussed in section 3.1.3 can be applied to compute liquid crystalline systems under various circumstances. First of all, the two-dimensional bulk calculations presented in section 3.2.2 clearly need to be extended to three spatial dimensions. Moreover, a huge application area is found for confined systems. For instance, boundary conditions to the director fields set by external walls can lead to forced topological defects of the orientational order [281]. Here, PFC models for liquid crystals provide a flexible tool to access those numerically. Next, liquid crystalline droplets in air or vacuum provide another type of confinement which induces quite peculiar orientational fields (so-called tactoids [282] or smectic droplets [282]) and again the PFC approach would provide a microscopic avenue to approach those. It would further



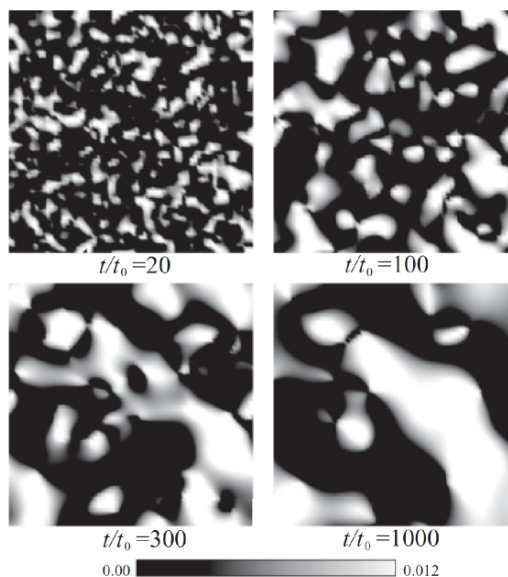


Figure 48. Time evolution of the Schlieren pattern  $\propto Q_{12}^2$  in the  $x_1$ - $x_2$ -plane, which exhibits a dynamical coarsening. The symbol  $t_0$  denotes a characteristic time. (Reproduced with permission from S. Yabunaka and T. Araki, *Polydomain growth at isotropic-nematic transitions in liquid crystalline polymers*, Phys. Rev. E 83 (2011), 061711, no. 6, DOI: 10.1103/PhysRevE.83.061711 © 2011 by the American Physical Society.)

be interesting to generalize the PFC model on curved surfaces in order to explore the structure of thin liquid crystalline bubbles, see, e. g., references [283, 284] for simulation predictions. Last not least the structure of interfaces between two coexisting liquid crystalline phases needs future attention, in particular for phases with positional order.

A further broad range of applications have to do with dynamics. One recent example was performed in reference [158], where the CMA was employed to compute the dynamic coarsening of a disturbed nematic phase. The time evolution of such a nematic phase is shown in the Schlieren patterns in figure 48.

More applications concern the dynamics of topological defects, nucleation in liquid crystalline systems [285], and the orientational dynamics induced by external switching fields [286]. Hence a flourishing future of many more PFC computations for liquid crystals is still lying ahead.

## 6. Summary and outlook

Motivated by the spectacular advances phase-field-crystal modelling has made in recent years, we have reviewed its present status. Besides presenting the original PFC model together with its derivation from dynamical density functional theory, we have reviewed many of its numerous extensions, including those aimed at describing binary solidification, vacancy transport (VPFC), anisotropic molecules (APFC), liquid crystals, and a quantitative description of real systems. We have reviewed, furthermore, a broad range of applications for metallic and soft matter systems (colloids, polymers, and liquid crystals), and for phenomena like the glass transition, and the formation of foams. We have discussed open issues such as coupling to hydrodynamics and the possibility of making quantitative PFC predictions for real materials. The main question at present is what further steps need yet to be made to turn the PFC-type models into even more potent modelling tools.

To summarize the present state of affairs, it seems appropriate to recall some of the concluding remarks of a CECAM workshop dedicated to DDFT- and PFC-type

approaches held in 2009 in Lausanne [194]. It appears that despite the advances made meantime, some of the major issues identified there need yet further attendance. These are the following:

(i) *How to build numerically efficient, quantitative PFC models for a broad spectrum of metallic materials?* The PFC models incorporate microscopic physics in a phenomenological manner. The respective local free-energy functional and the simplified dynamics lead to equations of motion that can be handled fairly efficiently with advanced numerical methods so that simulations containing up to a few times  $10^7$  particles/atoms can be performed with relative ease. A major aim here is to develop a methodology for tuning crystal symmetry, lattice spacing, elastic constants, surface energy, dislocation core energy, dislocation mobility, etc. without sacrificing numerical efficiency. Along this line, methods have been proposed for constructing PFC free energies that allow for the tuning of the crystal structure [132, 135, 136]. The amplitude equations represent an appealing alternative (see, e. g., references [19, 31, 131, 169]), in which the density field is expressed in terms of slowly-varying amplitudes, modulated by the fundamental spatial periodicity of particle density. As demonstrated, this approach realizes a truly multi-scale approach to phase transitions in freezing liquids [20]. Alternatively, one can work directly with the scaled density field of the PFC models and introduce additional model parameters, which can be fitted so that a required set of physical properties is recovered, as done in the case of pure bcc Fe [133].

(ii) *How to construct effective, low-frequency representations from DFT/DDFT?* Provided that one had an accurate and predictive density functional that incorporates *interaction potentials* between the constituent species in a multi-component system, it would become possible to develop an effective description that enables quantitative simulations for microscopically-informed continuum systems that evolve on diffusive time scales. However, one needs to develop first such free-energy functionals. Next, the dynamics of the relevant degrees of freedom should be projected out from the full DDFT description. It may be expected on physical grounds that the shape of a single density peak would relax much faster than the distance between different peak centres. Accordingly, one could “slave” the high-frequency modes associated with the peak shapes to the more slowly evolving modes with low spatial frequencies.

(iii) *The role of fluctuations in DDFT and PFC modelling.* There is a continuing debate about the role of noise in the DDFT- and PFC-type models [193]. Derivations of DDFT from either the Smoluchowski level [97] or within the projection operator technique [74] lead to a deterministic equation of motion without any noise an approximation that becomes problematic near the critical point, or during nucleation, where the system has to leave a metastable free-energy minimum. In the former case fluctuations are needed to obtain the correct critical behaviour, whereas in the latter case, fluctuations are needed to establish an escape route of the system from a metastable phase. Other approaches treat fluctuations on a more phenomenological level. Often, however, the noise strength, though fundamentally correlated with the thermal energy, is treated as a phenomenological fitting parameter (see, e. g., references [34, 203]). This is a fundamental problem, shared by all DDFT and PFC approaches. We note that the addition of noise to the equation of motion in continuum models is not without conceptual difficulties (see reference [195]), even if noise is discretised properly during numerical solution. For example, in the presence of noise, the equilibrium properties of the system change. Furthermore, transformation kinetics generally depends on the spatial and temporal steps and in the limit of infinitely small steps in 3D the free energy of the PFC systems diverges, leading to an ultraviolet “catastrophe”. Evidently, an appropriate “ultra-

violet cutoff”, i. e., filtering out the highest frequencies, is required to regularize the unphysical singularity. Here, a straightforward choice for the cut-off length is the interparticle/interatomic distance, which then removes the unphysical, small wavelength fluctuations [27, 28, 42, 164]. A more elegant handling of the problem is via renormalizing the model parameters so that with noise one recovers the “bare” physical properties (as outlined for the Swift-Hohenberg model in reference [197]). Further systematic investigations are yet needed to settle this issue.

## Appendix A. Coefficients in the PFC models for liquid crystals

### A.1. PFC model for liquid crystals in two spatial dimensions

In the contributions (94)-(96) of the local scaled excess free-energy density, the coefficients

$$A_1 = 8 M_0^0(1), \quad A_2 = -2 M_0^0(3), \quad A_3 = \frac{1}{8} M_0^0(5) \quad (\text{A1})$$

are associated with a gradient expansion of  $\psi^2(\mathbf{r})$ . These coefficients also appear in a different form in the original PFC model [26]. The further coefficients are given by [147, 287]

$$B_1 = 4(M_{-1}^1(2) - M_1^0(2)), \quad (\text{A2})$$

$$B_2 = 2(M_1^1(2) - M_{-1}^2(2)), \quad (\text{A3})$$

$$B_3 = -M_{-2}^2(3) - M_2^0(3), \quad (\text{A4})$$

$$C_1 = 4 M_0^1(1), \quad C_2 = M_0^1(3) - \frac{1}{2} M_{-2}^1(3), \quad C_3 = -M_{-2}^1(3), \quad (\text{A5})$$

and

$$D_1 = 2 M_0^2(1), \quad D_2 = -M_0^2(3). \quad (\text{A6})$$

So far, all these coefficients can also be obtained by using the second-order Ramakrishnan-Yussouff functional for the excess free energy. The remaining coefficients, however, result from higher-order contributions in the functional Taylor expansion [147]. In third order, one obtains for the homogeneous terms the coefficients

$$E_1 = 32 \widehat{M}_{00}^{00}, \quad (\text{A7})$$

$$E_2 = 16 \left( \widehat{M}_{00}^{-11} + 2 \widehat{M}_{00}^{01} \right), \quad (\text{A8})$$

$$E_3 = 8 \left( \widehat{M}_{00}^{-22} + 2 \widehat{M}_{00}^{02} \right), \quad (\text{A9})$$

$$E_4 = 8 \left( 2 \widehat{M}_{00}^{-21} + \widehat{M}_{00}^{11} \right) \quad (\text{A10})$$

and for the terms containing a gradient the coefficients

$$F_1 = 16 \left( \widetilde{M}_{01}^{-10} - 2 \widetilde{M}_{01}^{0-1} + \widetilde{M}_{01}^{00} \right), \quad (\text{A11})$$

$$F_2 = 16 \left( \tilde{M}_{01}^{-21} - \tilde{M}_{01}^{0-2} + \tilde{M}_{01}^{01} - \tilde{M}_{01}^{1-2} \right), \quad (\text{A12})$$

$$F_3 = -16 \left( \tilde{M}_{01}^{-20} - \tilde{M}_{01}^{-21} - \tilde{M}_{01}^{01} + \tilde{M}_{01}^{10} \right), \quad (\text{A13})$$

$$F_4 = -8 \left( \tilde{M}_{01}^{-1-1} - 2 \tilde{M}_{01}^{-11} + \tilde{M}_{01}^{1-1} \right), \quad (\text{A14})$$

$$F_5 = -4 \left( \tilde{M}_{01}^{-2-1} - \tilde{M}_{01}^{-22} - \tilde{M}_{01}^{-12} + \tilde{M}_{01}^{2-1} \right), \quad (\text{A15})$$

$$F_6 = 8 \left( \tilde{M}_{01}^{-22} - \tilde{M}_{01}^{-1-2} + \tilde{M}_{01}^{-12} - \tilde{M}_{01}^{2-2} \right). \quad (\text{A16})$$

In fourth order, only homogeneous terms are kept. The corresponding coefficients are

$$G_1 = 128 \hat{M}_{000}^{000}, \quad (\text{A17})$$

$$G_2 = 192 \left( \hat{M}_{000}^{-101} + \hat{M}_{000}^{001} \right), \quad (\text{A18})$$

$$G_3 = 96 \left( \hat{M}_{000}^{-202} + \hat{M}_{000}^{002} \right), \quad (\text{A19})$$

$$G_4 = 96 \left( 2 \hat{M}_{000}^{-201} + \hat{M}_{000}^{-211} + \hat{M}_{000}^{011} \right), \quad (\text{A20})$$

$$G_5 = 48 \left( \hat{M}_{000}^{-212} + \hat{M}_{000}^{-112} \right), \quad (\text{A21})$$

$$G_6 = 48 \hat{M}_{000}^{-111}, \quad (\text{A22})$$

$$G_7 = 12 \hat{M}_{000}^{-222}. \quad (\text{A23})$$

All the coefficients from above are linear combinations of moments of the Fourier expansion coefficients of the direct correlation functions. These moments are defined through

$$M_{\mathbf{l}^n}^{\mathbf{m}^n}(\boldsymbol{\alpha}^n) = \pi^{2n+1} \rho_{\text{ref}}^{n+1} \left( \prod_{i=1}^n \int_0^\infty dr_i r_i^{\alpha_i} \right) \tilde{c}_{\mathbf{l}^n, \mathbf{m}^n}^{(n+1)}(\mathbf{r}^n) \quad (\text{A24})$$

with the multi-index notation  $\mathbf{X}^n = (X_1, \dots, X_n)$  for  $X \in \{l, m, r, 1, \alpha, \phi, \phi_R\}$  and the abbreviations  $\hat{M}_{\mathbf{l}^n}^{\mathbf{m}^n} = M_{\mathbf{l}^n}^{\mathbf{m}^n}(\mathbf{1}^n)$  and  $\tilde{M}_{l_1 l_2}^{m_1 m_2} = M_{l_1 l_2}^{m_1 m_2}(1, 2)$ . The expansion coefficients of the direct correlation functions are given by

$$\tilde{c}_{\mathbf{l}^n, \mathbf{m}^n}^{(n+1)}(\mathbf{r}^n) = \frac{1}{(2\pi)^{2n}} \int_0^{2\pi} d\phi_{\mathbf{R}}^n \int_0^{2\pi} d\phi^n c^{(n+1)}(\mathbf{r}^n, \phi_{\mathbf{R}}^n, \phi^n) e^{-i(\mathbf{l}^n \cdot \phi_{\mathbf{R}}^n + \mathbf{m}^n \cdot \phi^n)} \quad (\text{A25})$$

with  $\mathbf{r}_1 - \mathbf{r}_{i+1} = R_i \hat{\mathbf{u}}(\varphi_{R_i})$ ,  $\hat{\mathbf{u}}_i = \hat{\mathbf{u}}(\varphi_i)$ ,  $\phi_{R_i} = \varphi_1 - \varphi_{R_i}$ , and  $\phi_i = \varphi_1 - \varphi_{i+1}$ .

When the system is apolar, the modulus  $P(\mathbf{r})$  of the polarization  $\mathbf{P}(\mathbf{r})$  is zero and its orientation  $\hat{\mathbf{p}}(\mathbf{r})$  is not defined, while the direction  $\hat{\mathbf{n}}(\mathbf{r})$  associated with quadrupolar order still exists. Then, symmetry considerations lead to the equalities

$$\tilde{c}_{-1,1}^{(2)}(R) = \tilde{c}_{1,0}^{(2)}(R), \quad \tilde{c}_{-1,2}^{(2)}(R) = \tilde{c}_{1,1}^{(2)}(R), \quad \tilde{c}_{-2,2}^{(2)}(R) = \tilde{c}_{2,0}^{(2)}(R) \quad (\text{A26})$$

between expansion coefficients of the direct pair-correlation function and to the

equations

$$M_{-1}^1(2) = M_1^0(2), \quad M_{-1}^2(2) = M_1^1(2), \quad M_{-2}^2(2) = M_2^0(2) \quad (\text{A27})$$

for the generalized moments. A consequence of these equations is that the coefficients  $B_1$  and  $B_2$  vanish and  $B_3$  becomes more simple.

### A.2. PFC model for liquid crystals in three spatial dimensions

The coefficients in equation (105) appear in three different groups. The first group consists of the three coefficients

$$A_1 = 8\Omega_{000}(0), \quad A_2 = -\frac{4}{3}\Omega_{000}(2), \quad A_3 = \frac{1}{15}\Omega_{000}(4), \quad (\text{A28})$$

that are already known from the original PFC model [26] and belong to the gradient expansion of the translational density. In the next group, the two coefficients

$$B_1 = \frac{16}{15\sqrt{5}}\Omega_{220}(0), \quad B_2 = -\frac{16}{15}\Omega_{022}(2), \quad (\text{A29})$$

that go along with the nematic tensor and the coupling of its gradient with the gradient of the translational density, are collected. The last group contains the Frank constants

$$\tilde{K}_1 = \frac{16}{15}\sqrt{\frac{2}{35}}\Omega_{222}(2), \quad \tilde{K}_2 = \frac{8}{45\sqrt{5}}\Omega_{220}(2) + \frac{1}{3}\tilde{K}_1, \quad (\text{A30})$$

that appear in the Frank free-energy density [145, 157]. All these coefficients are expressed in terms of the generalized moments

$$\Omega_{l_1 l_2 l}(n) = \pi^{3/2} \rho_{\text{ref}}^2 \int_0^\infty dr r^{n+2} \omega_{l_1 l_2 l}(r) \quad (\text{A31})$$

with the expansion coefficients

$$\begin{aligned} \omega_{l_1 l_2 l}(r) = & \sqrt{\frac{4\pi}{2l+1}} \sum_{m=-\min\{l_1, l_2\}}^{\min\{l_1, l_2\}} C(l_1, l_2, l, m, -m, 0) \\ & \times \int d\hat{\mathbf{u}}_1 \int d\hat{\mathbf{u}}_2 c^{(2)}(r\hat{\mathbf{e}}_3, \hat{\mathbf{u}}_1, \hat{\mathbf{u}}_2) \bar{Y}_{l_1 m}(\hat{\mathbf{u}}_1) \bar{Y}_{l_2 -m}(\hat{\mathbf{u}}_2), \end{aligned} \quad (\text{A32})$$

where the symbol  $C(l_1, l_2, l, m_1, m_2, m)$  denotes a Clebsch-Gordan coefficient [288],  $Y_{lm}(\hat{\mathbf{u}})$  is a spherical harmonic,  $\hat{\mathbf{e}}_3$  stands for the Cartesian unit vector co-directional with the  $x_3$ -axis, and  $\bar{\cdot}$  denotes complex conjugation.

As before, equalities between generalized moments with different index-combinations, that can be derived using symmetry considerations [59], have been taken into account in order to reduce the set of generalized moments in equation (105) to its seven independent members.

## Acknowledgements

This work has been supported by the EU FP7 Projects “ENSEMBLE” (contract no. NMP4-SL-2008-213669) and “EXOMET” (contract no. NMP-LA-2012-280421, co-funded by ESA), by the ESA MAP/PECS project “MAGNEPHAS III”, and by the German Research Foundation (DFG) in the context of the DFG Priority Program 1296.

## References

- [1] P.C. Hohenberg and B.I. Halperin, *Theory of dynamic critical phenomena*, Rev. Mod. Phys. 49 (1977), pp. 435–479.
- [2] J.D. Gunton, M. San Miguel, and P.S. Sahni, 1983, The dynamics of first order phase transitions. in *Phase transitions and critical phenomena* 1st ed., Academic Press, London, pp. 267–466.
- [3] M.C. Cross and P.C. Hohenberg, *Pattern formation outside of equilibrium*, Rev. Mod. Phys. 65 (1993), pp. 851–1112.
- [4] M. Seul and D. Andelman, *Domain shapes and patterns – the phenomenology of modulated phases*, Science 267 (1995), pp. 476–483.
- [5] P.M. Chaikin and T.C. Lubensky *Principles of condensed matter physics*, 1st ed., Cambridge University Press, Cambridge, 1995.
- [6] L.M. Pismen *Patterns and interfaces in dissipative dynamics*, 1st ed., Springer, Berlin, 2006.
- [7] M.C. Cross and H. Greenside *Pattern formation and dynamics in nonequilibrium systems*, 1st ed., Cambridge University Press, Cambridge, 2010.
- [8] C. Klemenz, *Hollow cores and step-bunching effects on (001) YBCO surfaces grown by liquid-phase epitaxy*, J. Cryst. Growth 187 (1998), pp. 221–227.
- [9] B. Vasiev, F. Siegert, and C. Weijer, *Multiarmed spirals in excitable media*, Phys. Rev. Lett. 78 (1997), pp. 2489–2492.
- [10] J. Swift and P.C. Hohenberg, *Hydrodynamic fluctuations at the convective instability*, Phys. Rev. A 15 (1977), pp. 319–328.
- [11] S.A. Brazowskii, *Phase transition of an isotropic system to a nonuniform state*, Sov. Phys. JETP 41 (1975), pp. 85–89.
- [12] K.R. Elder, M. Katakowski, M. Haataja, and M. Grant, *Modeling elasticity in crystal growth*, Phys. Rev. Lett. 88 (2002), p. 245701.
- [13] D. Oxtoby, *Course 3: Crystallization of liquids: a density functional approach*, J.P. Hansen, D. Levesque and J. Zinn-Justin, eds., , Vol. 1 of *Proceedings of the Les Houches Summer School, Course LI, 3-28 July 1989* North Holland, Elsevier Science Publishers B. V., Amsterdam, 1991, pp. 145–192.
- [14] Y. Singh, *Density-functional theory of freezing and properties of the ordered phase*, Phys. Rep. 207 (1991), pp. 351–444.
- [15] H. Löwen, *Melting, freezing and colloidal suspensions*, Phys. Rep. 237 (1994), pp. 249–324.
- [16] Y. Rosenfeld, *Free-energy model for the inhomogeneous hard-sphere fluid mixture and density-functional theory of freezing*, Phys. Rev. Lett. 63 (1989), pp. 980–983.
- [17] J.F. Lutsko, *Ginzburg-Landau theory of the liquid-solid interface and nucleation for hard spheres*, Phys. Rev. E 74 (2006), p. 021603.
- [18] A. Härtel, M. Oettel, R.E. Rozas, S.U. Egelhaaf, J. Horbach, and H. Löwen, *Tension and stiffness of the hard-sphere crystal-fluid interface*, Phys. Rev. Lett. 108 (2012), p. 226101.
- [19] N. Goldenfeld, B.P. Athreya, and J.A. Dantzig, *Renormalization group approach to multiscale simulation of polycrystalline materials using the phase field crystal model*, Phys. Rev. E 72 (2005), p. 020601.
- [20] B.P. Athreya, N. Goldenfeld, J.A. Dantzig, M. Greenwood, and N. Provatas, *Adaptive mesh computation of polycrystalline pattern formation using a renormalization-group reduction of the phase-field crystal model*, Phys. Rev. E 76 (2007), p. 056706.
- [21] J.J. Hoyt, M. Asta, and A. Karma, *Atomistic and continuum modeling of dendritic solidification*, Mater. Sci. Eng. R 41 (2003), pp. 121–163.
- [22] L. Gránásy, T. Pusztai, and J.A. Warren, *Modelling polycrystalline solidification using phase field theory*, J. Phys.: Condens. Matter 16 (2004), pp. R1205–R1235.
- [23] A. Karma, *Phase field modeling*, in S. Yip ed., Springer, 2005, pp. 2087–2103.
- [24] H. Emmerich, *Advances of and by phase-field modeling in condensed-matter physics*, Adv. Phys. 57 (2008), pp. 1–87.
- [25] N. Provatas and K. Elder *Phase-field methods in materials science and engineering*, 1st ed., Wiley, Weinheim, 2010.
- [26] K.R. Elder, N. Provatas, J. Berry, P. Stefanovic, and M. Grant, *Phase-field crystal modeling and classical density functional theory of freezing*, Phys. Rev. B 75 (2007), p. 064107.
- [27] T. Pusztai, G. Tegze, G.I. Tóth, L. Környei, G. Bansal, Z. Fan, and L. Gránásy, *Phase-field approach to polycrystalline solidification including heterogeneous and homogeneous nucleation*, J. Phys.: Condens. Matter 20 (2008), p. 404205.
- [28] G.I. Tóth, G. Tegze, T. Pusztai, G. Tóth, and L. Gránásy, *Polymorphism, crystal nucleation and growth in the phase-field crystal model in 2D and 3D*, J. Phys.: Condens. Matter 22 (2010), p. 364101.

- [29] G. Tegze, *Application of atomistic phase-field methods to complex solidification problems*, PhD Thesis, Eötvös University, Budapest, Hungary, 2009 In Hungarian.
- [30] S. Tang, R. Backofen, J. Wang, Y. Zhou, A. Voigt, and Y. Yu, *Three-dimensional phase-field crystal modeling of fcc and bcc dendritic crystal growth*, *J. Cryst. Growth* 334 (2011), pp. 146–152.
- [31] K.R. Elder, Z.F. Huang, and N. Provatas, *Amplitude expansion of the binary phase-field-crystal model*, *Phys. Rev. E* 81 (2010), p. 011602.
- [32] R. Backofen and A. Voigt, *A phase-field-crystal approach to critical nuclei*, *J. Phys.: Condens. Matter* 22 (2010), p. 364104.
- [33] L. Gránásy, G. Tegze, G.I. Tóth, and T. Pusztai, *Phase-field crystal modelling of crystal nucleation, heteroepitaxy and patterning*, *Philos. Mag.* 91 (2011), pp. 123–149.
- [34] J. Hubert, M. Cheng, and H. Emmerich, *Effect of noise-induced nucleation on grain size distribution studied via the phase-field crystal method*, *J. Phys.: Condens. Matter* 21 (2009), p. 464108.
- [35] G.I. Tóth, T. Pusztai, G. Tegze, G. Tóth, and L. Gránásy, *Amorphous nucleation precursor in highly nonequilibrium fluids*, *Phys. Rev. Lett.* 107 (2011), p. 175702.
- [36] J. Berry, K.R. Elder, and M. Grant, *Melting at dislocations and grain boundaries: a phase-field crystal study*, *Phys. Rev. B* 77 (2008), p. 224114.
- [37] J. Mellenthin, A. Karma, and M. Plapp, *Phase-field crystal study of grain-boundary premelting*, *Phys. Rev. B* 78 (2008), p. 184110.
- [38] G. Tegze, L. Gránásy, G.I. Tóth, J.F. Douglas, and T. Pusztai, *Tuning the structure of nonequilibrium soft materials by varying the thermodynamic driving force for crystal ordering*, *Soft Matter* 7 (2011), pp. 1789–1799.
- [39] G. Tegze, G.I. Tóth, and L. Gránásy, *Faceting and branching in 2D crystal growth*, *Phys. Rev. Lett.* 106 (2011), p. 195502.
- [40] K. Wu and A. Karma, *Phase-field crystal modeling of equilibrium bcc-liquid interfaces*, *Phys. Rev. B* 76 (2007), p. 184107.
- [41] S. Majaniemi and N. Provatas, *Deriving surface-energy anisotropy for phenomenological phase-field models of solidification*, *Phys. Rev. E* 79 (2009), p. 011607.
- [42] G. Tegze, L. Gránásy, G.I. Tóth, F. Podmaniczky, A. Jaatinen, T. Ala-Nissila, and T. Pusztai, *Diffusion-controlled anisotropic growth of stable and metastable crystal polymorphs in the phase-field crystal model*, *Phys. Rev. Lett.* 103 (2009), p. 035702.
- [43] R. Backofen and A. Voigt, *Solid-liquid interfacial energies and equilibrium shapes of nanocrystals*, *J. Phys.: Condens. Matter* 21 (2009), p. 464109.
- [44] T. Pusztai, G.I. Tóth, G. Tegze, and L. Gránásy, *Dendritic growth: phase field crystal vs. phase field simulations*, Abstract Booklet, TMS Annual Meeting, 26 February - 3 March 2011, San Diego, USA (2011), p. 31.
- [45] H. Humadi, J. Hoyt, and N. Provatas, *A phase field crystal study of rapid solidification and solute trapping in binary alloys*, Abstract Booklet, TMS Annual Meeting, 11-15 March 2012, Orlando, USA (2012).
- [46] J. Berry, K.R. Elder, and M. Grant, *Simulation of an atomistic dynamic field theory for monatomic liquids: freezing and glass formation*, *Phys. Rev. E* 77 (2008), p. 061506.
- [47] J. Berry and M. Grant, *Modeling multiple time scales during glass formation with phase-field crystals*, *Phys. Rev. Lett.* 106 (2011), p. 175702.
- [48] S. Muralidharan and M. Haataja, *Phase-field crystal modeling of compositional domain formation in ultrathin films*, *Phys. Rev. Lett.* 105 (2010), p. 126101.
- [49] K.R. Elder, G. Rossi, P. Kanerva, F. Sanches, S.C. Ying, E. Granato, C.V. Achim, and T. Ala-Nissila, *Patterning of heteroepitaxial overlayers from nano to micron scales*, *Phys. Rev. Lett.* 108 (2012), p. 226102.
- [50] K.R. Elder and M. Grant, *Modeling elastic and plastic deformations in nonequilibrium processing using phase field crystals*, *Phys. Rev. E* 70 (2004), p. 051605.
- [51] P. Stefanovic, M. Haataja, and N. Provatas, *Phase-field crystals with elastic interactions*, *Phys. Rev. Lett.* 96 (2006), p. 225504.
- [52] Z.F. Huang and K.R. Elder, *Mesosopic and microscopic modeling of island formation in strained film epitaxy*, *Phys. Rev. Lett.* 101 (2008), p. 158701.
- [53] P.Y. Chan, G. Tsekis, J. Dantzig, K.A. Dahmen, and N. Goldenfeld, *Plasticity and dislocation dynamics in a phase field crystal model*, *Phys. Rev. Lett.* 105 (2010), p. 015502.
- [54] R. Spatschek and A. Karma, *Amplitude equations for polycrystalline materials with interaction between composition and stress*, *Phys. Rev. B* 81 (2010), p. 214201.
- [55] K.R. Elder, K. Thornton, and J.J. Hoyt, *The Kirkendall effect in the phase field crystal model*, *Philos. Mag.* 91 (2011), pp. 151–164.
- [56] P.Y. Chan, N. Goldenfeld, and J. Dantzig, *Molecular dynamics on diffusive time scales from the phase-field-crystal equation*, *Phys. Rev. E* 79 (2009), p. 035701R.
- [57] S. Aland, J. Lowengrub, and A. Voigt, *A continuum model of colloid-stabilized interfaces*, *Phys. Fluids* 23 (2011), p. 062103.
- [58] H. Löwen, *A phase-field-crystal model for liquid crystals*, *J. Phys.: Condens. Matter* 22 (2010), p. 364105.
- [59] R. Wittkowski, H. Löwen, and H.R. Brand, *Derivation of a three-dimensional phase-field-crystal model for liquid crystals from density functional theory*, *Phys. Rev. E* 82 (2010), p. 031708.
- [60] C.V. Achim, R. Wittkowski, and H. Löwen, *Stability of liquid crystalline phases in the phase-field-crystal model*, *Phys. Rev. E* 83 (2011), p. 061712.
- [61] N. Guttenberg, N. Goldenfeld, and J. Dantzig, *Emergence of foams from the breakdown of the phase field crystal model*, *Phys. Rev. E* 81 (2010), p. 065301.
- [62] H. Emmerich, L. Gránásy, and H. Löwen, *Selected issues of phase-field crystal simulations*, *Eur. Phys. J. Plus* 126 (2011), p. 102.
- [63] J.P. Hansen and H. Löwen, *Effective interactions between electric double layers*, *Ann. Rev. Phys. Chem.* 51 (2000), pp. 209–242.

- [64] A. Einstein, *Über die von der molekularkinetischen Theorie der Wärme geforderte Bewegung von in ruhenden Flüssigkeiten suspendierten Teilchen*, Ann. Phys. (Leipzig) 322 (1905), pp. 549–560.
- [65] E. Frey and K. Kroy, *Brownian motion: a paradigm of soft matter and biological physics*, Ann. Phys. (Leipzig) 517 (2005), pp. 20–50.
- [66] G.E. Morfill and A.V. Ivlev, *Complex plasmas: an interdisciplinary research field*, Rev. Mod. Phys. 81 (2009), pp. 1353–1404.
- [67] G.E. Morfill, A.V. Ivlev, P. Brandt, and H. Löwen, *Interdisciplinary research with complex plasmas*, G. Bertin, F. de Luca, G. Lodato, R. Pozzoli and M. Romé, eds., , Melville, 2010, pp. 67–79.
- [68] P.N. Pusey, *Course 10: Colloidal suspensions*, J.P. Hansen, D. Levesque and J. Zinn-Justin, eds., , Vol. 2 of *Proceedings of the Les Houches Summer School, Course LI, 3-28 July 1989* North Holland, Elsevier Science Publishers B. V., Amsterdam, 1991, pp. 763–942.
- [69] R. Evans, *The nature of the liquid-vapour interface and other topics in the statistical mechanics of non-uniform, classical fluids*, Adv. Phys. 28 (1979), pp. 143–200.
- [70] S. van Teeffelen, R. Backofen, A. Voigt, and H. Löwen, *Derivation of the phase-field-crystal model for colloidal solidification*, Phys. Rev. E 79 (2009), p. 051404.
- [71] J.K.G. Dhont *An introduction to dynamics of colloids*, 1st ed., Elsevier, Amsterdam, 1996.
- [72] M. Doi and S.F. Edwards *The theory of polymer dynamics*, 1st ed., Oxford University Press, Oxford, 2007.
- [73] H. Risken *The Fokker-Planck equation: methods of solution and applications*, 3rd ed., Springer, Berlin, 1996.
- [74] P. Español and H. Löwen, *Derivation of dynamical density functional theory using the projection operator technique*, J. Chem. Phys. 131 (2009), p. 244101.
- [75] A.J. Archer, *Dynamical density functional theory for dense atomic liquids*, J. Phys.: Condens. Matter 18 (2006), pp. 5617–5628.
- [76] ———, *Dynamical density functional theory for molecular and colloidal fluids: a microscopic approach to fluid mechanics*, J. Chem. Phys. 130 (2009), p. 014509.
- [77] U.M.B. Marconi and S. Melchionna, *Dynamic density functional theory versus kinetic theory of simple fluids*, J. Phys.: Condens. Matter 22 (2010), p. 364110.
- [78] U.M.B. Marconi, P. Tarazona, F. Cecconi, and S. Melchionna, *Beyond dynamic density functional theory: the role of inertia*, J. Phys.: Condens. Matter 20 (2008), p. 494233.
- [79] R. Roth, *Fundamental measure theory for hard-sphere mixtures: a review*, J. Phys.: Condens. Matter 22 (2010), p. 063102.
- [80] R. Roth, R. Evans, A. Lang, and G. Kahl, *Fundamental measure theory for hard-sphere mixtures revisited: the White Bear version*, J. Phys.: Condens. Matter 14 (2002), pp. 12063–12078.
- [81] H. Graf and H. Löwen, *Density functional theory for hard spherocylinders: phase transitions in the bulk and in the presence of external fields*, J. Phys.: Condens. Matter 11 (1999), pp. 1435–1452.
- [82] H. Hansen-Goos and K. Mecke, *Fundamental measure theory for inhomogeneous fluids of nonspherical hard particles*, Phys. Rev. Lett. 102 (2009), p. 018302.
- [83] H. Löwen, 2010, Applications of density functional theory in soft condensed matter. in *Understanding soft condensed matter via modeling and computation* World Scientific Publishing, Singapore, pp. 9–45.
- [84] A. Poniewierski and R. Holyst, *Density-functional theory for nematic and smectic-A ordering of hard spherocylinders*, Phys. Rev. Lett. 61 (1988), pp. 2461–2464.
- [85] T.V. Ramakrishnan and M. Yussouff, *First-principles order-parameter theory of freezing*, Phys. Rev. B 19 (1979), pp. 2775–2794.
- [86] Y. Rosenfeld, M. Schmidt, H. Löwen, and P. Tarazona, *Fundamental-measure free-energy density functional for hard spheres: dimensional crossover and freezing*, Phys. Rev. E 55 (1997), pp. 4245–4263.
- [87] W.A. Curtin and N.W. Ashcroft, *Density-functional theory and freezing of simple liquids*, Phys. Rev. Lett. 56 (1986), pp. 2775–2778.
- [88] R. Ohnesorge, H. Löwen, and H. Wagner, *Density-functional theory of surface melting*, Phys. Rev. A 43 (1991), pp. 2870–2878.
- [89] ———, *Density distribution in a hard-sphere crystal*, Europhys. Lett. 22 (1993), pp. 245–249.
- [90] ———, *Density functional theory of crystal-fluid interfaces and surface melting*, Phys. Rev. E 50 (1994), pp. 4801–4809.
- [91] R. Evans, 1992, Density functionals in the theory of nonuniform fluids. in *Fundamentals of inhomogeneous fluids* 1st ed., Marcel Dekker, New York, pp. 85–176.
- [92] J.P. Hansen and I.R. McDonald *Theory of simple liquids*, 3rd ed., Elsevier Academic Press, Amsterdam, 2006.
- [93] V.I. Kalikmanov *Statistical physics of fluids: basic concepts and applications*, 2nd ed., Springer, Berlin, 2010.
- [94] H. Löwen, *Density functional theory of inhomogeneous classical fluids: recent developments and new perspectives*, J. Phys.: Condens. Matter 14 (2002), pp. 11897–11905.
- [95] U.M.B. Marconi and P. Tarazona, *Dynamic density functional theory of fluids*, J. Chem. Phys. 110 (1999), pp. 8032–8044.
- [96] ———, *Dynamic density functional theory of fluids*, J. Phys.: Condens. Matter 12 (2000), pp. 413–418.
- [97] A.J. Archer and R. Evans, *Dynamical density functional theory and its application to spinodal decomposition*, J. Chem. Phys. 121 (2004), pp. 4246–4254.
- [98] A.J. Archer, *Dynamical density functional theory: binary phase-separating colloidal fluid in a cavity*, J. Phys.: Condens. Matter 17 (2005), pp. 1405–1427.
- [99] H.H. Wensink and H. Löwen, *Aggregation of self-propelled colloidal rods near confining walls*, Phys. Rev. E 78 (2008), p. 031409.
- [100] M. Rex and H. Löwen, *Dynamical density functional theory with hydrodynamic interactions and colloids in unstable traps*, Phys. Rev. Lett. 101 (2008), p. 148302.



- [101] ———, *Dynamical density functional theory for colloidal dispersions including hydrodynamic interactions*, 28 (2009), pp. 139–146.
- [102] M. Rauscher, *DDFT for Brownian particles and hydrodynamics*, J. Phys.: Condens. Matter 22 (2010), p. J4109.
- [103] M. Rex, H.H. Wensink, and H. Löwen, *Dynamical density functional theory for anisotropic colloidal particles*, Phys. Rev. E 76 (2007), p. 021403.
- [104] R. Wittkowski and H. Löwen, *Dynamical density functional theory for colloidal particles with arbitrary shape*, Mol. Phys. 109 (2011), pp. 2935–2943.
- [105] S. van Teeffelen, C.N. Likos, N. Hoffmann, and H. Löwen, *Density functional theory of freezing for soft interactions in two dimensions*, Europhys. Lett. 75 (2006), pp. 583–589.
- [106] J.L. Barrat, *Role of triple correlations in the freezing of the one-component plasma*, Europhys. Lett. 3 (1987), pp. 523–526.
- [107] J.L. Barrat, J.P. Hansen, and G. Pastore, *Factorization of the triplet direct correlation function in dense fluids*, Phys. Rev. Lett. 58 (1987), pp. 2075–2078.
- [108] ———, *On the equilibrium structure of dense fluids*, Mol. Phys. 63 (1988), pp. 747–767.
- [109] R. van Roij, P. Bolhuis, B. Mulder, and D. Frenkel, *Transverse interlayer order in lyotropic smectic liquid crystals*, Phys. Rev. E 52 (1995), pp. R1277–R1280.
- [110] C.N. Likos, N. Hoffmann, H. Löwen, and A.A. Louis, *Exotic fluids and crystals of soft polymeric colloids*, J. Phys.: Condens. Matter 14 (2002), pp. 7681–7698.
- [111] C.N. Likos, A. Lang, M. Watzlawek, and H. Löwen, *Criterion for determining clustering versus reentrant melting behavior for bounded interaction potentials*, Phys. Rev. E 63 (2001), p. 031206.
- [112] A.A. Louis, *Effective potentials for polymers and colloids: beyond the van der Waals picture of fluids?*, Phil. Trans. Roy. Soc. Lond. A 359 (2001), pp. 939–960.
- [113] W.A. Curtin and N.W. Ashcroft, *Weighted-density-functional theory of inhomogeneous liquids and the freezing transition*, Phys. Rev. A 32 (1985), pp. 2909–2919.
- [114] A.R. Denton and N.W. Ashcroft, *Modified weighted-density-functional theory of nonuniform classical liquids*, Phys. Rev. A 39 (1989), pp. 4701–4708.
- [115] H. Hansen-Goos and K. Mecke, *Tensorial density functional theory for non-spherical hard-body fluids*, J. Phys.: Condens. Matter 22 (2010), p. 364107.
- [116] Y. Rosenfeld, M. Schmidt, H. Löwen, and P. Tarazona, *Dimensional crossover and the freezing transition in density functional theory*, J. Phys.: Condens. Matter 8 (1996), pp. L577–L581.
- [117] P. Tarazona, *Density functional for hard sphere crystals: a fundamental measure approach*, Phys. Rev. Lett. 84 (2000), pp. 694–697.
- [118] Y. Rosenfeld, *Density functional theory of molecular fluids: free-energy model for the inhomogeneous hard-body fluid*, Phys. Rev. E 50 (1994), pp. R3318–R3321.
- [119] M. von Smoluchowski, *Über Brownsche Molekularbewegung unter Einwirkung äußerer Kräfte und deren Zusammenhang mit der verallgemeinerten Diffusionsgleichung*, Ann. Phys. (Leipzig) 353 (1916), pp. 1103–1112.
- [120] S. van Teeffelen, C.N. Likos, and H. Löwen, *Colloidal crystal growth at externally imposed nucleation clusters*, Phys. Rev. Lett. 100 (2008), p. 108302.
- [121] H. Löwen, *Colloidal soft matter under external control*, J. Phys.: Condens. Matter 13 (2001), pp. R415–R432.
- [122] H. Löwen, T. Beier, and H. Wagner, *Van der Waals theory of surface melting*, Europhys. Lett. 9 (1989), pp. 791–796.
- [123] ———, *Multiple order parameter theory of surface melting: a van der Waals approach*, Z. Phys. B 79 (1990), pp. 109–118.
- [124] J.F. Lutsko, *First principles derivation of Ginzburg-Landau free energy models for crystalline systems*, Physica A 366 (2006), pp. 229–242.
- [125] S.R.d. Groot and P. Mazur *Non-equilibrium thermodynamics*, 1st ed., Dover Publications, New York, 1984.
- [126] P.C. Martin, O. Parodi, and P.S. Pershan, *Unified hydrodynamic theory for crystals, liquid crystals, and normal fluids*, Phys. Rev. A 6 (1972), pp. 2401–2420.
- [127] L.E. Reichl *A modern course in statistical physics*, 2nd ed., Wiley, New York, 1998.
- [128] P.K. Galenko, D.A. Danilov, and V.G. Lebedev, *Phase-field-crystal and Swift-Hohenberg equations with fast dynamics*, Phys. Rev. E 79 (2009), p. 051110.
- [129] S. Majaniemi and M. Grant, *Dissipative phenomena and acoustic phonons in isothermal crystals: a density-functional theory study*, Phys. Rev. B 75 (2007), p. 054301.
- [130] S. Majaniemi, M. Nonomura, and M. Grant, *First-principles and phenomenological theories of hydrodynamics of solids*, Eur. Phys. J. B 66 (2008), pp. 329–335.
- [131] B.P. Athreya, N. Goldenfeld, and J.A. Dantzig, *Renormalization-group theory for the phase-field crystal equation*, Phys. Rev. E 74 (2006), p. 011601.
- [132] K. Wu, A. Adland, and A. Karma, *Phase-field-crystal model for fcc ordering*, Phys. Rev. E 81 (2010), p. 061601.
- [133] A. Jaatinen, C.V. Achim, K.R. Elder, and T. Ala-Nissila, *Thermodynamics of bcc metals in phase-field-crystal models*, Phys. Rev. E 80 (2009), p. 031602.
- [134] M. Greenwood, N. Provatas, and J. Rottler, *Free energy functionals for efficient phase field crystal modeling of structural phase transformations*, Phys. Rev. Lett. 105 (2010), p. 045702.
- [135] M. Greenwood, J. Rottler, and N. Provatas, *Phase-field-crystal methodology for modeling of structural transformations*, Phys. Rev. E 83 (2011), p. 031601.
- [136] K. Wu, M. Plapp, and P.W. Voorhees, *Controlling crystal symmetries in phase-field crystal models*, J. Phys.: Condens. Matter 22 (2010), p. 364102.
- [137] R. Prieler, J. Hubert, D. Li, B. Verleye, R. Haberkern, and H. Emmerich, *An anisotropic phase-field crystal model for heterogeneous nucleation of ellipsoidal colloids*, J. Phys.: Condens. Matter 21 (2009), p. 464110.
- [138] M.A. Choudhary, D. Li, H. Emmerich, and H. Löwen, *DDFT calibration and investigation of an*

- anisotropic phase-field crystal model*, J. Phys.: Condens. Matter 23 (2011), p. 265005.
- [139] M.A. Choudhary, J. Kundin, and H. Emmerich, *Phase-field crystal modeling of anisotropic material systems of arbitrary Poisson's ratio*, Philos. Mag. Lett. (2012) Published electronically: <http://www.tandfonline.com/doi/abs/10.1080/09500839.2012.686173>.
- [140] G.I. Tóth, G. Tegze, T. Pusztai, and L. Gránásy, *Heterogeneous crystal nucleation: the effect of lattice mismatch*, Phys. Rev. Lett. 108 (2012), p. 025502.
- [141] A. Karma and W.J. Rappel, *Phase-field model of dendritic sidebranching with thermal noise*, Phys. Rev. E 60 (1999), pp. 3614–3625.
- [142] D.J.B. Lloyd, B. Sandstede, D. Avitabile, and A.R. Champneys, *Localized hexagon patterns of the planar Swift-Hohenberg equation*, SIAM J. Appl. Dyn. Syst. 7 (2008), pp. 1049–1100.
- [143] M.J. Robbins, A.J. Archer, U. Thiele, and E. Knobloch, *Modeling the structure of liquids and crystals using one- and two-component modified phase-field crystal models*, Phys. Rev. E 85 (2012), p. 061408.
- [144] P.G. de Gennes, *Short range order effects in the isotropic phase of nematics and cholesterics*, Mol. Cryst. Liq. Cryst. 12 (1971), pp. 193–214.
- [145] P.G. de Gennes and J. Prost *The physics of liquid crystals*, 2nd ed., Oxford University Press, Oxford, 1995.
- [146] H.R. Brand and K. Kawasaki, *Gradient free energy of nematic liquid crystals with topological defects*, J. Phys. C 19 (1986), pp. 937–942.
- [147] R. Wittkowski, H. Löwen, and H.R. Brand, *Polar liquid crystals in two spatial dimensions: the bridge from microscopic to macroscopic modeling*, Phys. Rev. E 83 (2011), p. 061706.
- [148] P. Bolhuis and D. Frenkel, *Tracing the phase boundaries of hard spherocylinders*, J. Chem. Phys. 106 (1997), pp. 666–687.
- [149] H. Löwen, *Brownian dynamics of hard spherocylinders*, Phys. Rev. E 50 (1994), pp. 1232–1242.
- [150] D. Frenkel, B.M. Mulder, and J.P. McTague, *Phase diagram of a system of hard ellipsoids*, Phys. Rev. Lett. 52 (1984), pp. 287–290.
- [151] Th. Kirchhoff, H. Löwen, and R. Klein, *Dynamical correlations in suspensions of charged rodlike macromolecules*, Phys. Rev. E 53 (1996), pp. 5011–5022.
- [152] H. Löwen, *Charged rodlike colloidal suspensions: an ab initio approach*, J. Chem. Phys. 100 (1994), pp. 6738–6749.
- [153] ———, *Interaction between charged rodlike colloidal particles*, Phys. Rev. Lett. 72 (1994), pp. 424–427.
- [154] D.J. Cleaver, C.M. Care, M.P. Allen, and M.P. Neal, *Extension and generalization of the Gay-Berne potential*, Phys. Rev. E 54 (1996), pp. 559–567.
- [155] H. Fukunaga, J.I. Takimoto, and M. Doi, *Molecular dynamics simulation study on the phase behavior of the Gay-Berne model with a terminal dipole and a flexible tail*, J. Chem. Phys. 120 (2004), pp. 7792–7800.
- [156] L. Muccioli and C. Zannoni, *A deformable Gay Berne model for the simulation of liquid crystals and soft materials*, Chem. Phys. Lett. 423 (2006), pp. 1–6.
- [157] S. Chandrasekhar *Liquid crystals*, 2nd ed., Cambridge University Press, Cambridge, 1992.
- [158] S. Yabunaka and T. Araki, *Polydomain growth at isotropic-nematic transitions in liquid crystalline polymers*, Phys. Rev. E 83 (2011), p. 061711.
- [159] T. Hirouchi, T. Takaki, and Y. Tomita, *Development of numerical scheme for phase field crystal deformation simulation*, Comput. Mater. Sci. 44 (2009), pp. 1192–1197.
- [160] S.M. Wise, C. Wang, and J.S. Lowengrub, *An energy-stable and convergent finite-difference scheme for the phase field crystal equation*, SIAM J. Numer. Anal. 47 (2009), pp. 2269–2288.
- [161] C. Wang and S.M. Wise, *An energy stable and convergent finite-difference scheme for the modified phase field crystal equation*, SIAM J. Numer. Anal. 49 (2011), pp. 945–969.
- [162] Z. Hu, S.M. Wise, C. Wang, and J.S. Lowengrub, *Stable and efficient finite-difference nonlinear-multigrid schemes for the phase field crystal equation*, J. Comp. Phys. 228 (2009), pp. 5323–5339.
- [163] M. Cheng and J.A. Warren, *An efficient algorithm for solving the phase field crystal model*, J. Comp. Phys. 227 (2008), pp. 6241–6248.
- [164] G. Tegze, G. Bansel, G.I. Tóth, T. Pusztai, Z. Fan, and L. Gránásy, *Advanced operator splitting-based semi-implicit spectral method to solve the binary phase-field crystal equations with variable coefficients*, J. Comp. Phys. 228 (2009), pp. 1612–1623.
- [165] R. Backofen, A. Rätz, and A. Voigt, *Nucleation and growth by a phase field crystal (PFC) model*, Philos. Mag. Lett. 87 (2007), pp. 813–820.
- [166] G.I. Tóth and G. Tegze (2012), to be published.
- [167] Y. Shiwa, *Comment on “Renormalization-group theory for the phase-field crystal equation”*, Phys. Rev. E 79 (2009), p. 013601.
- [168] Z.F. Huang and K.R. Elder, *Morphological instability, evolution, and scaling in strained epitaxial films: an amplitude-equation analysis of the phase-field-crystal model*, Phys. Rev. B 81 (2010), p. 165421.
- [169] D. Yeon, Z. Huang, K.R. Elder, and K. Thornton, *Density-amplitude formulation of the phase-field crystal model for two-phase coexistence in two and three dimensions*, Philos. Mag. 90 (2010), pp. 237–263.
- [170] G.F. Kendrick, T.J. Sluckin, and M.J. Grimson, *Macrocrystal phases in charged colloidal suspensions*, Europhys. Lett. 6 (1988), p. 567.
- [171] A. Jaatinen and T. Ala-Nissila, *Extended phase diagram of the three-dimensional phase field crystal model*, J. Phys.: Condens. Matter 22 (2010), p. 205402.
- [172] A. de Candia, E. Del Gado, A. Fierro, N. Sator, M. Tarzia, and A. Coniglio, *Columnar and lamellar phases in attractive colloidal systems*, Phys. Rev. E 74 (2006), p. 010403R.
- [173] M. Bestehorn and H. Haken, *Transient patterns of the convection instability: a model-calculation*, Z. Phys. B 57 (1984), pp. 329–333.
- [174] C. Kubstrup, H. Herrero, and C. Pérez-García, *Fronts between hexagons and squares in a generalized*

- Swift-Hohenberg equation*, Phys. Rev. E 54 (1996), pp. 1560–1569.
- [175] P. Cremer, M. Marechal, and H. Löwen (2012), to be published.
- [176] A.F. Demirörs, P.M. Johnson, C.M. van Kats, A. van Blaaderen, and A. Imhof, *Directed self-assembly of colloidal dumbbells with an electric field*, Langmuir 26 (2010), pp. 14466–14471.
- [177] S.J. Gerbode, U. Agarwal, D.C. Ong, C.M. Liddell, F. Escobedo, and I. Cohen, *Glassy dislocation dynamics in 2D colloidal dimer crystals*, Phys. Rev. Lett. 105 (2010), p. 078301.
- [178] M. Marechal and M. Dijkstra, *Stability of orientationally disordered crystal structures of colloidal hard dumbbells*, Phys. Rev. E 77 (2008), p. 061405.
- [179] T.J. Stasevich, H. Gebremariam, T.L. Einstein, M. Giesen, C. Steimer, and H. Ibach, *Low-temperature orientation dependence of step stiffness on (111) surfaces*, Phys. Rev. B 71 (2005), p. 245414.
- [180] V.V. Hoang, *Molecular dynamics simulation of liquid and amorphous Fe nanoparticles*, Nanotechnology 20 (2009), p. 295703.
- [181] Y. Wang, X. Wang, and H. Wang, *Atomic simulation on evolution of nano-crystallization in amorphous metals*, Trans. Nonferrous Met. Soc. China 16 (2006), pp. s327–s331.
- [182] J.A.P. Ramos, E. Granato, S.C. Ying, C.V. Achim, K.R. Elder, and T. Ala-Nissila, *Dynamical transitions and sliding friction of the phase-field-crystal model with pinning*, Phys. Rev. E 81 (2010), p. 011121.
- [183] C.V. Achim, M. Karttunen, K.R. Elder, E. Granato, T. Ala-Nissila, and S.C. Ying, *Phase diagram and commensurate-incommensurate transitions in the phase field crystal model with an external pinning potential*, Phys. Rev. E 74 (2006), p. 021104.
- [184] C.V. Achim, J.A.P. Ramos, M. Karttunen, K.R. Elder, E. Granato, T. Ala-Nissila, and S.C. Ying, *Nonlinear driven response of a phase-field crystal in a periodic pinning potential*, Phys. Rev. E 79 (2009), p. 011606.
- [185] M. Chen, D. Li, and H. Emmerich (2012), to be published.
- [186] H. Emmerich, in *The diffuse interface approach in material science: thermodynamic concepts and applications of phase-field models*, Lecture Notes in Physics Monographs, M 73 Springer, Berlin, 2003, pp. 1–186.
- [187] S. Praetorius and A. Voigt, *A phase field crystal approach for particles in a flowing solvent*, Macromol. Theory Simul. 20 (2011), pp. 541–547.
- [188] M. Rauscher, A. Domínguez, M. Krüger, and F. Penna, *A dynamic density functional theory for particles in a flowing solvent*, J. Chem. Phys. 127 (2007), p. 244906.
- [189] F. Penna, J. Dzubiella, and P. Tarazona, *Dynamic density functional study of a driven colloidal particle in polymer solutions*, Phys. Rev. E 68 (2003), p. 061407.
- [190] D. Li, H.L. Yang, and H. Emmerich, *Phase field model simulations of hydrogel dynamics under chemical stimulation*, Coll. Polym. Sci. 289 (2011), pp. 513–521.
- [191] R. Backofen, M. Gräf, D. Potts, S. Praetorius, A. Voigt, and T. Witkowski, *A continuous approach to discrete ordering on  $S^2$* , Multiscale Model. Simul. 9 (2011), pp. 314–334.
- [192] H. Löwen, *Density functional theory: from statics to dynamics*, J. Phys.: Condens. Matter 15 (2003), pp. V1–V3.
- [193] A.J. Archer and M. Rauscher, *Dynamical density functional theory for interacting Brownian particles: stochastic or deterministic?*, J. Phys. A 37 (2004), pp. 9325–9333.
- [194] M. Haataja, L. Gránásy, and H. Löwen, *Classical density functional theory methods in soft and hard matter*, J. Phys.: Condens. Matter 22 (2010), p. 360301.
- [195] M. Plapp, *Remarks on some open problems in phase-field modelling of solidification*, Philos. Mag. 91 (2011), pp. 25–44.
- [196] G.H. Fredrickson and K. Binder, *Kinetics of metastable states in block copolymer melts*, J. Chem. Phys. 91 (1989), pp. 7265–7275.
- [197] N.A. Gross, M. Ignatiev, and B. Chakraborty, *Kinetics of ordering in fluctuation-driven first-order transitions: simulation and theory*, Phys. Rev. E 62 (2000), pp. 6116–6125.
- [198] M. Asta, C. Beckermann, A. Karma, W. Kurz, R. Napolitano, M. Plapp, G. Purdy, M. Rappaz, and R. Trivedi, *Solidification microstructures and solid-state parallels: recent developments, future directions*, Acta Mater. 57 (2009), pp. 941–971.
- [199] J.Q. Broughton and G.H. Gilmer, *Molecular dynamics investigation of the crystal-fluid interface. VI. Excess surface free energies of crystal-liquid systems*, J. Chem. Phys. 84 (1986), pp. 5759–5768.
- [200] K.F. Kelton and A.L. Greer (eds.) *Nucleation in condensed matter: applications in materials and biology*, 1st ed., Pergamon Press, Oxford, 2005.
- [201] A.L. Greer, A.M. Bunn, A. Tronche, P.V. Evans, and D.J. Bristow, *Modelling of inoculation of metallic melts: application to grain refinement of aluminium by Al-Ti-B*, Acta Mater. 48 (2000), pp. 2823–2835.
- [202] K. Sandomirski, E. Allahyarov, H. Löwen, and S. Egelhaaf, *Heterogeneous crystallization of hard-sphere colloids near a wall*, Soft Matter 7 (2011), pp. 8050–8055.
- [203] J.A.P. Ramos, E. Granato, C.V. Achim, S.C. Ying, K.R. Elder, and T. Ala-Nissila, *Thermal fluctuations and phase diagrams of the phase-field crystal model with pinning*, Phys. Rev. E 78 (2008), p. 031109.
- [204] J. Rottler, M. Greenwood, and B. Ziebarth, *Morphology of monolayer films on quasicrystalline surfaces from the phase field crystal model*, J. Phys.: Condens. Matter 24 (2012), p. 135002.
- [205] Z.F. Huang, K.R. Elder, and N. Provatas, *Phase-field-crystal dynamics for binary systems: derivation from dynamical density functional theory, amplitude equation formalism, and applications to alloy heterostructures*, Phys. Rev. E 82 (2010), p. 021605.
- [206] K.R. Elder and Z.F. Huang, *A phase field crystal study of epitaxial island formation on nanomembranes*, J. Phys.: Condens. Matter 22 (2010), p. 364103.
- [207] M.J. Aziz, *Model for solute redistribution during rapid solidification*, J. Appl. Phys. 53 (1982), pp. 1158–1168.
- [208] K.A. Jackson, K.M. Beatty, and K.A. Gudgel, *An analytical model for non-equilibrium segregation*

- during crystallization, *J. Cryst. Growth* 271 (2004), pp. 481–494.
- [209] M.J. Aziz and T. Kaplan, *Continuous growth model for interface motion during alloy solidification*, *Acta Metall.* 36 (1988), pp. 2335–2347.
- [210] P.K. Galenko, E.V. Abramova, D. Jou, D.A. Danilov, V.G. Lebedev, and D.M. Herlach, *Solute trapping in rapid solidification of a binary dilute system: a phase-field study*, *Phys. Rev. E* 84 (2011), p. 041143.
- [211] J. Li, S. Sarkar, W.T. Cox, T.J. Lenosky, E. Bitzek, and Y. Wang, *Diffusive molecular dynamics and its application to nanoindentation and sintering*, *Phys. Rev. B* 84 (2011), p. 054103.
- [212] A. Karma, personal communication.
- [213] S. Alexander and J. McTague, *Should all crystals be bcc? Landau theory of solidification and crystal nucleation*, *Phys. Rev. Lett.* 41 (1978), pp. 702–705.
- [214] P.R. ten Wolde, M.J. Ruiz-Montero, and D. Frenkel, *Numerical evidence for bcc ordering at the surface of a critical fcc nucleus*, *Phys. Rev. Lett.* 75 (1995), pp. 2714–2717.
- [215] C. Desgranges and J. Delhommelle, *Controlling polymorphism during the crystallization of an atomic fluid*, *Phys. Rev. Lett.* 98 (2007), p. 235502.
- [216] G.I. Tóth, J.R. Morris, and L. Gránásy, *Ginzburg-Landau-type multiphase field model for competing fcc and bcc nucleation*, *Phys. Rev. Lett.* 106 (2011), p. 045701.
- [217] O. Galkin and P.G. Vekilov, *Control of protein crystal nucleation around the metastable liquid-liquid phase boundary*, *Proc. Nat. Acad. Sci.* 97 (2000), pp. 6277–6281.
- [218] P.R. ten Wolde and D. Frenkel, *Enhancement of protein crystal nucleation by critical density fluctuations*, *Science* 277 (1997), pp. 1975–1978.
- [219] J.F. Lutsko and G. Nicolis, *Theoretical evidence for a dense fluid precursor to crystallization*, *Phys. Rev. Lett.* 96 (2006), p. 046102.
- [220] T. Schilling, H.J. Schöpe, M. Oettel, G. Opletal, and I. Snook, *Precursor-mediated crystallization process in suspensions of hard spheres*, *Phys. Rev. Lett.* 105 (2010), p. 025701.
- [221] T.H. Zhang and X.Y. Liu, *How does a transient amorphous precursor template crystallization*, *J. Am. Chem. Soc.* 129 (2007), pp. 13520–13526.
- [222] H.J. Schöpe, G. Bryant, and W. van Meegen, *Two-step crystallization kinetics in colloidal hard-sphere systems*, *Phys. Rev. Lett.* 96 (2006), p. 175701.
- [223] P. Dillmann, G. Maret, and P. Keim, *Polycrystalline solidification in a quenched 2D colloidal system*, *J. Phys.: Condens. Matter* 20 (2008), p. 404216.
- [224] W. Schommers, *Pair potentials in disordered many-particle systems: a study for liquid gallium*, *Phys. Rev. A* 28 (1983), pp. 3599–3605.
- [225] J.P. Doye, D.J. Wales, F.H.M. Zetterling, and M. Dzugutov, *The favored cluster structures of model glass formers*, *J. Chem. Phys.* 119 (2003), pp. 2792–2799.
- [226] O. Mishima and H.E. Stanley, *Decompression-induced melting of ice IV and the liquid-liquid transition in water*, *Nature* 392 (1998), pp. 164–168.
- [227] M. Shimoji *Liquid metals: an introduction to the physics and chemistry of metals in the liquid state*, 1st ed., Academic Press, London, 1977.
- [228] M. Castro, *Phase-field approach to heterogeneous nucleation*, *Phys. Rev. B* 67 (2003), p. 035412.
- [229] W.B. Russel, P.M. Chaikin, J. Zhu, W.V. Meyer, and R. Rogers, *Dendritic growth of hard sphere crystals*, *Langmuir* 13 (1997), pp. 3871–3881.
- [230] A.T. Skjeltorp, *Visualization and characterization of colloidal growth from ramified to faceted structures*, *Phys. Rev. Lett.* 58 (1987), pp. 1444–1447.
- [231] L. Gránásy, G. Tegze, G.I. Tóth, F. Podmaniczky, and T. Pusztai, *Phase-field crystal modeling of nucleation, patterning, and early-stage growth in colloidal systems in two and three dimensions*; Abstract Booklet, TMS Annual Meeting, 14–18 February 2010, Seattle, USA.
- [232] J. Maurer, P. Bouissou, B. Perrin, and P. Tabeling, *Faceted dendrites in the growth of  $NH_4Br$  crystals*, *Europhys. Lett.* 8 (1989), p. 67.
- [233] Z. Cheng, P.M. Chaikin, J. Zhu, W.B. Russel, and W.V. Meyer, *Crystallization kinetics of hard spheres in microgravity in the coexistence regime: interactions between growing crystallites*, *Phys. Rev. Lett.* 88 (2001), p. 015501.
- [234] I. Lee, H. Zheng, M.F. Rubner, and P.T. Hammond, *Controlled cluster size in patterned particle arrays via directed adsorption on confined surfaces*, *Adv. Mater.* 14 (2002), pp. 572–577.
- [235] C. Reichhardt and C.J. Olson, *Novel colloidal crystalline states on two-dimensional periodic substrates*, *Phys. Rev. Lett.* 88 (2002), p. 248301.
- [236] A. Mathur, A. Brown, and J. Erlebacher, *Self-ordering of colloidal particles in shallow nanoscale surface corrugations*, *Langmuir* 22 (2006), pp. 582–589.
- [237] J. Sun, Y.Y. Li, H. Dong, P. Zhan, C.J. Tang, M.W. Zhu, and Z.L. Wang, *Fabrication and light-transmission properties of monolayer square symmetric colloidal crystals via controlled convective self-assembly on 1D grooves*, *Adv. Mater.* 20 (2008), pp. 123–128.
- [238] N.V. Dzionkina, M.A. Hempenius, and G.J. Vancso, *Symmetry control of polymer colloidal monolayers and crystals by electrophoretic deposition on patterned surfaces*, *Adv. Mater.* 17 (2005), pp. 237–240.
- [239] K. Dholakia, G. Spalding, and M. MacDonald, *Optical tweezers: the next generation*, *Phys. World* 15 (2002), pp. 31–35.
- [240] M. Hermes, E.C.M. Vermolen, M.E. Leunissen, D.L.J. Vossen, P.D.J. van Oostrum, M. Dijkstra, and A. van Blaaderen, *Nucleation of colloidal crystals on configurable seed structures*, *Soft Matter* 7 (2011), pp. 4623–4628.
- [241] G.I. Tóth and L. Gránásy (2012), to be published.
- [242] S.F. Edwards, *Statistical mechanics of polymers with excluded volume*, *Proc. Phys. Soc. (London)* 85 (1965), pp. 613–624.
- [243] E. Helfand and Y. Tagami, *Theory of interface between immiscible polymers*, *J. Polymer Sci. B Polymer Lett.* 9 (1971), p. 741.
- [244] M. Müller and F. Schmid, *Incorporating fluctuations and dynamics in self-consistent field theories*

- for polymer blends, *Adv. Polym. Sci.* 185 (2005), pp. 1–85.
- [245] F. Schmid, *Self-consistent-field theories for complex fluids*, *J. Phys.: Condens. Matter* 10 (1998), pp. 8105–8138.
- [246] Y.L. Yang, F. Qiu, P. Tang, and H.D. Zhang, *Applications of self-consistent field theory in polymer systems*, *Sci. China B Chem.* 49 (2006), pp. 21–43.
- [247] K.M. Hong and J. Noolandi, *Conformational entropy effects in a compressible lattice fluid theory of polymers*, *Macromol.* 14 (1981), pp. 1229–1234.
- [248] D. Dücks, V. Ganesan, G.H. Fredrickson, and F. Schmid, *Fluctuation effects in ternary  $ab+a+b$  polymeric emulsions*, *Macromol.* 36 (2003), pp. 9237–9248.
- [249] V. Ganesan and G.H. Fredrickson, *Field-theoretic polymer simulations*, *Europhys. Lett.* 55 (2001), pp. 814–820.
- [250] K. Rasmussen and G. Kalosakas, *Improved numerical algorithm for exploring block copolymer mesophases*, *J. Polymer Sci. B Polymer Phys.* 40 (2002), pp. 1777–1783.
- [251] N.M. Maurits and J.G.E.M. Fraaije, *Mesosopic dynamics of copolymer melts: from density dynamics to external potential dynamics using nonlocal kinetic coupling*, *J. Chem. Phys.* 107 (1997), pp. 5879–5889.
- [252] P.E. Rouse, *A theory of the linear viscoelastic properties of dilute solutions of coiling polymers*, *J. Chem. Phys.* 21 (1953), pp. 1272–1280.
- [253] E. Reister, M. Müller, and K. Binder, *Spinodal decomposition in a binary polymer mixture: dynamic self-consistent-field theory and Monte Carlo simulations*, *Phys. Rev. E* 64 (2001), p. 041804.
- [254] T. Honda and T. Kawakatsu, *Hydrodynamic effects on the disorder to order transitions of diblock copolymer melts*, *J. Chem. Phys.* 129 (2008), p. 114904.
- [255] D.M. Hall, T. Lookman, G.H. Fredrickson, and S. Banerjee, *Numerical method for hydrodynamic transport of inhomogeneous polymer melts*, *J. Comp. Phys.* 224 (2007), pp. 681–698.
- [256] ———, *Hydrodynamic self-consistent field theory for inhomogeneous polymer melts*, *Phys. Rev. Lett.* 97 (2006), p. 114501.
- [257] D. Anders and K. Weinberg, *A variational approach to the decomposition of unstable viscous fluids and its consistent numerical approximation*, *Z. Angew. Math. Mech.* 91 (2011), pp. 609–629.
- [258] H. Tian, J. Shao, Y. Ding, X. Li, and X. Li, *Numerical studies of electrically induced pattern formation by coupling liquid dielectrophoresis and two-phase flow*, *Electrophoresis* 32 (2011), pp. 2245–2252.
- [259] G. Boffetta, A. Mazzino, S. Musacchio, and L. Vozella, *Rayleigh-Taylor instability in a viscoelastic binary fluid*, *J. Fluid Mech.* 643 (2010), pp. 127–136.
- [260] H. Xu and C.T. Bellehumeur, *Modeling the morphology development of ethylene copolymers in rotational molding*, *J. Appl. Polym. Sci.* 102 (2006), pp. 5903–5917.
- [261] P.T. Yue, J.J. Feng, C. Liu, and J. Shen, *Diffuse-interface simulations of drop coalescence and retraction in viscoelastic fluids*, *J. Non-Newtonian Fluid Mech.* 129 (2005), pp. 163–176.
- [262] J.W. Cahn and J.E. Hilliard, *Free energy of a nonuniform system. I. Interfacial free energy*, *J. Chem. Phys.* 28 (1958), pp. 258–267.
- [263] P.J. Flory, *Thermodynamics of high polymer solutions*, *J. Chem. Phys.* 10 (1942), pp. 51–61.
- [264] M.L. Huggins, *Theory of solutions of high polymers*, *J. Am. Chem. Soc.* 64 (1942), pp. 1712–1719.
- [265] Y.C. Li, R.P. Shi, C.P. Wang, X.J. Liu, and Y. Wang, *Predicting microstructures in polymer blends under two-step quench in two-dimensional space*, *Phys. Rev. E* 83 (2011), p. 041502.
- [266] R.B. Bird, C.F. Curtiss, O. Hassager, and R.C. Armstrong *Dynamics of polymeric liquids*, 2nd ed., Vol. 2: Kinetic theory, Wiley, New York, 1987.
- [267] J.G. Oldroyd, *The effect of interfacial stabilizing films on the elastic and viscous properties of emulsions*, *Proc. Roy. Soc. Lond. A* 232 (1955), pp. 567–577.
- [268] J. Beaucourt, T. Biben, and C. Verdier, *Elongation and burst of axisymmetric viscoelastic droplets: a numerical study*, *Phys. Rev. E* 71 (2005), p. 066309.
- [269] P. Yue, C. Zhou, and J.J. Feng, *A computational study of the coalescence between a drop and an interface in Newtonian and viscoelastic fluids*, *Phys. Fluids* 18 (2006), p. 102102.
- [270] V.E. Badalassi, H.D. Ceniceros, and S. Banerjee, *Computation of multiphase systems with phase field models*, *J. Comp. Phys.* 190 (2003), pp. 371–397.
- [271] H. Müller-Krumbhaar, H. Emmerich, E. Brener, and M. Hartmann, *Dewetting hydrodynamics in  $1+1$  dimensions*, *Phys. Rev. E* 63 (2001), p. 026304.
- [272] D. Wang, T. Shi, J. Chen, L. An, and Y. Jia, *Simulated morphological landscape of polymer single crystals by phase field model*, *J. Chem. Phys.* 129 (2008), p. 194903.
- [273] H.J. Xu, R. Matkar, and T. Kyu, *Phase-field modeling on morphological landscape of isotactic polystyrene single crystals*, *Phys. Rev. E* 72 (2005), p. 011804.
- [274] S.M. Allen and J.W. Cahn, *Microscopic theory for antiphase boundary motion and its application to antiphase domain coarsening*, *Acta Metall.* 27 (1979), pp. 1085–1095.
- [275] S. Buddhiranon, N. Kim, and T. Kyu, *Morphology development in relation to the ternary phase diagram of biodegradable  $pdlla/pcl/peo$  blends*, *Macromol. Chem. Phys.* 212 (2011), pp. 1379–1391.
- [276] L. Leibler, *Theory of microphase separation in block co-polymers*, *Macromol.* 13 (1980), pp. 1602–1617.
- [277] T. Ohta and K. Kawasaki, *Equilibrium morphology of block copolymer melts*, *Macromol.* 19 (1986), pp. 2621–2632.
- [278] S.F. Edwards, *The theory of polymer solutions at intermediate concentrations*, *Proc. Phys. Soc. (London)* 88 (1966), pp. 265–280.
- [279] Y. Tsori and D. Andelman, *Diblock copolymer ordering induced by patterned surfaces*, *Europhys. Lett.* 53 (2001), pp. 722–728.
- [280] A.W. Bosse, *Phase-field simulation of long-wavelength line edge roughness in diblock copolymer resists*, *Macromol. Theory Simul.* 19 (2010), pp. 399–406.
- [281] T.C. Lubensky, D. Pettey, N. Currier, and H. Stark, *Topological defects and interactions in nematic emulsions*, *Phys. Rev. E* 57 (1998), pp. 610–625.

- [282] A.A. Verhoeff, R.H.J. Otten, P. van der Schoot, and H.N.W. Lekkerkerker, *Shape and director field deformation of tactoids of plate-like colloids in a magnetic field*, J. Phys. Chem. B 113 (2009), pp. 3704–3708.
- [283] J. Dzubiella, M. Schmidt, and H. Löwen, *Topological defects in nematic droplets of hard spherocylinders*, Phys. Rev. E 62 (2000), pp. 5081–5091.
- [284] J.A. Moreno-Razo, E.J. Sambriski, N.L. Abbott, J.P. Hernandez-Ortiz, and J.J. de Pablo, *Liquid-crystal-mediated self-assembly at nanodroplet interfaces*, Nature 485 (2012), pp. 86–89.
- [285] T. Schilling and D. Frenkel, *Self-poisoning of crystal nuclei in hard-rod liquids*, J. Phys.: Condens. Matter 16 (2004), pp. S2029–S2036.
- [286] A. Härtel and H. Löwen, *Fundamental measure density functional theory for hard spherocylinders in static and time-dependent aligning fields*, J. Phys.: Condens. Matter 22 (2010), p. 104112.
- [287] R. Wittkowski, H. Löwen, and H.R. Brand, *Microscopic and macroscopic theories for the dynamics of polar liquid crystals*, Phys. Rev. E 84 (2011), p. 041708.
- [288] C.G. Gray and K.E. Gubbins *Theory of molecular fluids: fundamentals*, 1st ed., Oxford University Press, Oxford, 1984.

### List of abbreviations

2D	two spatial dimensions
3D	three spatial dimensions
1M-PFC model	single-mode PFC model
2M-PFC model	two-mode PFC model
APFC model	anisotropic PFC model
ATG instability	Asaro-Tiller-Grinfeld instability
bcc crystal structure	body-centred cubic crystal structure
bct crystal structure	body-centred tetragonal crystal structure
BVP	boundary value problem
CH equation	Cahn-Hilliard equation
CMA	constant-mobility approximation
DDFT	dynamical DFT
DEP method	dynamic external potential method
DFT	density functional theory
DLVO potential	Derjaguin-Landau-Verwey-Overbeek potential
DMD simulation	diffusive MD simulation
DSCF theory	dynamic SCF theory
EAP-MD simulation	embedded-atom-potential MD simulation
ELE	Euler-Lagrange equation
EOF-PFC model	eighth-order fitting PFC model
EOM	equation of motion
fcc crystal structure	face-centred cubic crystal structure
FD scheme	finite-difference scheme
FMT	fundamental-measure theory
GRP-PFC model	Greenwood-Rottler-Provatas PFC model
hcp crystal structure	hexagonal close packed crystal structure
HS potential	hard-sphere potential
LJ potential	Lennard-Jones potential
LOK theory	Leibler-Ohta-Kawasaki theory
MC simulation	Monte-Carlo simulation
MCT	mode-coupling theory
MD simulation	molecular-dynamics simulation
Model A	relaxational dynamical equation for a non-conserved order parameter
Model B	relaxational dynamical equation for a conserved order parameter

Model C	coupled relaxational dynamical equations for a non-conserved and a conserved order parameter
Model H	dynamical equation for a conserved order parameter coupled to flow
MPFC model	modified PFC model
NS equation	Navier-Stokes equation
Oldroyd-B model	constitutive model for the flow of viscoelastic fluids
PFC model	phase-field-crystal model
PFC1 model	dynamical equation for the original PFC model without CMA
PFC2 model	dynamical equation for the original PFC model with CMA
PF model	phase-field model
RLV	reciprocal lattice vector
RPA	random-phase approximation
sc crystal structure	simple cubic crystal structure
SCF theory	self-consistent field theory
SH model	Swift-Hohenberg model
VPFC model	vacancy PFC model